The Interaction of Formates with Water Cluster Ions

Malick Diedhiou

Thesis submitted in partial fulfillment of the requirements for the

Doctorate in Philosophy degree in Chemistry

Department of Chemistry and Biomolecular Sciences

Faculty of Science

University of Ottawa,

"Completing my PhD in chemistry marks the culmination of years of dedication, discovery, and determination. Through countless experiments and analyses, I've delved deep into the mysteries of molecules, uncovering insights that contribute to our understanding of the natural world. As I step forward with this achievement, I carry with me the excitement of new possibilities and the satisfaction of overcoming challenges. While this milestone represents the end of one chapter, it also signifies the beginning of countless opportunities to apply my expertise, push the boundaries of scientific knowledge, and make meaningful contributions to the field of chemistry. With gratitude for the support of mentor (Dr. Paul Mayer), colleagues, and loved ones, I look ahead to the next phase of my journey with optimism and enthusiasm."

ABSTRACT

Over the past several decades, the study of gas-phase chemistry has emerged as a prominent area of research, particularly focusing on understanding the behavior of various molecules in the atmosphere. This research explores the gas-phase interaction of formates with water cluster ions and the resulting unimolecular dissociation of protonated and hydrated formates and chloroformates.

Chapter 3 of this thesis investigates the ion-molecule reactions involving neutral methyl formate (MF) and proton-bound solvent clusters W_2H^+, W_3H^+, M_2H^+, E_2H^+, and E_3H^+. Through experimental investigation, it was found that the primary reaction pathway involves the loss of solvent molecules from the initial encounter complex, leading to the formation of protonated methyl formate (MFH^+). Detailed collision-induced dissociation breakdown curves were obtained for the initial solvent-MF proton-bound pairs and trimers, revealing relative activation energies for the observed channels. Density functional theory calculations (B3LYP/6-311+G(d,p)) supported barrierless reactions for solvent loss in each case. Additionally, for $MF(M)H^+$ ions, the loss of CH_4 at higher collision energies was observed. The mechanism of this reaction involves the migration of the MF methyl group to form a loosely bound complex between neutral CH_4 and an ion comprised of $(CH_3OH)(CO_2)H^+$. Overall, these findings demonstrate the formation of stable encounter complexes between methyl formate and atmospheric water, which subsequently dissociate to produce protonated methyl formate.

In chapter 4, the focus is on ion-molecule reactions involving neutral ethyl (EF), isopropyl (IF), t-butyl (TF), and phenyl formate (PF) interacting with proton-bound water clusters W_2H^+ and W_3H^+ (where $W=H_2O$). It was observed that the primary reaction product entails the loss of water from the initial encounter complex, subsequently leading to the formation of protonated formate. Utilizing collision-induced dissociation, breakdown curves of the formate-water complexes were generated, allowing for the extraction of relative activation energies for the identified channels. Density functional theory calculations, employing the B3LYP/6-311+G(d,p) method, further supported these findings by revealing that the water loss reactions exhibit no reverse energy barrier in each instance. Overall, the outcomes suggest that the interaction between formates and atmospheric water can yield stable encounter complexes that eventually dissociate, resulting in the formation of protonated formates.

Chapter 5 further expands on the atmospheric fate of formate-derived esters through the exploration of their dissociation pathways upon protonation. Tandem mass spectrometry serves as the primary tool for studying the unimolecular dissociation of protonated methyl-, ethyl-, isopropyl-, tert-butyl-, and phenyl formate. Key findings reveal distinct fragmentation patterns: methyl- and ethyl formate ions lose CO to form protonated alcohols, with ethyl formate additionally yielding neutral ethanol. Isopropyl- and tert-butyl formate ions readily shed stable radicals and neutral alkenes, alongside methanol loss. Phenyl formate exhibits a unique behavior, involving phenyl radical loss akin to isopropyl- and tert-butyl formate, alongside CO loss similar to methyl- and ethyl formate. The investigation leverages density functional theory to elucidate minimum energy reaction pathways for each ion, with CBS-QB3 single-point energy calculations providing reliable energetics. These insights deepen our understanding of the atmospheric

chemistry of formate-derived esters, contributing to the broader understanding of atmospheric processes.

Chapter 6 explores the gas-phase dissociation of protonated chloroformates, prevalent in the atmosphere due to their utilization as fuel additives and industrial solvents. Tandem mass spectrometry was employed to scrutinize the unimolecular dissociation of protonated methyl (1), ethyl (2), neopentyl (3), and phenyl chloroformate (4). Notably, 1 and 4 exhibited common HCl loss, yielding CH_3OCO^+ and $C_6H_5OCO^+$, respectively, with 1 additionally generating neutral methanol and $ClCO^+$. 4 additionally loses CO and CO_2. In contrast, 2 and 3 each only exhibit a single fragmentation channel, with 2 losing C_2H_4 to generate protonated chloroformic acid and 3 generating protonated 2-methylbutene by losing neutral chloroformic acid. Density functional theory at the B3LYP/6-311+G(d,p) level of theory was employed to explore minimum energy reaction pathways for each ion, and CBS-QB3 single-point energy calculations were used to provide reliable energetics. RRKM (Rice-Ramsperger-Kassel-Marcus) calculations of the rate constants for selected competing processes were carried out to link theory and experiment. One common process observed was the 1,3-H shift of the proton from the carbonyl oxygen to the ester oxygen before dissociation.

ACKNOWLEDGMENTS

I would like to express my deepest gratitude to my parents and wife (Mariama), for their unwavering love, support, and sacrifices throughout my academic journey. Their encouragement, guidance, and belief in my abilities have been the cornerstone of my success, and I am profoundly grateful for their endless encouragement. I am also immensely thankful to God, whose grace and blessings have been ever-present in my life, guiding me through both challenges and triumphs. My faith has been a source of strength, hope, and inspiration, allowing me to persevere in the face of adversity.

Furthermore, I am indebted to the inspiring great people with whom I have had the privilege to collaborate. Dr. Sharon Barden, Dr. Sander Mommers, Dr. Wendy Pell, Dr. Brandi West, and Mr. Sean Overton have broadened my perspective and enriched my academic journey, for which I am truly thankful. I am also thankful for the opportunity to work alongside the outstanding students of the Mayer research group. Each of you has contributed to my growth and learning in unique ways. Special thanks to Dr Bethany Chukwu, Nick, Sandesh, Edgar, Reshmi, and Peace for being so helpful.

At the core of my academic journey stands Pr. Paul Mayer, my supervisor, mentor, and source of inspiration. Professor Mayer's unwavering dedication to scientific inquiry and his contagious passion for research have been transformative. His guidance, patience, encouragement, and belief in my potential have been pivotal in shaping my academic trajectory. I am profoundly grateful for the opportunity to undertake my graduate studies under his supervision.

In conclusion, I express my deepest gratitude to all those who have supported and believed in me throughout this journey. Your contributions, whether big or small, have been integral to the realization of this milestone.

TABLE OF CONTENT

ABSTRACT iii
ACKNOWLEDGMENTS vi
TABLE OF CONTENT viii
LIST OF FIGURES xi
LIST OF TABLES xv
LIST OF ABBREVIATIONS xvi
Chapter 1. FORMATES IN THE ATMOSPHERE 1
1.1. Background 1
1.2. Atmospheric Water Clusters 2
1.3. Reactive Organic Carbon in the Atmosphere 4
1.4. Interactions Between Atmospheric Water Clusters and Reactive Organic Carbon 5
1.5. Atmospheric Chemistry of the Formates 11
1.6. Goals 14
CHAPTER 2. METHODS OF STUDY 16
2.1. Introduction 16
2.2. Triple Quadrupole Mass Spectrometry 17
2.2.1. Electrospray Ionization (ESI) 17
2.2.2. Quadrupole Mass Analyzer 18
2.2.3. Ion Molecule Reactions 19
2.2.4. Collision-Induced Dissociation (CID) 21
2.3. Magnetic Sector Mass Spectrometry 22
2.3.1. Electron ionization 22
2.3.2. Double Focusing Magnetic Sector Mass Spectrometer and the MIKES Experiment 24
2.4. Computational Methods 29
2.4.1. Density Functional Theory (DFT) Calculations 29
2.4.2. Rice–Ramsperger–Kassel–Marcus (RRKM) theory 31

CHAPTER 3. THE INTERACTION OF METHYL FORMATE WITH PROTON-BOUND SOLVENT CLUSTERS IN THE GAS PHASE AND THE UNIMOLECULAR CHEMISTRY OF THE REACTION PRODUCTS 35
3.1. Introduction 35
3.2. Materials and Methods 36
3.2.1. Tandem Mass Spectrometry 36
3.2.2. Computational Methods 37
3.3. Results 38
3.3.1. Solvent Cluster Ion / Methyl Formate Reactions 38
3.3.2. Unimolecular Reactions of Proton-Bound Solvent-MF clusters 42
3.4. Conclusions 48
3.5. Appendix 49
CHAPTER 4. ON THE GAS-PHASE INTERACTIONS OF ALKYL AND PHENYL FORMATES WITH WATER: ION-MOLECULE REACTIONS WITH PROTON-BOUND WATER CLUSTERS 53
4.1. Introduction 53
4.2. Experimental Procedures 55
4.2.1. Chemicals 55
4.2.2. Tandem Mass Spectrometry 55
4.2.3. Computational Methods 56
4.3. Results and Discussion 58
4.3.1. Water Cluster Ion / Formate Reactions 58
4.3.2. Unimolecular Reactions of Proton-Bound Water-Formate Clusters 62
4.4. Conclusions 66
4.5. Appendix 67
CHAPTER 5. THE FATE OF PROTONATED FORMATES IN THE GAS PHASE 70
5.1. Introduction 70
5.2. Experimental Procedures 71
5.2.1. Tandem Mass Spectrometry 72
5.2.2. Computational Methods 72
5.3. Results and Discussion 73
5.3.1. Tandem Mass Spectrometry 73

5.3.2. Calculated Reaction Mechanisms 77
5.4. Conclusions 82
CHAPTER 6. ON THE FATE OF PROTONATED CHLOROFORMATES IN THE GAS PHASE: A COMPETITION BETWEEN FORMING HCl AND CHLOROFORMIC ACID 83
6.1. Introduction 83
6.2. Experimental Procedures 85
6.2.1. Tandem Mass Spectrometry 85
6.2.2. Computational Methods 86
6.3. Results and Discussion 87
6.4. Calculated Reaction Mechanisms 88
6.5. Conclusions 92
6.6. Appendix 94
CHAPTER 7. CONCLUSIONS 95
Future Outlook 96
References 97

LIST OF FIGURES

Figure 1.1: Temperature trends and chemical composition of Earth's atmospheric layers with increasing altitude. 2
Figure 1.2: Geometry-optimized, energetically-stable structures of water clusters, $(H_2O)_n$, $1 \leq n \leq 4$. 3
Figure 1.3: Sources, interactions, and downstream effects of reactive organic carbon, water clusters, and inorganic gases/acids in the troposphere. 8
Figure 1.4: Experimental setup of the Ion Flow Tube. 10
Figure 1.5: Sectional view of the PTR3 tripole. The electric field vector accelerating the ions rotates in the radial direction. 11
Figure 2.1: Experimental setup of the triple quadrupole mass spectrometer. 17
Figure 2.2: Experimental setup of Electrospray Ionization (ESI) experiment. 18
Figure 2.3: Schematic diagram of the Ion Molecule Reaction (IMR) set up, using the protonated water dimer ion and neutral methyl formate as examples. 21
Figure 2.4: Schematic diagram of Collision Induced Dissociation (CID) using the proton-bound methyl formate/water complex (m/z 79) as an example. 22
Figure 2.5: Schematic representation of electron ionization. 23
Figure 2.6: Schematic representation of modified VG-ZAB instrument. 24
Figure 2.7: Diagram illustrating the magnetic sector and its functionality in the context of mass selection. 26
Figure 2.8: Diagram illustrating the electrostatic analyzer and its functionality. 27
Figure 2.9: Diagram of a Photomultiplier Detector. 28
Figure 3.1: Representative mass spectra of neutral methyl formate reacting with a) water dimer ion (m/z 37, **R1**), b) water trimer ion (m/z 55, **R2**), c) methanol dimer ion (m/z 65, **R3**), d) ethanol dimer ion (m/z 93, **R4**), and e) ethanol trimer ion (m/z 139, **R5**). 39
Figure 3.2: Relative energy (B3LYP/6-311+G(d,p)) of the major product ions resulting from the reaction between neutral methyl formate with a) the water cluster dimer and b) the water cluster trimer, c) the methanol dimer, d) the ethanol dimer and e) the ethanol trimer. 41

Figure 3.3: CID breakdown curves of a) $P^+ = MF(W)H^+$, b) $P^+ = MF(M)H^+$, and c) $P^+ = MF(E)H^+$. 43
Figure 3.4: CID breakdown curves of a) $P^+ = MF(M)_2H^+$, b) $P^+ = MF(E)_2H^+$ and c) $P^+ = MF(E)_3H^+$. 44
Figure 3.5: relaxed potential energy scan of the dissociation of $MFWH^+$ and $MF(E)_3H^+$ at the B3LYP/6-311+G(d,p) level of theory. 45
Figure 3.6: B3LYP/6-311+G(d,p) minimum energy reaction pathways surface for the dissociation of $MF(M)H^+$ (m/z 93). 46
Figure S3.1: RRKM k(E) vs E curves for the dissociation of the ion-molecule encounter complexes. 49
Figure S3.2: Vibrational internal energy distributions at 300 K for the encounter complexes in **R1**-**R5**. 50
Figure S3.3: RRKM modeled breakdown curves for reactions in Figures 3.3 and 3.4. To accommodate the model, sequential reactions (such as loss of H_2O from m/z 33 in Figure 3.3a) were summed into the primary product ion abundance. 52
Figure 4.1: Representative mass spectra of water dimer ion (m/z 37, highlighted with the *) reacting with neutral a) EF (74 Da, **R1**), b) IF (88 Da, **R2**), c) TF (102 Da, **R3**), d) and PF (122 Da, **R4**). 58
Figure 4.2: Representative mass spectra of water trimer ion (m/z 55, highlighted with the *) reacting with neutral a) EF (74 Da, **R5**), b) IF (88 Da, **R6**), c) TF (102 Da, **R7**), and d) PF (122 Da, **R8**). 59
Figure 4.3: Relative energy (B3LYP/6-311+G(d,p)) of the main product ions from the interaction of the water dimer ion (m/z 37) with neutral a) EF (**R1**), b) IF (**R2**), c) TF (**R3**), d) and PF (**R4**). 60
Figure 4.4: Vibrational internal energy distributions at 300 K for the encounter complexes in a) **R1** and c) **R8** and the RRKM k(E) vs E curves for the dissociation of the corresponding ion-molecule encounter complexes (b, d). 61
Figure 4.5: Relative energy (B3LYP/6-311+G(d,p)) of the main product ions from the interaction of water trimer ion (m/z 55) with neutral a) EF (**R5**), b) IF (**R6**), c) TF (**R7**), and d) PF (**R8**). .. 62
Figure 4.6: CID breakdown curves of a) $P_1^+ = EF(W)H^+$, b) $P_2^+ = IF(W)H^+$, c) $P_3^+ = TF(W)H^+$ and c) $P_4^+ = PF(W)H^+$. 63

Figure 4.7: Relaxed potential energy scan of the dissociation of $TF(W)H^+$, $IF(W)_2H^+$ and $PF(W)_3H^+$ at the B3LYP/6-311+G(d,p) level of theory. 65
Figure 4.8: RRKM modeled breakdown curves for $EF(W)_2H^+$ $IF(W)_2H^+$, $TF(W)_2H^+$ or $PF(W)_2H^+$ complexes. Sequential fragmentation channels were summed into the primary channel to aid the modeling of those primary pathways. The solid line represents the RRKM fit. 66
Figure S4.1: Calculated minimum energy structures for (W)2H+ and (W)3H+ at the B3LYP/6-311+G(d,p) level of theory. 67
Figure S4.2: Vibrational internal energy distributions at 300 K for the encounter complexes. .. 67
Figure S4.3: RRKM k(E) vs E curves for the dissociation of the ion-molecule encounter complexes. 68
Figure 5.1: Global minimum calculated protonated formates at the B3LYP/6-311+G(d,p) level of theory. 73
Figure 5.2: Representative CID mass spectra (each at the given E_{LAB}) of protonated **a)** methyl formate (**1**, m/z 61, 25 eV), **b)** ethyl formate (**2,** m/z 75, 10 eV), **c)** isopropyl formate (**3**, m/z 88, 13 eV), **d)** t-butyl formate (**4**, m/z 103, 10 eV) and **e)** phenyl formate (**5**, m/z 123, 10 eV). 74
Figure 5.3: CID breakdown curves of protonated **a)** methyl formate (**1**), **b)** ethyl formate (**2**), **c)** isopropyl formate (**3**), **d)** tert-butyl formate (**4**), and **e)** phenyl formate (**5**). 75
Figure 5.4: CBS-QB3//B3LYP/6-311+G(d,p) minimum energy reaction pathways for CO loss (—) and CO,H_2O loss (····) and from **1**. 78
Figure 5.5: CBS-QB3//B3LYP/6-311+G(d,p) minimum energy reaction pathway for C_2H_5OH loss (---) and CO loss (—) from **2**. 79
Figure 5.6: CBS-QB3//B3LYP/6-311+G(d,p) minimum energy reaction pathways for H_2CO_2 loss (- · -), C_3H_6 loss (---) and CH_3OH loss (—) from **3**. 80
Figure 5.7: CBS-QB3//B3LYP/6-311+G(d,p) minimum energy reaction pathways for H_2CO_2 loss (- · -) and CH_3OH loss (---) from **4**. 81
Figure 5.8: CBS-QB3//B3LYP/6-311+G(d,p) minimum energy reaction pathways for H_2CO_2 loss (- · -), and two possible paths to CO loss (— · · —) and (—) from **5**. 82
Figure 6.1: Global minimum structure for all calculated protonated chloroformates at the B3LYP/6-311+G(d,p) level of theory. 86
Figure 6.2: MIKE mass spectra of the ^{35}Cl isotope of protonated a) methyl chloroformate (**1**, m/z 95), b) ethyl chloroformate (**2**, m/z 109), c) neopentyl chloroformate (**3**, m/z 151), and d) phenyl

chloroformate (**4**, m/z 157). In each case the selected precursor ion (at 8000 eV) is several orders of magnitude greater in abundance than the displayed fragment ions and is omitted for clarity. 87

Figure 6.3: CBS-QB3(sp)//B3LYP/6-311+G(d,p) minimum energy reaction pathways for the unimolecular decomposition of **1**..... 89

Figure 6.4: CBS-QB3(sp)//B3LYP/6-311+G(d,p) minimum energy reaction pathway for C_2H_4 loss **2**. 90

Figure 6.5: CBS-QB3(sp)//B3LYP/6-311+G(d,p) minimum energy reaction pathways for $ClCO_2H$ loss from **3**. 91

Figure 6.6: CBS-QB3(sp)//B3LYP/6-311+G(d,p) minimum energy reaction pathways for CO_2 loss (—), CO loss (---) and HCl loss (—) from **4**. 92

Figure S6.1: RRKM k(E) vs E curves for the dissociation of protonated methyl chloroformate. The region responsible for observations in the MIKE experiment is shown in the box..... 94

LIST OF TABLES

Table 3.1: Comparison of the RRKM estimated reaction energies[1] (*Figure S3.3*) with those calculated values shown in *Figure 3.2*..... 47
Table S3.1: Additional reactions observed in the ion-molecule reactions explored in this study. Energies calculated at the B3LYP/6-311+G(d,p) level of theory..... 49
Table 4.1: Theoretical Energies calculated from *Figure 4.3*. 69

LIST OF ABBREVIATIONS

VOC	Volatile Organic Compounds
SOA	Secondary Organic Aerosols
ΔS‡	Activation Entropy
ZPE	Zero-Point Energy
BD	Breakdown Diagrams
TST	Canonical Transition State Theory
CVTST	Canonical Variational Transition State Theory
DFT	Density Functional Theory
CBS	Complete Basis Set
ESA	Electrostatic Analyser
ROC	Reactive Organic Carbon
ESI	Electrospray Ionization
TPES	Threshold Photoelectron Spectra
FFR	Field-Free Region
IRC	Intrinsic Reaction Coordinate
RRKM	Rice-Ramsperger-Kassel-Marcus
IE	Ionisation Energy
MF	Methyl Formate
EF	Ethyl Formate
IF	Isopropyl Formate
TF	T-butyl Formate
PF	Phenyl Formate
MCF	Methyl Chloroformate
ECF	Ethyl Chloroformate
NCF	Neopentyl Chloroformate
PCF	Phenyl Chloroformate
W	Water
M	Methanol
E	Ethanol
IMR	Ion Molecule Reaction
MS	Mass Spectrometry
CID	Collision-Induced Dissociation
GC/FID	Gas chromatography Flame Ionization Detector
GC/MS	Gas chromatography Mass Sprctromety
MIKES	Mass-Analysed Ion Kinetic Energy Spectrometry

Chapter 1. FORMATES IN THE ATMOSPHERE

1.1. Background

Earth's atmosphere has been studied for decades, and measurements of temperature and pressure have led to the identification of 5 main atmospheric layers. These layers are the troposphere, stratosphere, mesosphere, thermosphere, and exosphere. The temperature trends with altitude, relative gas compositions, and sizes of each layer are shown in *Figure 1.1*. The layer lying closest to the Earth's surface, the troposphere, is the main region of interest when studying atmospheric chemistry [1]. This is due to the fact that the troposphere is responsible for the weather events observed by humans, and it contains around 80% of the atmosphere's total mass. The composition of gases in the troposphere remains relatively constant, with its main components being nitrogen (78%) and oxygen (21%). The remainder of the air content is composed of trace gases such as argon, but also varying amounts of water vapor. Latitude, altitude, temperature, season, and human activities are all factors that affect the amount of water vapor in the atmosphere [2].

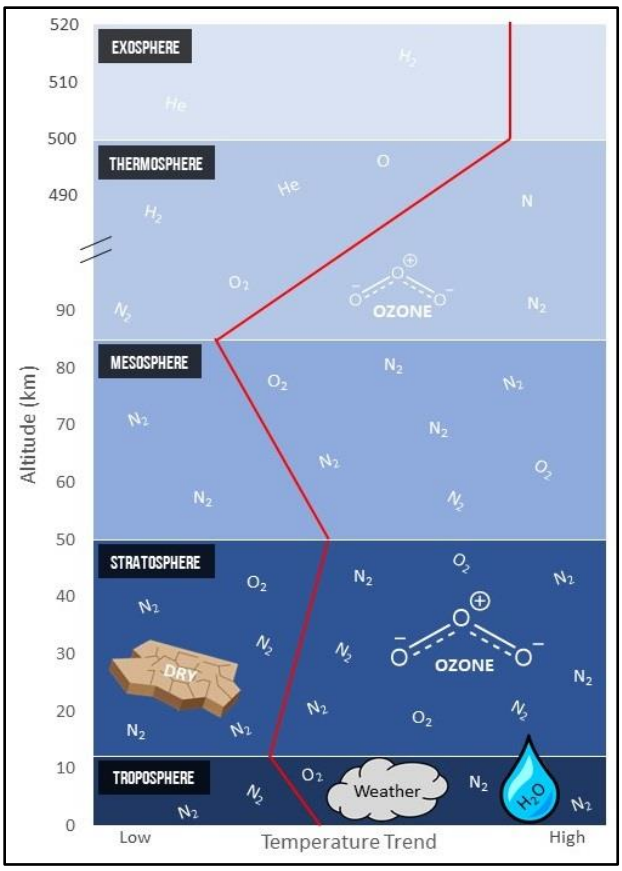

Figure 1.1: Temperature trends and chemical composition of Earth's atmospheric layers with increasing altitude.

1.2. Atmospheric Water Clusters

Water vapor is known to be important in atmospheric chemistry, and its involvement in reactions can influence weather, pollution, acid rain, and climate change. More specifically, the ability of small clusters of water molecules in the atmosphere to catalyze reactions, enhance photochemical degradation, and contribute to organic aerosol formation has become a rapidly growing area of research to better understand atmospheric processes [3-5].

The predicted stability and abundances of different sizes of water clusters in the atmosphere have been addressed in recent studies through computational methods. Most of the findings suggest that there are highly stable structures for small water clusters of 1 to 4 molecules. Those with 3-4 molecules will form stable hydrogen bonding networks in a cyclic fashion and are predicted to be present in the atmosphere and to contribute greatly to chemical reactions. A few of these structures are shown in *Figure 1.2* [3,6]. Water clusters ranging from 1 to 30 molecules have also been detected experimentally. The "magic cluster" with 21 water molecules tends to be the most abundant in all recorded results [7].

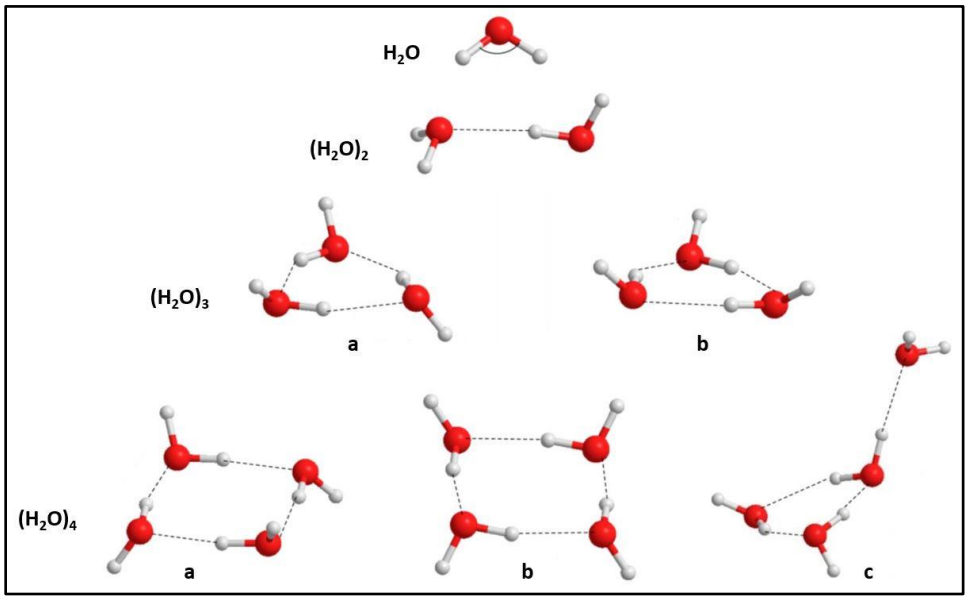

Figure 1.2: Geometry-optimized, energetically-stable structures of water clusters, $(H_2O)_n$, $1 \leq n \leq 4$.

Water clusters can interact with inorganic atmospheric gases, enhancing the rates of sunlight-driven reactions. Some examples of this include van der Waals interactions with ozone and acetone in the troposphere, enhancing photolysis and the production of hydroxyl radicals. These radicals are known to be important oxidizing agents in the atmosphere [6,8].

The ability of water clusters to contribute hydrogen bonds allows them to catalyze a plethora of reactions. Several inorganic gaseous and acidic atmospheric reactions catalyzed by water clusters have been studied by computational modelling of reaction pathways. The findings suggest that small water clusters (1-4 molecules) can effectively catalyze the HO_2 self-reaction, HO_2 reaction with HS, and NO_2 hydrolysis. The products of these reactions are oxidants and inorganic acids which contribute to acid rain production [5,9,10].

1.3. Reactive Organic Carbon in the Atmosphere

Another category of molecules which is important in the troposphere is reactive organic carbon (ROC). Any atmospheric organic molecule containing carbon (excluding methane) is considered to be ROC. The class of molecules contains thousands of species, including sub-classes such as volatile organic carbon (VOC). ROCs can undergo oxidation by hydroxyl radicals followed by subsequent cascades of reactions leading to CO_2 production, tropospheric ozone pollution, ground-level smog, and organic aerosol/particulate matter formation [11].

The sources contributing to ROC emissions have been heavily studied as environmental concerns continue to rise. A study on VOCs in British Columbia used factor analysis to identify 9 main sources of ROC emissions, including industrial solvents, natural gas combustion, and biogenic sources [12]. Air and water samples from clouds show that ROC levels in the atmosphere are heavily impacted by solar UV radiation intensity as well microbial metabolic activity [9]. Biogenic emissions have recently been identified as one of the major contributors to VOC levels in the

atmosphere. Studies on the Norway spruce concluded that CO_2 availability, sunlight intensity, and temperature all affect how much VOCs plants emit [13].

The incorporation of ROCs into organic aerosols can cause adverse health effects for humans. The oxidation of ROCs in organic aerosols by hydroxyl radicals leads to "aging", gradually increasing the oxidation state of all carbon in the atmosphere. This trend leads ROCs towards the production of CO_2 [14].

Heald & Kroll's review paper suggests that a more holistic approach to studying atmospheric chemistry is necessary. Most recent works studying ROCs in the atmosphere focus on examining individual species reacting in isolation. However, this piecewise approach is not thought to be sufficient, since the atmosphere involves thousands of different molecules which can undergo thousands of different reactions, all of which can interact and are interwoven as a system. Focusing on the interactions between atmospheric species is the first step towards better understanding the processes that govern weather, pollution, and climate change [11].

1.4. Interactions Between Atmospheric Water Clusters and Reactive Organic Carbon

Following the movement towards studying how different species interact in the troposphere, a natural progression is to look at the reactions between reactive organic carbon and water clusters. The ozonolysis of alkenes in the atmosphere leads to production of the Criegee intermediate (RR'COO), which can decompose into hydroxymethyl hydroperoxide and eventually hydroxyl radicals. Small water clusters are known to catalyze this decomposition. Computational analysis

of clusters of size 1-4 molecules has shown that although larger clusters reduce activation energies the most, the water dimer dominates the process due to its balanced complex stabilization and abundance, contributing to the greatest rate enhancement [15]. Formic acid decomposition is also catalyzed by water clusters. Decarboxylation results in the production of CO_2 and H_2 gases from cis-formic acid, while trans-formic acid leads to dehydration to create H_2O and CO gas. The presence of water clusters allows stabilizing hydrogen bonds to form with the formic acid molecules. As clusters increase in size, a cooperativity effect dominates in which the intermolecular hydrogen bonds strengthen, while the formic acid's intramolecular bonds are weakened. Computations determined that the highest rates and lowest activation energies were achieved with water clusters of 2-3 molecules interacting with cis-formic acid, catalyzing decomposition by decarboxylation [16]. These findings make it clear that water clusters have a critical influence on the rates of atmospheric reactions and thus the downstream effects caused by their products.

Furthermore, water clusters and ROC interactions are known to be involved in organic aerosol and cloud condensation nuclei formation and growth. Aerosols, as discussed previously, are significant tropospheric pollutants having health concerns, while cloud formation patterns greatly impact weather. Proton transfer from the biogenic ROC, pinene, to water clusters larger than 7 molecules has been shown to be a highly effective method of charge transfer to initiate cloud formation [17]. The incorporation of methanol, formic acid, amines, and sulfuric acid into water clusters has been extensively modelled computationally and experimentally, and the results generally show favorable intermolecular interactions (hydrogen bonds and proton transfers) which are believed to enhance the formation of aerosols & cloud nuclei [7,18,19]. Large biogenic ROCs such as isoprene

and monoterpenes, on the other hand, have not been shown to contribute significantly to organic aerosol production. Their interactions with water clusters are weak, which is due to their inability to contribute enough hydrogen bonds to make up for their largely hydrophobic natures [4].

A broad summary and general overview of the sources of water clusters, factors affecting ROC levels, interactions between the classes of species, and the downstream atmospheric effects of these interactions is shown in *Figure 1.3*.

In the past, many research papers have focused on studying the significance of water clusters and reactive organic carbon reactions and interactions in atmospheric chemistry. Many recent studies mentioned previously did so primarily through computational modelling [3,5,6,8-10], however others opted to use experimental methods to analyze these relationships [7,12-14,16,18,20].
These studies shed light on the intricate interactions between water clusters and reactive organic carbon (ROC) in atmospheric chemistry. Investigations into the structural dynamics of small water clusters revealed insights from low temperatures to vaporization, while studies on radical-radical reactions highlighted the catalytic efficiency of water monomers. Examination of ozone-water complexes unveiled their stability and predicted concentrations in the Earth's atmosphere. Furthermore, investigations into formic acid-water interactions indicated potential disruptions in cluster structures, impacting processes like nucleation and particle growth. The studies concluded that interactions between water clusters and reactive organic carbon (ROC) play a crucial role in atmospheric chemistry, affecting processes such as nucleation, particle growth, and radical-radical reactions.

The interactions between pinene and water clusters were measured in a 2019 study using TOF-MS devices. Two ion sources, electron ionization (EI) and photoionization after sodium doping (NaPI) were incorporated and compared. Spectra produced from the EI samples favored pinene clusters, while those from NaPI were highly selective towards pure water clusters. EI caused excessive fragmentation and loss of the pseudomolecular and molecular ions [16].

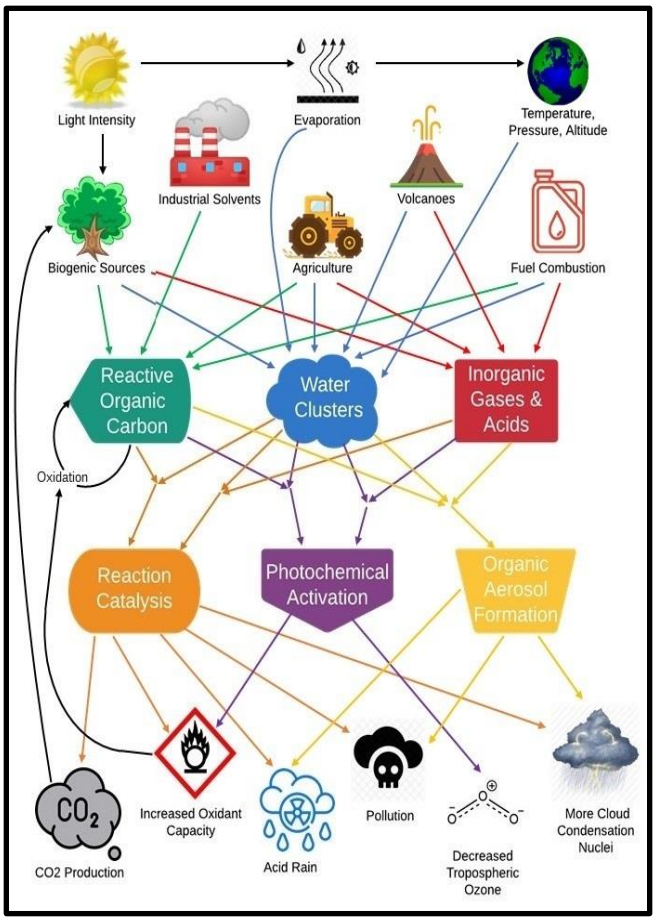

Figure 1.3: Sources, interactions, and downstream effects of reactive organic carbon, water clusters, and inorganic gases/acids in the troposphere. Combined arrows shows molecules interacting each other.

An older study, from 1989, aimed to analyze the fragmentation of mixed methanol-water clusters using tandem mass spectrometry (MS/MS). Clusters of the desired size were selected using the

first MS based on m/z ratio, and then redirected into a CID experiment with He gas. The specific MS instruments used involved reversed geometry double focusing techniques which created high-energy ions (keV range) to allow for a large amount of fragmentation to be observed. Kinetic energies were measured through mass-analysed ion kinetic energy spectroscopy (MIKES) [18]. Data collected from these two analytical methods showed that as ion cluster sizes increased, the kinetic energy released by their interactions increased as well. This should not be surprising, since the result is in accordance with classical physical predictions and has been previously recorded in various ion cluster studies. In regard to the fragmentation pattern of methanol-water cluster ions after MS/MS-CAD, the major observation from the pattern is that the clusters preferentially lose water molecules over methanol molecules. The findings in this study highlight the ability of different ROC-containing water clusters to contribute to atmospheric chemistry, as well as the importance of understanding the intermolecular interactions which influence their properties.

The interactions of water clusters with formic acid have been studied previously using unique home-made apparatuses. One example of this involves a fast-flow reactor and high-pressure ion source, allowing for the creation of protonated water clusters ranging from 2 to 30 molecules in size (*Figure 1.4*). These are then directed through the flow tube, where reactant gas (He and formic acid mixture) is injected through a reactant gas inlet. The products of the collisions are then pushed through a nose cone, where they are analyzed by a quadrupole MS, and lastly reach the electron multiplier detector. Results showed good resolution in separating the individual cluster sizes, and findings were in accordance with previous studies [7]. The researchers found that the addition of formic acid disrupted the clathrate-like structure of the "magic" 21-molecule water cluster, as evidenced by the absence of a prominent peak in intensity ratio graphs. This disruption was in

contrast to the observed stability of the 21-molecule cluster in the methanol system. Furthermore, they observed an increase in intensity with increased cluster size in the formic acid-water mixed clusters, suggesting that these clusters may serve as prenucleation embryos for the nucleation of water molecules and as a potential pathway for particle growth.

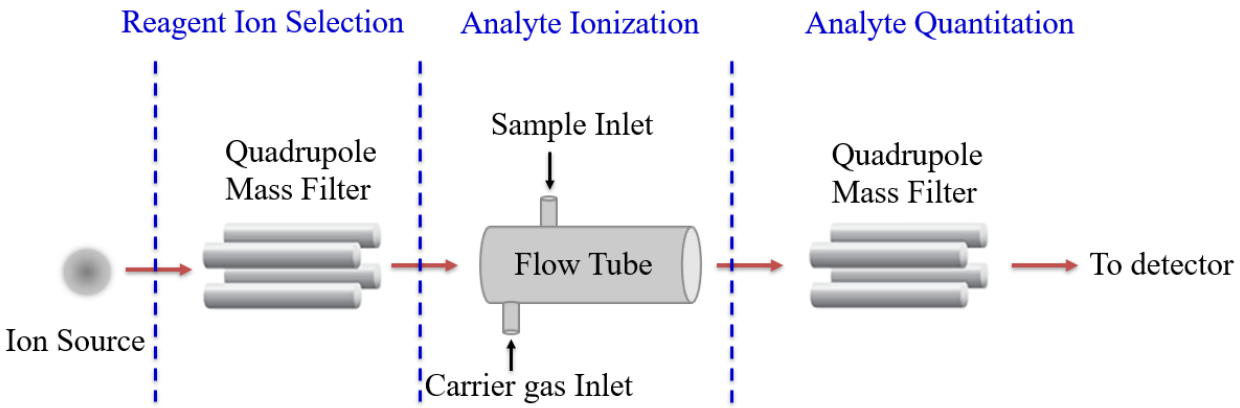

Figure 1.4: Experimental setup of the Ion Flow Tube.

Another unique apparatus which has been developed in recent years to study reactive organic carbon specifically is the Proton Transfer Reaction 3 (PTR3) instrument (*Figure 1.5*). Created by a team from Germany, their goal was to create a device that would perform better than previous models of PTR-TOF-MS, with lower detection limits and higher sensitivities to be able to detect VOC concentrations in the ppqv range (atmospherically relevant concentrations). PTR3 uses proton transfer from hydronium ions to softly ionize VOCs, creating pseudomolecular ions which are unlikely to fragment excessively. The unique feature of this instrument is that instead of using a 2D quadrupole, a 2D tripole reaction chamber was selected. The purpose of this is to decouple the ion velocity from the field direction to produce the optimal field to gas density ratio. Using nitrogen as the carrier gas and keeping the tripole radio frequencies 120 degrees out of phase, it was found that the PTR3 devices were more efficient at transmitting molecular ions with large m/z

(>100) compared to smaller ions. Poor sensitivity and higher detection limits for smallions (low m/z ratio), showing that the PTR3 is only effective at detecting VOCs with large m/z ratios [20].

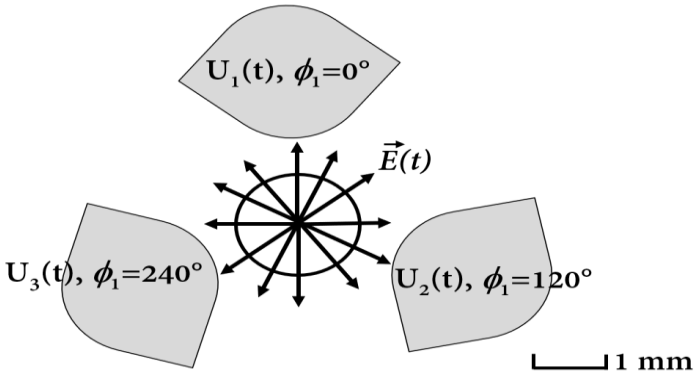

Figure 1.5: Sectional view of the PTR3 tripole. The electric field vector accelerating the ions rotates in the radial direction.

FT-ICR methods with laser vaporization ion sources and helium as the carrier gas have also been used recently to study water cluster interactions with ROC. Anionic water clusters of size 30 to 70 molecules were selected, and reacted with gaseous formic acid introduced through a needle valve [20].

1.5. Atmospheric Chemistry of the Formates

The molecules in one specific class of reactive organic carbon, the formates ROC(O)H (where R=alkyl, phenyl), are of atmospheric significance and a major point of interest in the current work. Formates are derivatives of formic acid, which is known to be the most abundant carboxylic acid in the troposphere [21,22].

Previous work has used analytical techniques to measure formate mixing ratios and concentrations in different atmospheric phases. In the gas phase, formate levels were reported to be around 80 to 300 pptv [22]. Concentrations in organic aerosols and particulate matter were measured as 0.71 to 0.91 μg/m^3 [23], or alternatively, 0.5 to 270 ppt. Formate concentrations of 0.3 to 23.6 μM were observed in rainwater, and the combined effects of formate and acetate are estimated to contribute to around 64% of total rainwater acidity [24]. Other studies found formate levels in non-urban precipitation in the 10 to 30 μM range [25]. Cloud water, fog, and dew also contain formates at concentrations of 3.2 to 627 μM [24]. The effects of formates in rainwater have been observed at the surface, with high concentrations of formates being found in the black crusts of degraded stone and lime mortar monuments (50 to 5000 μg/g of black crust) [26]. The most significant anthropogenic sources of atmospheric formates are vehicular fuel combustion (from incomplete combustion and fuel additives) and biomass burning [22,24,25]. Biogenic and non-biogenic sources include direct emission from vegetation, release from soil, and formicine ants [24]. Secondary atmospheric reactions are also known to affect formate levels, especially photooxidation processes. Some common reactions producing formates include ozone-olefin reactions, peroxyacetyl radical reactions, oxidation of formaldehyde by OH [22], isoprene photooxidation, and aldehyde oxidation by HO_2 [24]. Chemical degradation is a negligible sink for the formate molecule specifically [25], while wet & dry deposition contribute to 95% of formate removal from the troposphere [24].

Although the formate molecule itself is not significantly affected by chemical degradation, formate-derived esters can take part in a vast range of reactions in the troposphere. Some common formate esters which have been previously studied in their roles in atmospheric chemistry include methyl formate, methyl chloroformate, *iso*-propyl formate (IF), and *tert*-butyl formate (TF) [27-

30]. As with the formate molecule itself, the formate-derived esters are emitted by industrial solvents and fuel additives [27-30]. Methyl formate is classified as a VOC, due to its low boiling point of 34°C. As with most VOC species, it can undergo oxidation by OH radicals, but this can occur at two possible sites: the carbonyl side or the methyl side. Proton abstraction tends to occur more at the carbonyl side, with a branching ratio of 0.55 ± 0.07. Once the acyl or alkyl radicals form from methyl formate oxidation, they react with oxygen to form peroxy radicals, followed by alkoxy radical formation, peroxy nitrate radical generation, and lastly decomposition to CO_2 [27]. The thermodynamics and kinetics of methyl formate oxidation have also been extensively studied through computational work. A unique trend of negative temperature dependence of the rate constant below 100K has been found, failing to adhere to Arrhenius models. As for the selectivity of the proton abstraction, the methyl side dominates below 100K, while the carbonyl side is preferred above 300K. In the intermediate temperature range, branching ratios are highly dependent on pressure [28]. Methyl formate can also produce methanol through exothermic hydrogenolysis at atmospheric conditions, with the highest rates occurring at 180°C [29]. Methyl chloroformate, a similar species, can photolyse in the troposphere upon absorption of UV light (193.3nm) to produce the methoxy carbonyl radical. This radical contributes to a further cascade of gas-phase reactions, and eventually decomposes into CO_2 and methyl groups which lead to global warming and pollution [30]. IF & TF, like methyl formate, also undergo oxidation by OH radicals. Pimentel et al. used chlorine atoms to initiate proton abstractions to determine the branching ratios and product distributions of IF & TF oxidation. A branching ratio of 0.30 ± 0.03 was obtained for deprotonation at the formyl hydrogen of IF, while 0.50 ± 0.05 was measured for TF. Branching ratios were consistent across the temperature range studied. The presence of N_2, O_2, NO, and NO_2 led to the production of acyl peroxy nitrate radicals, formaldehyde, acetone,

formic acid, acetic formic acid anhydride, CO, and CO_2. Radicals produced from TF had a higher tendency to decompose, leading to slightly different product distributions. Clearly, an immense range of species can evolve from the oxidation of a few simple formates, proving their significance [27].

At present, only a handful of studies have investigated formate interactions with water clusters in the gas-phase or the atmosphere. To our knowledge, only the formate molecule itself has been investigated in its interactions with water, while formate-derived esters have not been studied at all in this context. One 2006 study uses FT-ICR MS to experimentally determine the outcome of formic acid interactions with hydrated electrons, $(H_2O)_n^-$. It was found that in water clusters of 30-70 molecules, formates form through the exothermic loss of hydrogen gas from formic acid and water, leaving a formate anion as the new centre of the cluster. These clusters are then more likely to undergo further reactions, incorporating more formic acid molecules while releasing more water molecules [31]. Another paper uses Franck-Condon computational simulations of photodetachment spectra to study the behaviour and properties of formate-water cluster anions. Proton transfers from water to formates were determined to be favourable, but only once 0.35 eV of energy is supplied after photodetachment of the anionic cluster into the neutral cluster has been completed [21].

1.6. Goals

In the present thesis, mass spectrometry and computational methods will be used to study the interactions and fate of formates with small water cluster cations (dimer and trimer) in the gas phase. While previous research has extensively investigated the behavior of formic acid and its derivatives in the atmosphere, including their interactions with water clusters, the specific

interactions of formates with small water clusters and the unimolecular of product complexes and cations have not been studied. Understanding these interactions is essential for comprehensively characterizing the complex processes occurring in the atmosphere, including aerosol and cloud formation, as well as the production of pollutants and greenhouse gases.

CHAPTER 2. METHODS OF STUDY

2.1. Introduction

As shown above in the previous studies, water droplets can be generated by using different instruments and methods, and in this project, triple quadrupole mass spectrometry (in which collision-induced dissociation (CID) can be performed) was used with electrospray ionization (ESI) as the ion source. Density Functional Theory (DFT) and Rice–Ramsperger–Kassel–Marcus (RRKM) were also used to get information about energies and properties of the species studied here.

Mass spectrometry (MS) is a versatile analytical technique that allows for the precise measurement of the mass-to-charge ratio (m/z) of ions. It has become an indispensable tool in scientific research and various fields due to its ability to provide detailed information about the composition, structure, and properties of molecules. At its core, mass spectrometry operates based on the principles of ionization, mass analysis, and ion detection. First, sample molecules are ionized by various techniques, such as electron ionization (EI), chemical ionization (CI), or electrospray ionization (ESI). This step creates ions with a specific charge (typically 1+). Second, the ions are then separated based on their mass-to-charge ratio (m/z) within a mass analyzer. Different types of mass analyzers, such as quadrupoles, time-of-flight (TOF), or ion traps, can be used depending on the specific analytical requirements. Finally, the separated ions are detected, and the resulting data is used to create mass spectra. The intensity of ion signals in the mass spectrum provides information about the abundance of different ions. In this work, we have used a) electrospray

ionization with a triple quadrupole mass analyzer and b) electron ionization with a magnetic sector double-focusing mass analyzer.

2.2. Triple Quadrupole Mass Spectrometry

In a triple quadrupole mass spectrometer ions undergo three stages of mass selection, fragmentation and analysis before being detected (*Figure 2.1*).

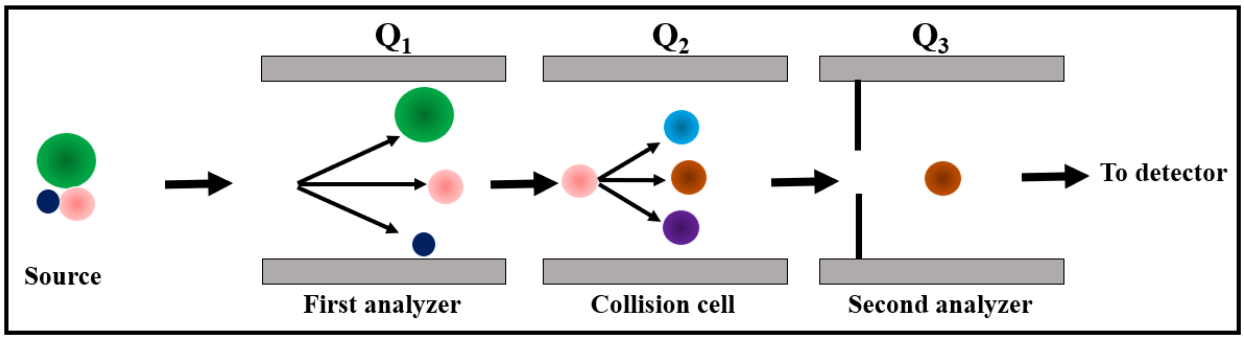

Figure 2.1: Experimental setup of the triple quadrupole mass spectrometer.

2.2.1. Electrospray Ionization (ESI)

Electrospray Ionization (ESI) works by generating ions from a liquid sample, making it particularly useful for analyzing polar and nonvolatile compounds. In the context of studying the fate of formates in the atmosphere, a sample containing formates is typically dissolved in water. This solution is then introduced into an ESI source through a syringe pump at 50 μl/min flow (*Figure 2.2*). The solvent emerges from a fine caplliary which has a high voltage applied to it. This field induces the formation of ions by a process known as the Taylor cone-jet mechanism, nebulizing the solution into tiny charged droplets. As the solvent evaporates excess charge accumulates on the surface of these droplets, creating a high electric field at the droplet's surface

[32]. These ions represent the chemical constituents of the sample, and they can be transferred to the mass spectrometer (first quadrupole) for analysis [33].

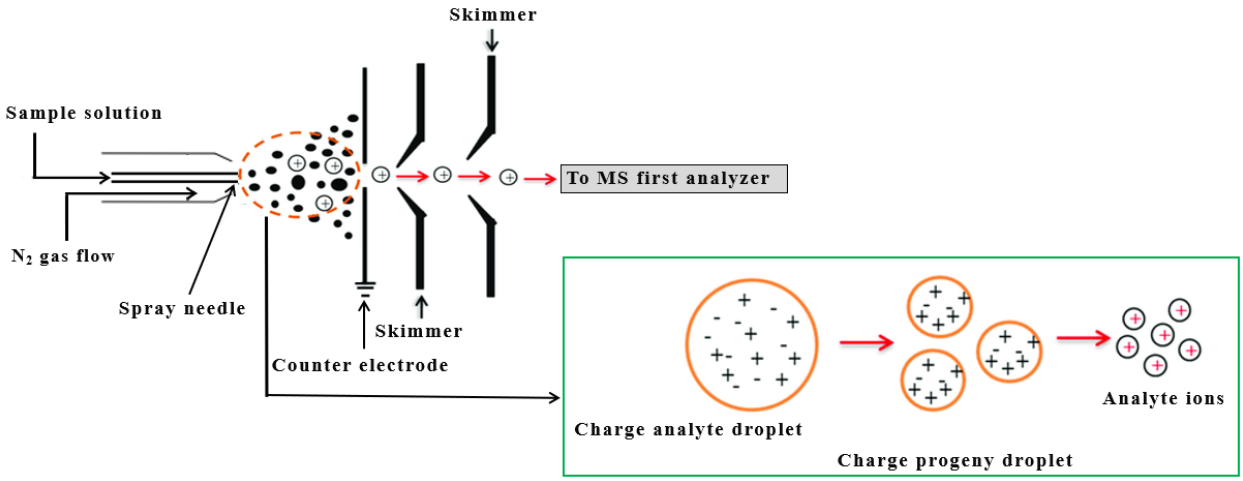

Figure 2.2: Experimental setup of Electrospray Ionization (ESI) experiment.

2.2.2. Quadrupole Mass Analyzer

Historically, triple quadrupole mass spectrometers operate by using three sets of quadrupole mass filters to selectively analyze and quantify specific molecules within a sample. In practice, our instrument uses two quadrupoles and an ion tunnel as the collision cell. The first quadrupole (Q1) selectively filters ions based on their mass-to-charge ratio (m/z), allowing only the target ions to pass through. These ions then enter the collision cell (ion tunnel), where collisions with a neutral gas atom or molecule leads to fragmentation. The resulting fragment ions are then analyzed in the next quadrupole (Q3), which acts as a second mass filter to select the desired product ions. The motions of ions within quadrupole devices significantly differs from the linear paths observed in field-free regions, as well as in magnetic and electrostatic sectors. Described as dynamic instruments, quadrupole mass filters or analyzers exhibit ion trajectories influenced by time-dependent forces. To establish a quadrupole field in these instruments, electrodes with a hyperbolic geometric form are subjected to a potential. Now, the pursuit involves developing a theory of ion

motion that comprehensively explains the dynamics of charged particles in a quadrupole field. Initially, let's examine the forces acting on a single ion within this field [34,35]. Within a quadrupole field, an ion encounters robust focusing, where the restoring force propelling it back to the device center intensifies as the ion deviates from the center. The exploration for a theory of ion motion leads to the Mathieu equation [36], a second-order linear differential equation initially described by Mathieu. Mathieu's mathematical exploration of vibrating stretched skins enabled the definition of solutions in terms of stability and instability regions [37,38].

$$\frac{d^2u}{d\xi^2} + (a_u - 2q_u cos2\xi)u = 0 \qquad (2.1)$$

where u represents the coordinate axes x, y and z, ξ is a dimensionless parameter equal to Ωt/2 such that Ω must be a frequency as t is time; a_u and q_u are additional parameters known as trapping parameters. Applying these solutions and concepts of stability and instability, we can delineate the trajectories of ions confined in quadrupole devices and specify the limits of trajectory stability. To employ Mathieu's solutions, we must confirm that the equation of motion for an ion confined in a quadrupole device aligns with the Mathieu equation. The approach involves obtaining an expression for a force in the Mathieu equation and comparing it with the force acting on an ion in a quadrupole field [39].

2.2.3. Ion-Molecule Reactions

In a triple quadrupole mass spectrometer, the collision cell also serves as a crucial component for performing ion-molecule reactions. When selected ions from the first quadrupole interact with a neutral gas in the collision cell, ion-molecule reactions (IMR) can result. During IMR, the selected

ions are accelerated through the collision cell and as these ions travel, they collide with neutral molecules present in the gas phase. These collisions lead to various ion-molecule reactions.

The specific reactions that occur depend on factors such as the nature of the ions and neutral molecules involved, their respective charges, and their collision energies. Common results of ion-molecule reactions in collision cells include ion-molecule complex formation, proton transfer, charge transfer, and radical reactions. Proton transfer involves the transfer of a proton from one molecule to another, resulting in the formation of new ions with different masses and charges. Charge transfer reactions involve the transfer of an electron from one species to another, leading to changes in charge states. Radical reactions involve the formation or dissociation of radical species through bond cleavage or bond formation processes.

As for this project, neutral formate vapours were introduced into the collision cell of the instrument through a 0.5 mm orifice where they interact with the ionized water/solvent cluster in question (*Figure 2.3*).

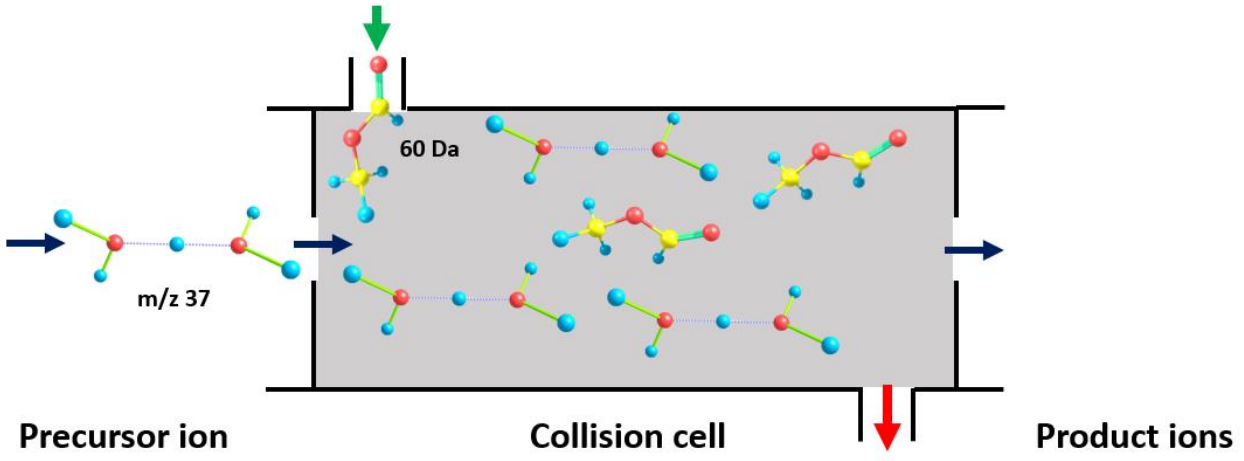

Figure 2.3: Schematic diagram of the Ion Molecule Reaction (IMR) set up, using the protonated water dimer ion and neutral methyl formate as examples.

2.2.4. Collision-Induced Dissociation (CID)

Collision-induced dissociation (CID) is a fundamental technique in mass spectrometry used to induce fragmentation of ions by subjecting them to collisions with neutral gas molecules such as Ar gas. It is commonly employed in tandem mass spectrometry experiments, where precursor ions generated in the ion source are selected, accelerated and then fragmented in the collision cell of the instrument, see *Figure 2.4*.

During CID, precursor ions gain internal energy from collisions with the collision gas, leading to the breaking of chemical bonds within the ion. This results in the formation of fragment ions, which can be detected and analyzed to deduce information about the structure and composition of the parent molecule. The fragmentation patterns observed in CID spectra are characteristic of the molecule's structure and can be used for identification and structural elucidation purposes.

CID parameters such as collision energy, collision gas composition, and pressure can be optimized to control the fragmentation process and enhance the selectivity and sensitivity of the analysis. As for this project, collisional induced dissociation occurs in the same region as the IMR but rather than putting in neutral formate, Argon gas is introduced, which will collide with the precursor ion and depending on collision energy, the precursor can fragment leading to product ions. These product ions are then analyzed by the last quadrupole analyzer [40].

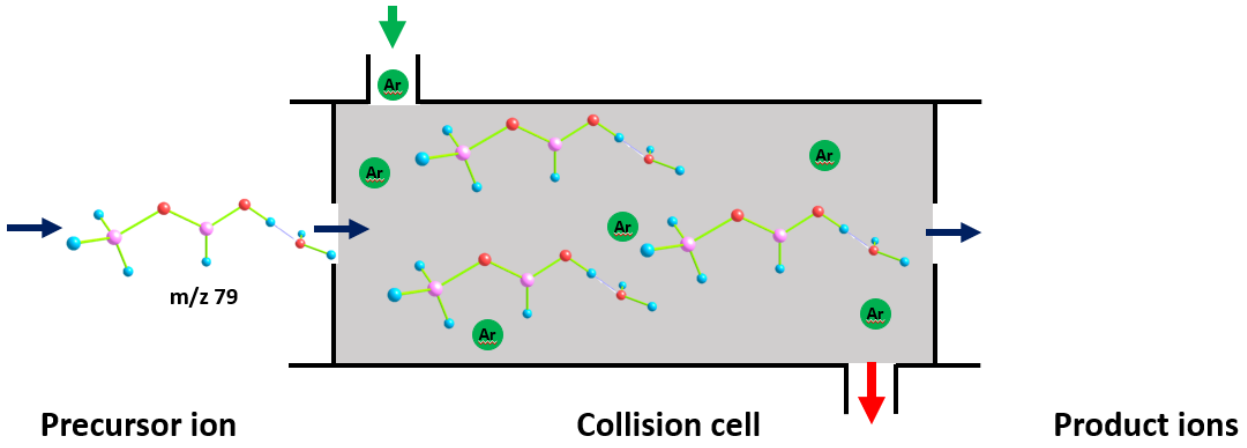

Figure 2.4: Schematic diagram of collision-induced dissociation (CID) using the proton-bound methyl formate/water complex (m/z 79) as an example.

2.3. Magnetic Sector Mass Spectrometry

2.3.1. Electron ionization

Electron ionization (EI) in mass spectrometry operates by generating electrons through the application of current to a wire filament. The intensity of the current dictates the number of electrons emitted. These electrons are then accelerated by an electric field, forming a high-energy beam (*Figure 2.5*). As an analyte molecule traverses this electron beam, a valence shell electron can be dislodged, resulting in the formation of a cation. Unlike processes dependent on molecular

structure, such as electron capture, EI induces ionization by ejecting a valence electron from the analyte molecule. The fast-moving electron, passing close to the molecule, disrupts the electron cloud around it, transferring kinetic energy. Sufficient energy transfer prompts the molecule to expel a valence electron, forming a radical cation ($M^{\bullet+}$) as shown in *Equation 2.2*. With an electron acceleration of 70V, 70 eV EI induces significant fragmentation due to the considerable energy involved.

$$\mathbf{M + e^- \rightarrow M^{+\bullet} + 2e^-} \qquad \mathbf{(2.2)}$$

As a result of ionization, positively charged ions are formed. These ions can be of various types, depending on the target material and the conditions of the ionization process. Once the ions are formed, they can be extracted from the ion source and accelerated into a mass spectrometer for analysis.

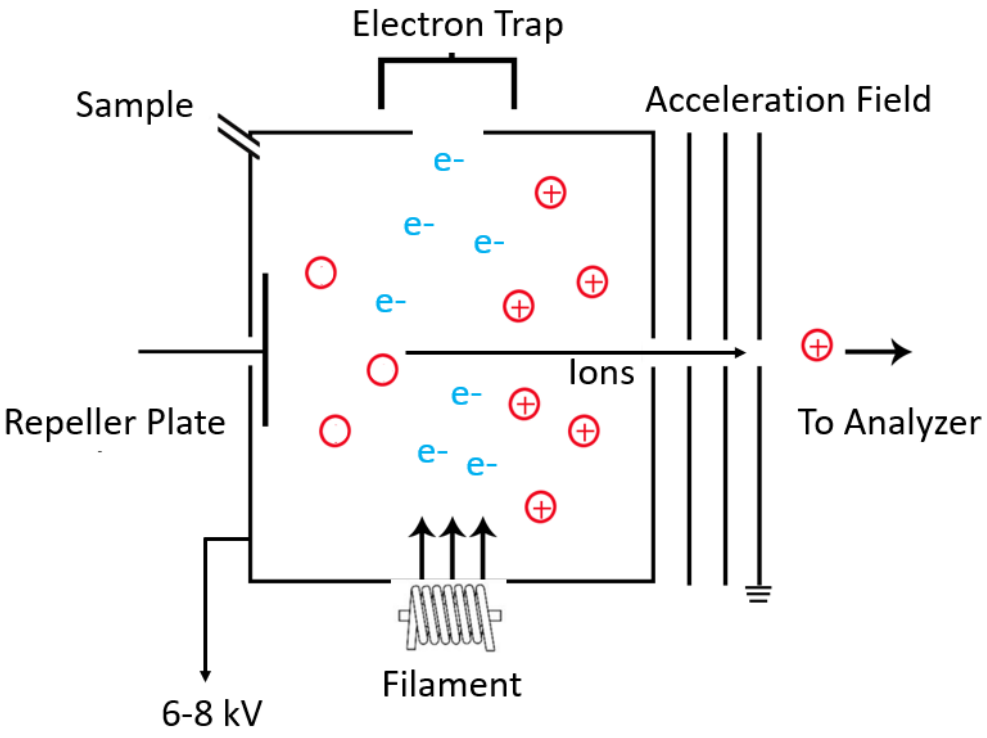

Figure 2.5: Schematic representation of electron ionization.

The speed of this acceleration corresponds to the energy difference between the housing and a grounded plate located just outside. The energy levels employed for this acceleration process are selectively chosen from 6, 7, or 8 kilovolts (kV) depending on the desired timescale for the experiment [41].

2.3.2. Double Focusing Magnetic Sector Mass Spectrometer and the MIKES Experiment

A modified VG-ZAB mass spectrometer has been employed for the investigation of all chloroformates. A schematic representation of how it operates is provided in *Figure 2.6*.

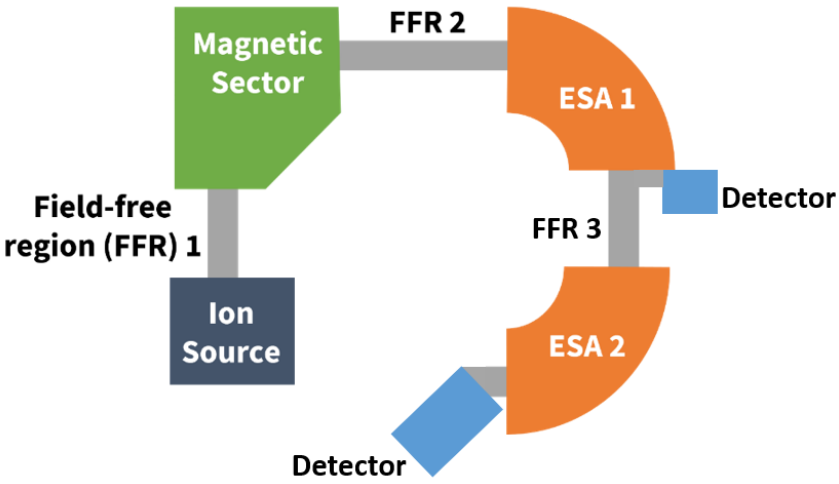

Figure 2.6: Schematic representation of modified VG-ZAB instrument.

A gas chromatography syringe is used to introduce approximately 10 µL of liquid sample into a steel reservoir heated to 100°C, via a septum inlet. The resulting vapor is then transferred to the ion source through a glass capillary inlet heated to 110°C. The pressure in the ion source, measured with an ionization gauge at the top of the turbo pump, typically reads 5 x 10^{-6} mbar, with the pressure in the source itself being at least 100 times higher. To increase the pressure reading to

10^{-4} mbar, methanol is then introduced in the same manner in the ion source, undergoes electron ionization due to its higher abundance, leading to ion-molecule reactions and resulting mass spectral signals. The ions are then accelerated to 8 keV, pass through a field free region (FFR 1) before entering the magnetic sector where they are separated according to mass-to-charge ratio (m/z) and the ion of choice can be selected based on its momentum using the magnetic field (Figure 2.6) [42].

The magnetic sector comprises two electromagnets with a gap between them through which ions travel (*Figure 2.7*). These electromagnets generate a magnetic field between them, facilitating the separation of ions based on their momentum. The relationship between the ion's momentum (mv) and the magnetic field is defined by the formula:

$$\boldsymbol{mv = rBze} \qquad \textbf{(2.3)}$$

Here, *mv* is the ion's momentum (m=mass and v=velocity), *r* is the radius of curvature of the magnetic sector (a constant value), *B* is the magnetic field, *z* is the ion's charge, and *e* is the elementary charge. The fixed radius implies that the only adjustable parameter is the magnetic field. By knowing the momentum of the desired ion, it becomes possible to set the magnetic field at a level that allows only the targeted ion to successfully traverse the curved trajectory [43].

Additionally, the ion's velocity is linked to the acceleration voltage (*V*) through a relationship which can be expressed as:

$$\mathbf{zeV = \tfrac{1}{2}\, m}\boldsymbol{v^2} \qquad \textbf{(2.4)}$$

The mass-to-charge ratio (m/z) for the chosen ions can be determined by combining equations (2.3) and (2.4):

$$\mathbf{m/z} = \frac{\boldsymbol{B^2 r^2 e}}{\mathbf{2v}} \qquad \textbf{(2.5)}$$

The selected ions progress through 2FFR where metastable ions dissociate; that is, those with enough internal energy to do so on the microsecond timescale (with rate constants between 10^3 and 10^6 s^{-1}) [44].

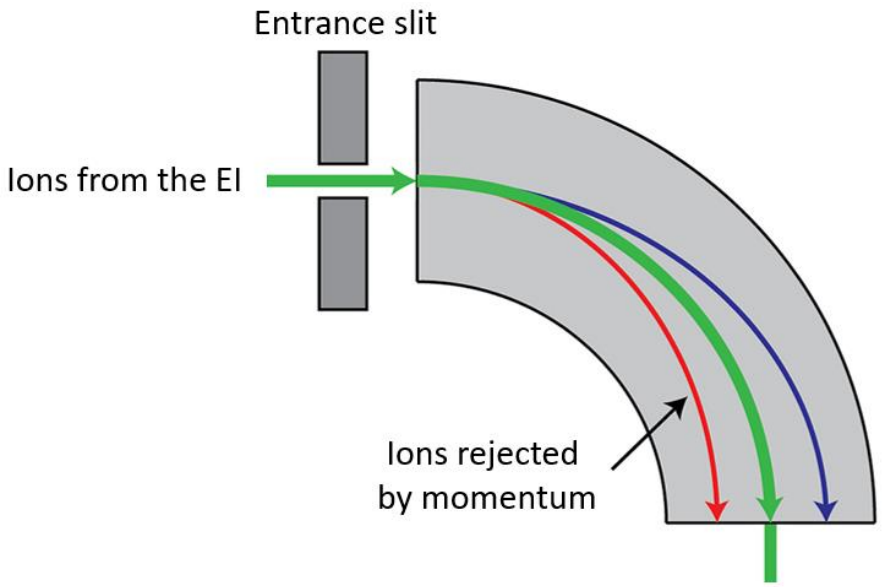

Figure 2.7: Diagram illustrating the magnetic sector and its functionality in the context of mass selection.

Moving on to the next components of the sector instrument, which are electrostatic analyzers (ESA) 1 and 2. These ESAs sectors consist of two curved metal plates with a constant gap between them (*Figure 2.8*).

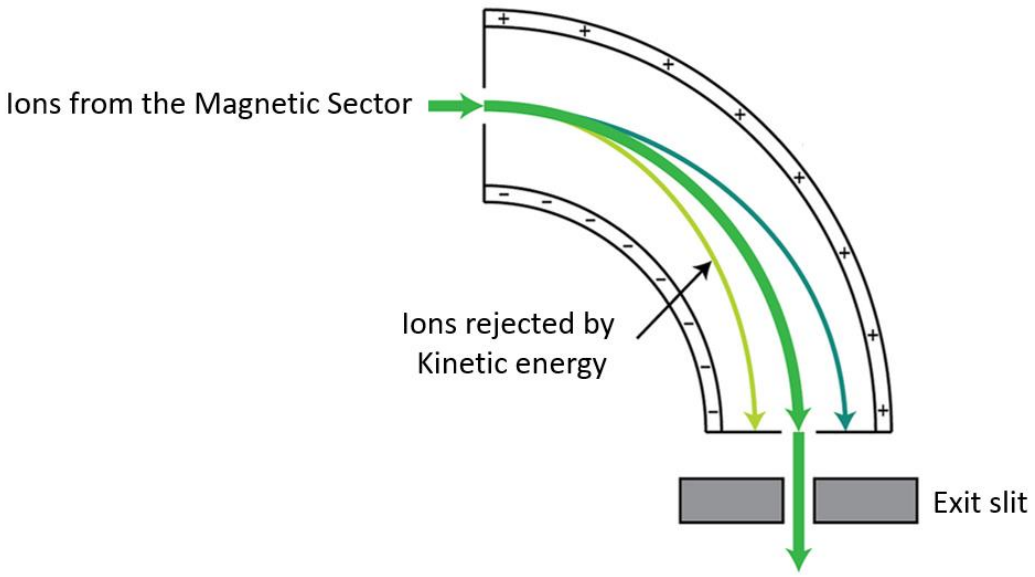

Figure 2.8: Diagram illustrating the electrostatic analyzer and its functionality.

The ions are then subjected to varying potentials on each plate, leading to the generation of an electric field across the gap. This electric field serves to separate the ions based on their kinetic energy. The separation process is governed by the following equation:

$$\tfrac{1}{2}\,\mathbf{m}v^2 = \mathbf{zeV} = \tfrac{1}{2}\,\mathbf{zeEr} \qquad \textbf{(2.6)}$$

Here, *E* represents the electric field. The equation can be rearranged to characterize the ion based on its mass-to-charge ratio (*m*/*z*):

$$\mathbf{m/z} = \frac{eEr}{v^2} \qquad \textbf{(2.7)}$$

The electric field can be configured in two ways: as a constant field, transforming the Electrostatic Analyzer (ESA) into a mass selector, or as a variable field, enabling it to function as a mass filter. The sector instrument's final component is the detector. In the VG-ZAB instrument, a photomultiplier detector, illustrated in *Figure 2.9*, is utilized.

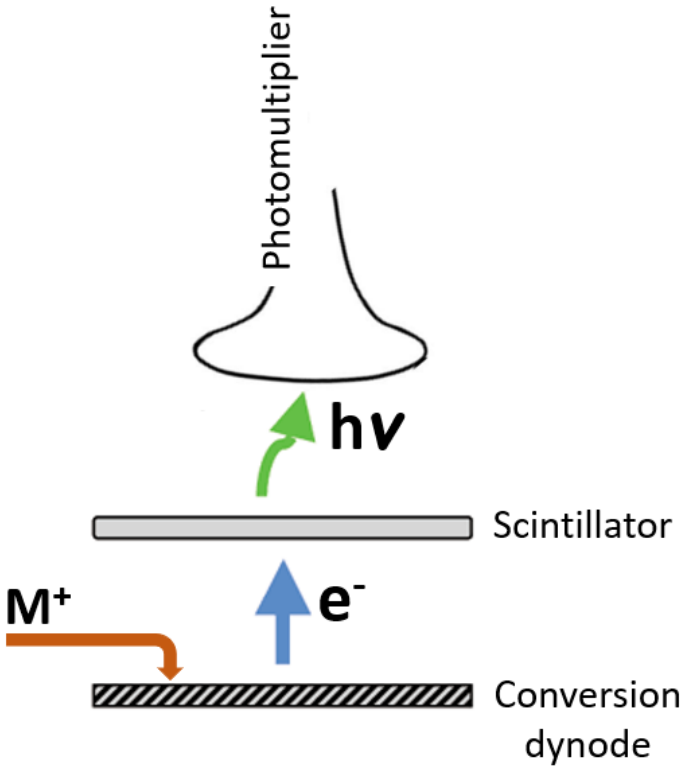

Figure 2.9: Diagram of a Photomultiplier Detector.

The ions undergo collisions with the conversion dynode, leading to the release of an electron. Subsequently, this electron then interacts with the scintillator material, which absorbs the energy of the electron and re-emits it as photons. The photon then travels to a photomultiplier, where the signal undergoes amplification through multiple dynodes. The processed electrical signal is then passed on to the data acquisition system of the mass spectrometer, where it is digitized and recorded. The recorded signal represents the intensity of the emitted photons, which in turn correlates with the abundance of ions reaching the detector. The recorded data is analyzed to generate a mass spectrum, which displays the intensity of ions detected at different mass-to-charge ratios (m/z).

2.4. Computational Methods

2.4.1. Density Functional Theory (DFT) Calculations

Density Functional Theory (DFT) is a computational quantum mechanical modeling method used in physics, chemistry, and materials science to investigate the electronic structure of many-body systems, especially the ground state. Unlike traditional quantum mechanical methods, which solve the many-body Schrödinger equation directly, DFT employs the Kohn-Sham approach [45], which were formulated by Walter Kohn and Lu Sham in 1965, reduces the problem to a set of single-particle equations. The Kohn-Sham equations are a set of equations derived from the Hohenberg-Kohn theorems, which establish the one-to-one correspondence between the ground-state electron density and the external potential of a system,

$$\hat{H}_{KS}\boldsymbol{\psi_i}(\boldsymbol{r}) = \boldsymbol{\epsilon_i}\boldsymbol{\psi_i}(\boldsymbol{r}) \qquad \textbf{(2.8)}$$

where $\hat{H}_{KS}$ is the Kohn-Sham Hamiltonian operator, $\psi_i(\mathbf{r})$ are the Kohn-Sham orbitals, and ϵ_i are the corresponding eigenvalues, representing the orbital energies. The Kohn-Sham Hamiltonian consists of kinetic energy, electron-electron repulsion, and an effective potential term, which depends on the electron density.

These equations represent non-interacting electrons moving in an effective potential, which includes the external potential due to atomic nuclei and the effective potential due to electron-electron interactions. The central idea of DFT is to describe the ground state electronic density of a system rather than the wavefunction of individual electrons, significantly reducing the computational complexity compared to traditional wavefunction-based methods. By focusing on the electron density, DFT calculations become computationally more efficient, making it feasible

to study systems with hundreds or thousands of atoms. Despite its simplifications, DFT has proven to be accurate for a wide range of molecular and condensed matter systems, making it one of the most widely used methods in theoretical chemistry and physics [46,47].

DFT provides valuable insights into molecular structures through a gradient search process. Initial guesses of energy are refined through small adjustments in geometry until an optimized structure within an energy minimum is achieved. This can be a local or global minimum on the potential energy surface (PES), indicating stable geometries. Transition states, crucial in understanding reactions, are defined as saddle points on the PES, being maxima along the reaction coordinate but minima in all other directions [48].

To determine the accurate energy associated with optimized structures, the zero-point energy (ZPE) (the minimum energy of molecular vibrations) is added to the electronic energy.[46] This real minimum energy is vital for calculating reaction energies, such as dissociation energy (ΔE) and ionization energy (IE).

Vibrational frequencies are computed by first determining the potential energy surface (harmonic oscillator model) and then using the Hessian matrix (the second derivative matrix) of the PES at equilibrium. However, in reality, molecular vibrations can exhibit anharmonic behavior, meaning that the potential energy surface is not perfectly quadratic and can deviate from harmonic behavior. The number of frequencies is determined by the molecule's degrees of freedom, with translational and rotational degrees subtracted ($3N - 6$ for non-linear, $3N - 5$ for linear molecules). Experimental frequencies are typically lower, requiring scaling based on empirical factors [49].

Imaginary frequencies in critical frequencies signify transition states, as restorative forces are lacking in those vibrations.

Rotational constants, derived from Density Functional Theory (DFT) calculations, are fundamental parameters used to characterize the rotational motion of molecules. They represent the rotational energy levels of a molecule and are determined by solving the rigid rotor Schrödinger equation, which describes the rotational motion of a molecule as a simple quantum mechanical system.

Geometry optimizations and harmonic vibrational frequency calculations of all species and transition states were conducted using the Gaussian 16 package.[50] In this study, the B3LYP/6-31+G(d,p) level of theory was used since it provides a good balance between a complete basis set and computational efficiency and is used for geometry optimizations as a result. Transition states were confirmed with the intrinsic reaction coordinate (IRC) protocol [51]. Zero-point vibrational energy ZPE correction is included for all calculated energies. To confirm the link between local minima or transition state, harmonic vibrational frequencies were calculated. CBS-QB3 single-point energy calculations have also been performed for all structures to improve accuracy.[50]

2.4.2. Rice–Ramsperger–Kassel–Marcus (RRKM) theory

The foundational framework for comprehending the rates of unimolecular reactions was primarily formulated in the first half of the twentieth century [52]. The Lindemann–Hinshelwood mechanism, introduced in 1922 by Lindemann and later refined by Hinshelwood, suggested that gas-phase unimolecular reactions initiate through bimolecular collisions [53]. This formulation enabled the calculation of reaction rates as a function of internal energy, irrespective of the activation method. In the subsequent decade, Rice and Ramsperger, alongside Kassel independently, enhanced this

model, resulting in the Rice–Ramsperger–Kassel (RRK) model [54,55]. The RRK model treated the molecule as a system of identical harmonic oscillators and introduced the concept of activation energy, stipulating that specific modes of motion must accumulate sufficient energy for the reaction to proceed. In 1952, Rice and Marcus expanded this into the Rice–Rampsberger–Kassel–Marcus theory (RRKM), incorporating a more comprehensive quantum mechanical description and introducing the concept of the transition state [56]. The RRKM model, which calculates reaction rates based on these computed structures, continues to be the prevailing scientific framework for understanding unimolecular chemical kinetics.

This thesis focuses on discussing unimolecular dissociation reactions, specifically those following the type:

$$\boldsymbol{A^* \xrightarrow{k} A^{\ddagger} \rightarrow P} \qquad \textbf{(2.9)}$$

where A^* represents an excited molecule, k is the rate constant for dissociation, $A^{\ddagger}$ is the transition state (TS) of A, and P denotes the dissociation products [57]. DFT (Density Functional Theory) is employed to compute optimized and transition state structures, allowing for correlation with experimental results.

Chemical transformations involve breaking bonds in reactants and forming new bonds in products. The potential energy associated with these changes defines an n-dimensional potential energy surface (PES), where n is the number of atoms. The reaction pathway is a one-dimensional section of the PES comprising the precursor, intermediates, transition states, and products of a specific reaction. Reactants and intermediates correspond to minima, while transition states are located at maxima along the reaction pathway [58].

The reaction rate hinges on the probability of the molecule adopting conformations along the reaction pathway, which, in turn, relies on the probability of sufficient energy being distributed into the necessary modes of motion. RRKM theory is noteworthy for incorporating Transition State Theory (TST), assuming that once the reaction reaches the transition state or dividing surface, it will inevitably proceed to form products, and internal vibrational energy redistribution (IVR) is fast compared to the reaction timescale [59]. Under these constraints, the RRKM microcanonical rate constant [60,61], k(E), is expressed as:

$$\boldsymbol{k(E) = \frac{\sigma N^{\ddagger}(E-E_0)}{h\rho(E)}} \qquad \textbf{(2.10)}$$

where E is the internal energy of the system, E_0 is the 0K activation energy for the reaction, $N^{\ddagger}(E-E_0)$ is the sum of internal states of the transition state at an internal energy from E_0 to E, $\rho(E)$ is the density of states of the precursor at an internal energy E, h is Planck's constant, and σ is the degeneracy of the reaction pathway [54-56]. A state is defined as any unique vibrational configuration determining the internal energy of the molecule. The sum of states, $N(E)$, is the total number of states within a specific energy range.[58] The density of states is the number of states per energy level and is expressed in units of inverse energy (E^{-1}), while the sum of states is dimensionless. Thus, the microcanonical rate constant has units of s^{-1}. $N^{\ddagger}(E-E_0)$ and $\rho(E)$ can be computed based on DFT-calculated structures for the precursor, considering vibrational frequencies and rotational constants, using the Beyer and Swinehart direct count algorithm.

For nonlinear polyatomic molecules, there are 3n-6 vibrational frequencies, and for the corresponding transition state, there are 3n-7 vibrational frequencies. The values of these frequencies, typically ranging from 50-3500 cm^{-1}, dictate how internal energy is distributed in the molecule. The calculation of the sum and density of states depends on these frequencies, which

can be measured or obtained from standard data tables. However, for transition states, these values must be estimated or, more commonly, calculated using theoretical packages.

CHAPTER 3. THE INTERACTION OF METHYL FORMATE WITH PROTON-BOUND SOLVENT CLUSTERS IN THE GAS PHASE AND THE UNIMOLECULAR CHEMISTRY OF THE REACTION PRODUCTS

Published as Diedhiou, Malick & Mayer, Paul M. (2023). The Interaction of Methyl Formate with Proton-Bound Solvent Clusters in the Gas Phase and the Unimolecular Chemistry of the Reaction Products. Applied Sciences, 13, 1339. doi:org/10.3390/app13031339.

3.1. Introduction

Volatile organic carbon (VOC) compounds in the atmosphere play a role in climate change, human and animal health, and oxidation capacity [62]. The results obtained from a 2020 study measuring the concentrations of various VOCs in Burnaby South and Port Moody (part of Greater Vancouver) and analyzing the factors contributing to their production showed that fuel combustion, natural gas, industrial solvents, and fugitive industrial, and biogenic emissions, are the main sources that contribute to all VOC emissions [63].

Methyl formate is a small ester derived from formic acid or formate. It can undergo a series of reactions in the troposphere initiated by the hydroxy radical and other atmospheric radicals [64]. In oxygenated fuels such as dimethyl ether and dimethoxy methane, which are two of the fuels that have been suggested as alternatives to conventional diesel fuel [65-67], methyl formate represents

the major intermediate formed in their oxidation. It has also been shown to interact with atmospheric water [68]. The mechanisms for organic molecule incorporation into water clusters include switching, association, and proton transfer [65]. When formates interact with water molecules, the carbonyl group leads to further hydrogen bonding interactions. The shape and bonding strength of the cluster is altered, making it more stable overall. These findings make it clear that organic esters like formates play a role in nucleation processes due to their ability to share intermolecular interactions with water [69,70]. Ion–molecule reactions are one method for exploring the reaction between formates and water clusters [71]. Proton-bound water clusters are widely used as reactant ions for the analysis of volatile organic compounds through mass spectrometry [72]. Also, it is quite common to produce protonated analyte molecules using proton-bound water clusters [73,74]. Herein, we present details of ion–molecule reactions between proton-bound solvent clusters of water, methanol and ethanol with neutral methyl formate in the gas phase. Reaction products have been further explored with collision-energy resolved tandem mass spectrometry to understand their unimolecular chemistry.

3.2. Materials and Methods

Water, methanol, ethanol, and methyl formate were purchased from Sigma Aldrich (Sigma-Aldrich, Oakville, Ontario, CA) and used without further purification.

3.2.1. Tandem Mass Spectrometry

A Micromass Quattro Ultima triple quadrupole mass spectrometer running the MassLynx software package equipped with an electrospray ionization (ESI) source in a Z-spray configuration was used for all the experiments described herein. Ionic clusterswere generated by electrospray ionization

of solutions of each solvent with 0.1% formic acid delivered by a syringe pump at a rate of 50 μL/min. The capillary voltage was typically set to 3.5 kV but was adjusted to optimize ion yield. Nitrogen was used as the nebulizer gas with a flow rate of 100 L/hour. The source and desolvation gas temperatures were held at 100 and 150 °C, respectively. The desired proton-bound cluster ion was mass-selected with the first quadrupole and transmitted to the collision cell where it interacted with methyl formate vapour introduced by a variable leak Granville-Phillips valve [75]. The voltage at the entrance and exit of the collision cell was set at 50 V to provide an extraction voltage for the derived reaction products, which were mass-analyzed with the second quadrupole and detected with a continuous dynode electron multiplier.

Collision-induced dissociation (CID) experiments were carried out by first forming the desired ion in the electrospray source from a 1 mg/mL solution of methyl formate in the solvent, mass selecting it with the first quadrupole, and performing collisions with argon target gas in the collision cell as a function of lab frame collision energy (generally between 0 and 26 eV for all the CID experiments) [76].

3.2.2. Computational Methods

All calculations were carried out using the GAUSSIAN 16 suite of programs [51]. Structures were optimized using the B3LYP density functional method with the 6-311+G(d,p) basis set [77,78]. Transition states were confirmed by the intrinsic reaction coordinate method in GAUSSIAN. Rice-Ramsperger-Kassel-Marcus (RRKM) theory was applied to calculate *k(E)* according to the following equation [60,79]:

$$\boldsymbol{k(E) = \frac{\sigma N^{\ddagger}(E-E_0)}{h\rho(E)}} \qquad \textbf{(3.1)}$$

where σ represents the reaction degeneracy, h is Planck's constant, $N^{\ddagger}(E - E_0)$ is the number of internal states for the transition state at internal energy $(E - E_0)$ and $\rho(E)$ is the density of states for the reactant ion at internal energy (E) as calculated via the Beyer and Swinehart direct count algorithm [80]. Our previous work modeling energy-resolved CID data employed a simple model in which the post-collision ions are assigned an effective temperature depending on the centre-of-mass collision energy, and thus a "thermal" internal energy distribution, according to the relationship:

$$\boldsymbol{T_{eff} = T_i + \alpha E_{com}} \qquad \textbf{(3.2)}$$

where T_i represents the initial temperature (300 K in the current study) and α describes the relationship between the centre-of-mass collision energy (E_{com}) and the increase in the effective temperature (T_{eff}). This assumption limits the model to a purely semi-quantitative one for comparisons of related systems [81,82].

3.3. Results

3.3.1. Solvent Cluster Ion / Methyl Formate Reactions

Representative mass spectra resulting from the ion-molecule reactions R1-R5 of proton-bound solvent clusters and neutral methyl formate (MF) are shown in *Figure 3.1*. Water = W, methanol = M, ethanol = E, and methyl formate = MF.

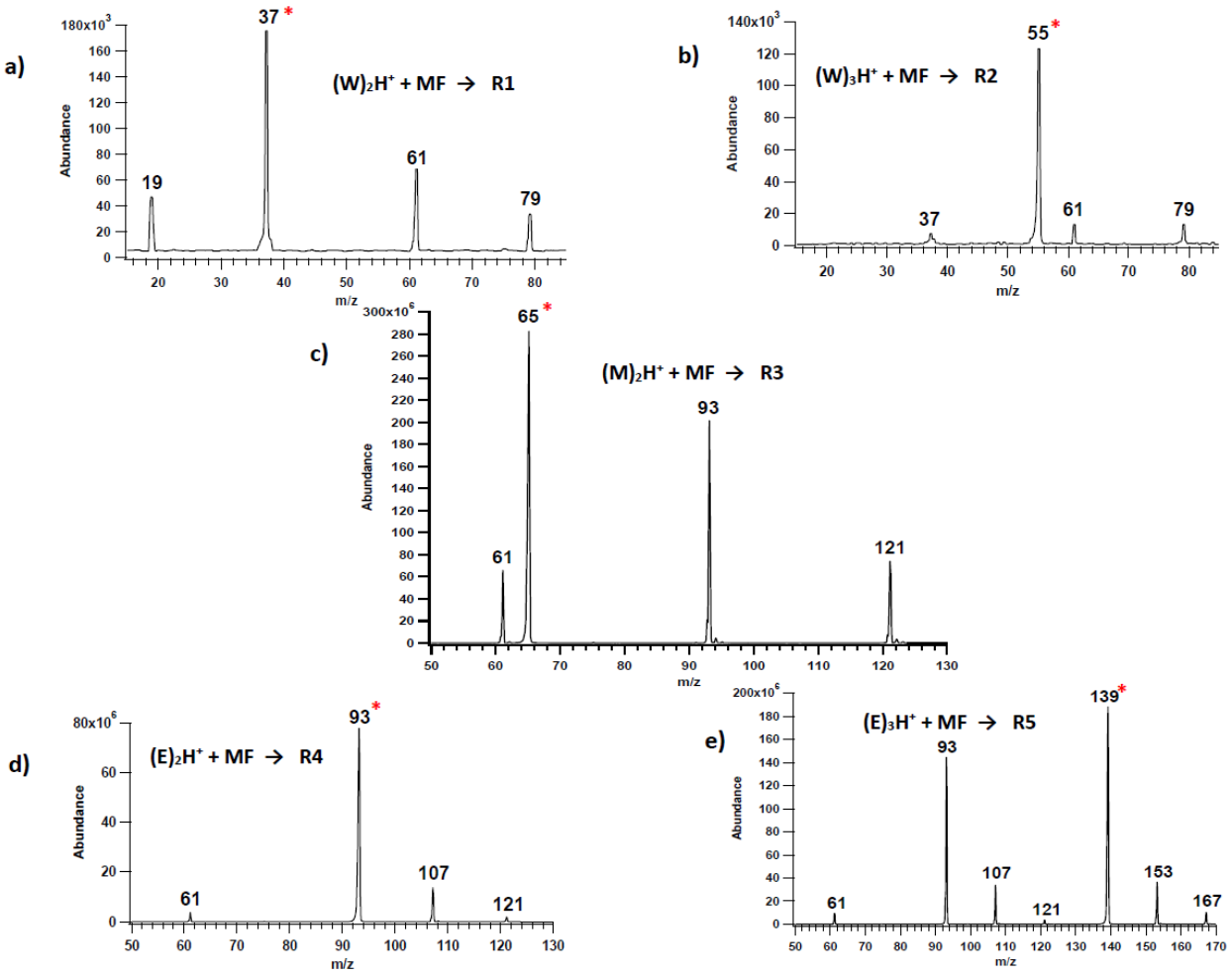

Figure 3.1: Representative mass spectra of neutral methyl formate reacting with a) water dimer ion (m/z 37, **R1**), b) water trimer ion (m/z 55, **R2**), c) methanol dimer ion (m/z 65, **R3**), d) ethanol dimer ion (m/z 93, **R4**), and e) ethanol trimer ion (m/z 139, **R5**).

The mass spectra recorded from the reaction between methyl formate and water dimer ion (**R1**) showed several peaks: m/z 79, which represent the proton-bound water-methyl formate complex; m/z 61, which would nominally be protonated methyl formate, and m/z 19 ion due to WH^+. The overall reaction scheme is summarized in *Figure 3.2a* at the B3LYP/6-311+G(d,p) level of theory. Formation of the encounter complex is exothermic by 1.31 eV, and the resulting loss of W exothermic by 0.53 eV (relative to the reactants), which means the encounter complex is not

observed in the experiment. Based on the relative energies, WH^+ is most likely to arise from the dissociation of the initial $(W)_2H^+$complex, as it would not be competitive to generate it from $MF(W)H^+$.

Similar peaks are observed in the ion-molecule reaction with the proton-bound water trimers ion (m/z 55) and from all of the solvent cluster ion reactions, *Figures 3.1*. In each case the initial encounter complex is not observed because the low binding-energy (*Figure 3.2*) results in a high enough rate constant for dissociation that there is not enough time or pressure to collisionally-stabilize the complex. Evident from the computational results summarized in *Figure 3.2* is that the highest binding energy encounter complex is $MF(E)_2H^+$, 0.89 eV, but this is still not enough to allow it to be observed. RRKM calculations were performed for the solvent loss reaction from each encounter complex and the resulting k(E) vs E curves are compared in *Figure S3.1*. For example, the calculated dissociation energy for the $MF(W)_2H^+$ complex is 0.78 eV. The rate constant for the dissociation is greater than 1×10^6 s^{-1} only 0.2 eV above this threshold. In a thermal system, the encounter complexes have an internal energy distribution that extends to between 0.60 and 1.00 eV (*Figure S3.2*), which means that they would be stable species at atmospheric pressure.

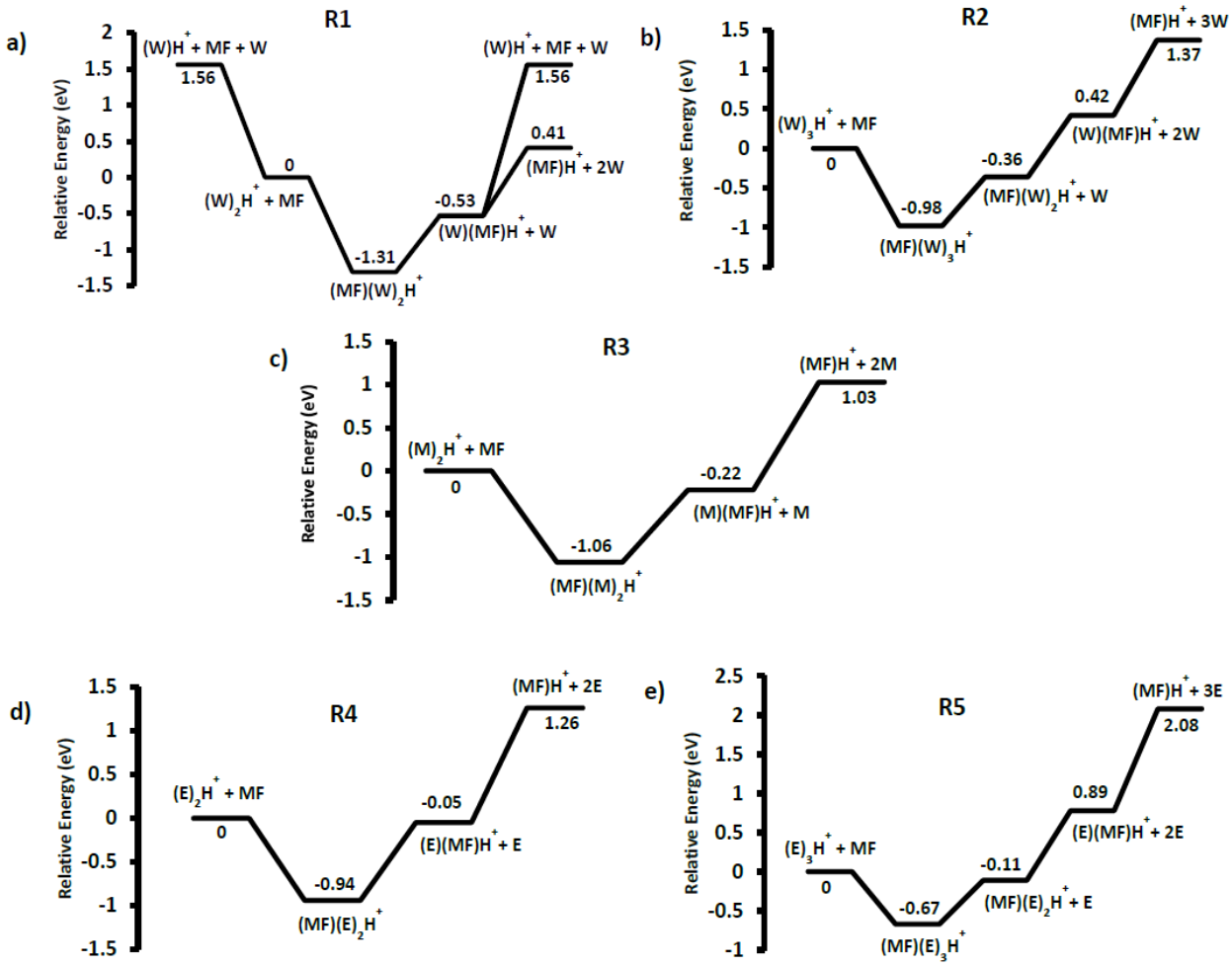

Figure 3.2: Relative energy (B3LYP/6-311+G(d,p)) of the major product ions resulting from the reaction between neutral methyl formate with a) the water cluster dimer and b) the water cluster trimer, c) the methanol dimer, d) the ethanol dimer and e) the ethanol trimer.

Also observed in the reactive mass spectra, aside from those shown in *Figure 3.2* are secondary reactions of protonated MF and dissociation products of the solvent cluster ions themselves (*Table S3.1*).

3.3.2. Unimolecular Reactions of Proton-Bound Solvent-MF clusters

The most common primary reaction products discussed above are the proton-bound complexes between MF and a solvent molecule. We were able to independently generate $MF(W)H^+$, $MF(M)H^+$, $MF(E)H^+$, $MF(M)_2H^+$, $MF(E)_2H^+$, and $MF(E)_3H^+$ in the electrospray source and obtain CID breakdown curves for each. They are shown in *Figures 3.3* and *3.4* along with initial assignments. A common dissociation product is protonated methyl formate as expected from the ion-molecule reaction results in *Figure 3.1*. We have previously investigated the unimolecular chemistry of MFH^+ and it leads to the formation of m/z 33 (loss of CO to form protonated methanol) [83]. In the case of $MF(M)H^+$ a competing loss of CH_4 is observed, which could form either a proton-bound complex between M and CO_2, $M(CO_2)H^+$, or MF and OH, $MF(OH)^+$. For $MF(E)H^+$, the similarity in the proton affinity (PA) of MF and E (782.5 kJ mol^{-1}) and (776.4 kJ mol^{-1}, respectively) [84] leads to competing cleavage of both sides of the hydrogen bond, *Figure 3.3c*.

The $MF(M)_2H^+$ cluster ion dissociates by sequential loss of both M molecules. A minor channel involves the loss of MF from the initially formed MF(M)H+ product ion, *Figure 3.4a*. As was observed with the $MF(E)H^+$ dimer ion, the $MF(E)_2H^+$ trimer ion exhibits competitive loss of E and MF, with the tetrameric $MF(E)_3H^+$ ion undergoing sequential E loss.

Evident from the breakdown curves is that these cluster ions undergo facile decomposition. In each case (except $MF(E)_2H^+$) there is significant dissociation between 0 and 0.5 eV E_{COM}. Thus, even under the high-pressure limit of 1 atm, these ions can decompose.

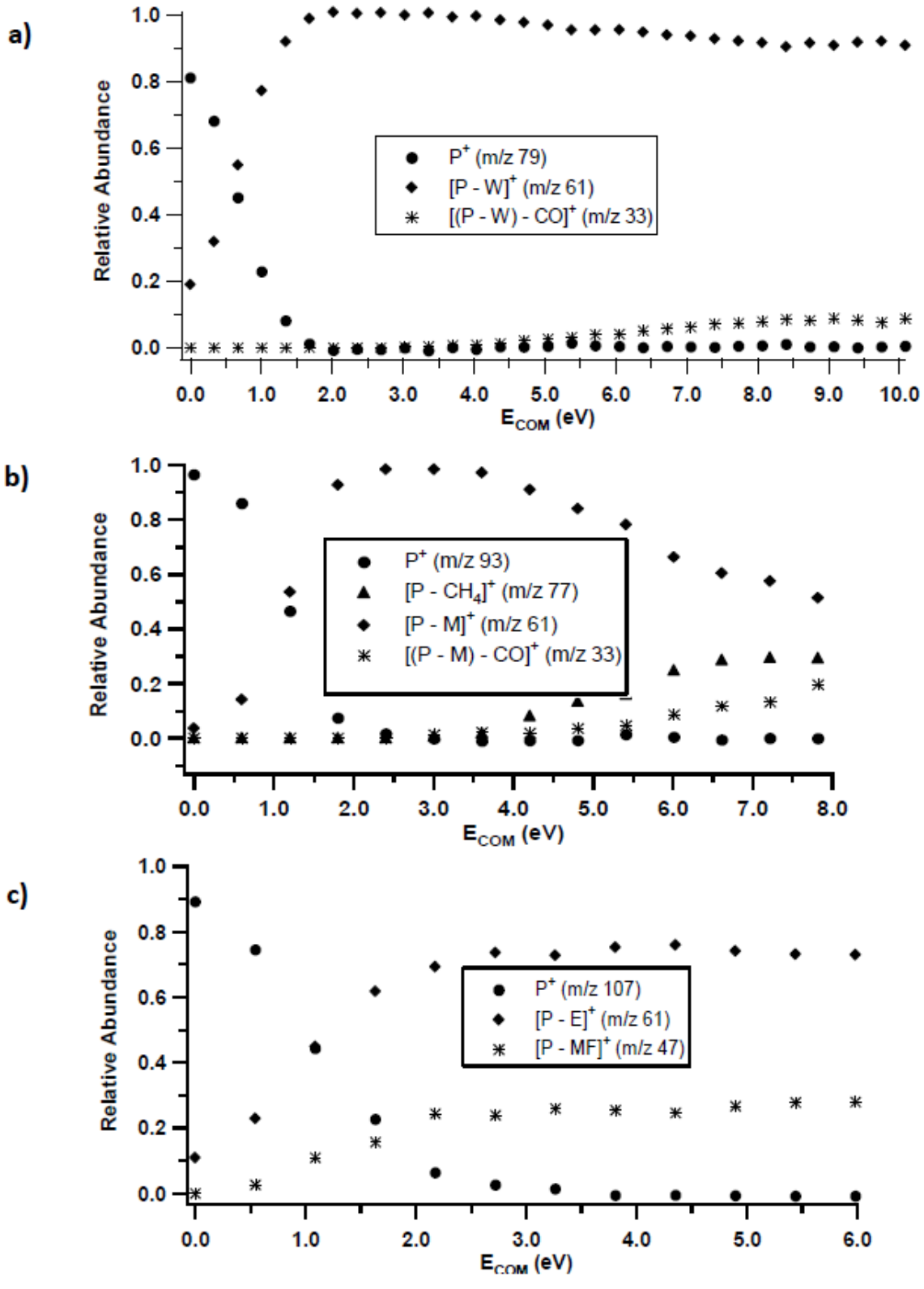

Figure 3.3: CID breakdown curves of a) $P^+ = MF(W)H^+$, b) $P^+ = MF(M)H^+$, and c) $P^+ = MF(E)H^+$.

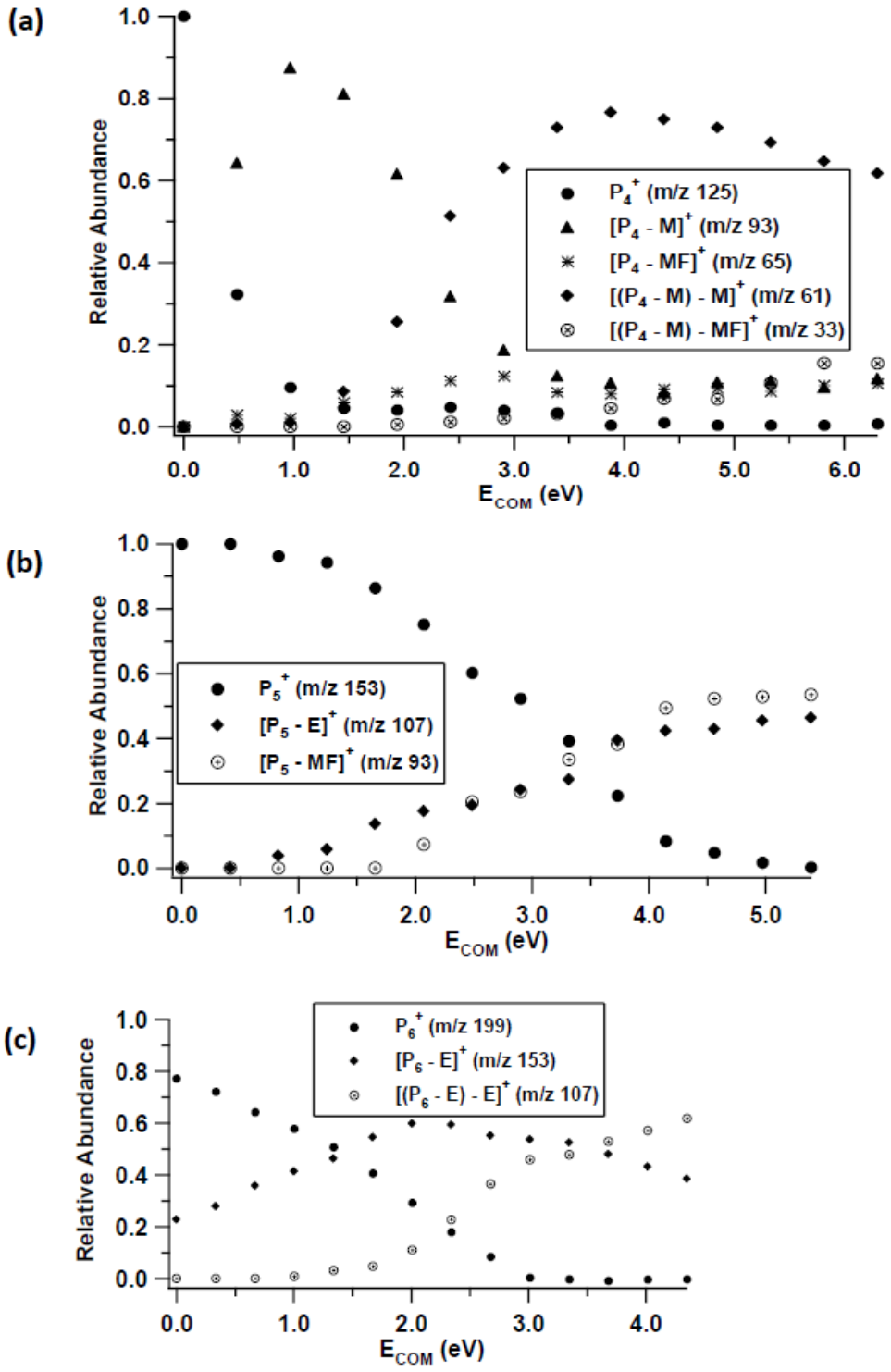

Figure 3.4: CID breakdown curves of a) $P^+ = MF(M)_2H^+$, b) $P^+ = MF(E)_2H^+$ and c) $P^+ = MF(E)_3H^+$.

The primary unimolecular reaction of these complexes is simple dissociation of a hydrogen bond. Relaxed potential energy scans of this dissociation for two examples, $MF(W)H^+$ and $MF(E)_3H^+$, were carried out to explore the potential for reverse activation barriers due to the possible structural rearrangement of the complexes, *Figure 3.5*. Evident from both scans is that these encounter complexes can easily fragment without a reverse barrier, which means the relative product energies in *Figure 3.2* direct the relative abundance of the competing reactions.

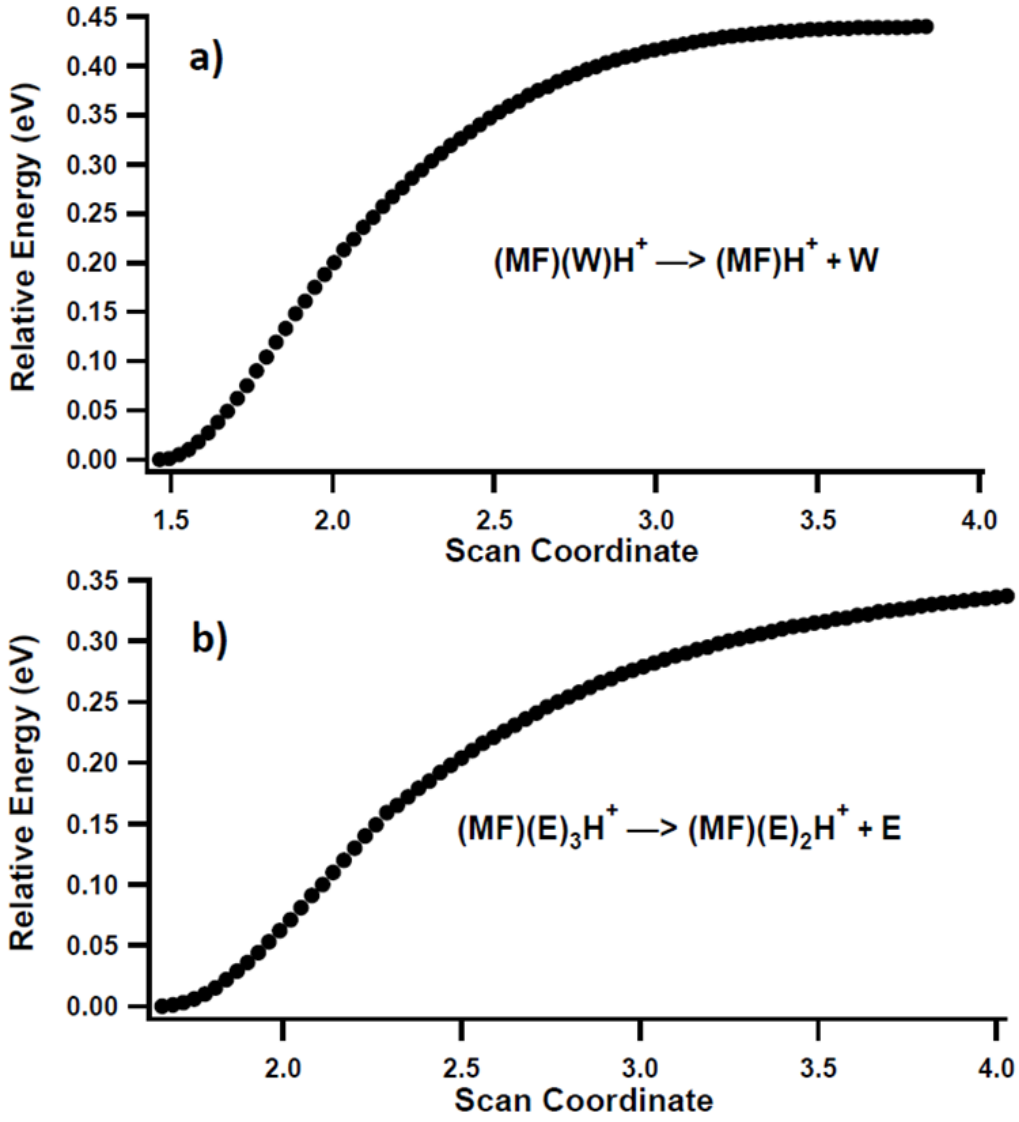

Figure 3.5: relaxed potential energy scan of the dissociation of $MFWH^+$ and $MF(E)_3H^+$ at the B3LYP/6-311+G(d,p) level of theory.

Unique among the clusters is $MF(M)H^+$, which undergoes a loss of CH_4. This reaction was explored computationally, and the reaction pathway is shown in *Figure 3.6* in comparison to the simple loss of methanol (and subsequent dissociation of MFH^+). The MF methyl group first pulls away from the complex leading to the TS at 1.98 eV. It then interacts with the carbon H atom on the central HOC(H)O moiety leading to a molecule of methane. Due to the low binding affinity of the methane to the resulting ionic complex, it is very mobile and can wander the skeleton. The methane complex shown in *Figure 3.6* at -0.49 eV only has a binding energy of 0.2 eV. The competing loss of methanol via a barrierless H-bond cleavage results in MFH^+, which is due to the higher proton affinity of methyl formate (782.5 kJ mol^{-1}) compared to methanol (754.3 kJ mol^{-1}) [25], having an energy requirement of 1.25 eV. The MFH^+ then dissociates by loss of CO [83]. The barrier heights to CH_4 loss vs M loss are consistent with the breakdown diagram that shows M loss to be the lower energy-threshold pathway.

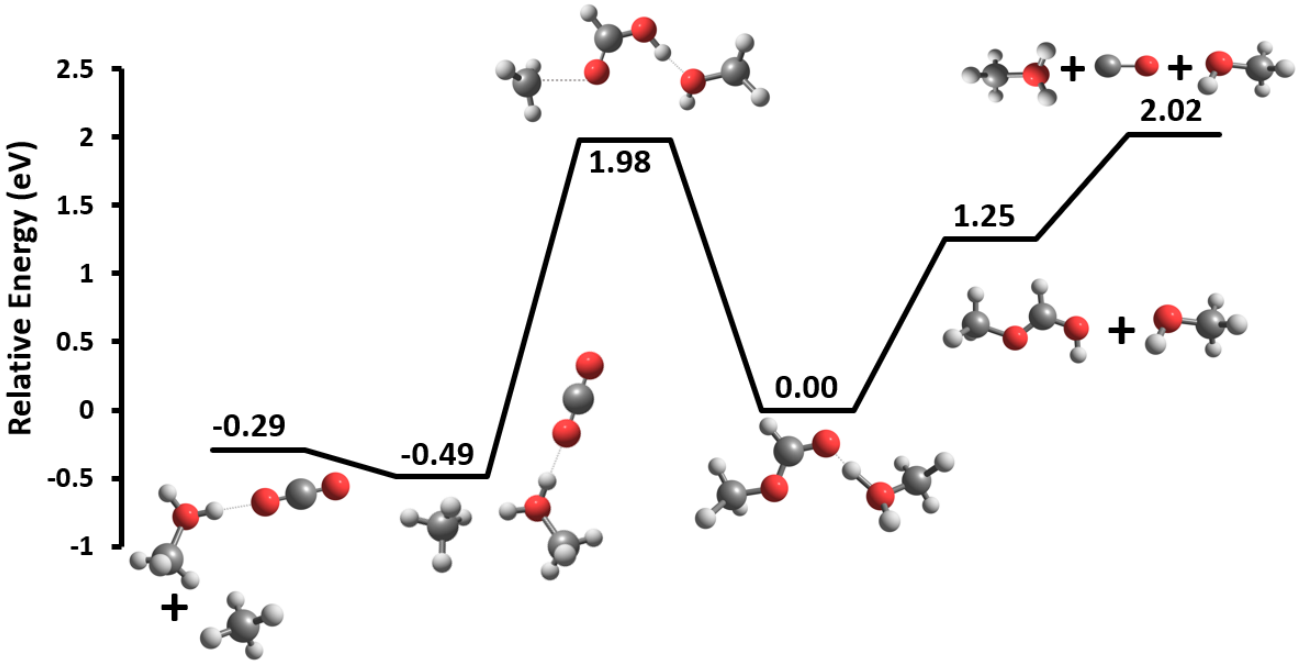

Figure 3.6: B3LYP/6-311+G(d,p) minimum energy reaction pathways surface for the dissociation of $MF(M)H^+$ (m/z 93).

The breakdown diagrams in *Figures 3.3* and *3.4* were modeled with the approach outlined in the computational procedures that is based on assigning an internal temperature to the post-collisions ions, followed by adjusting the RRKM rate constant for each unimolecular reaction. The results are shown in *Figure S3.3*. As anticipated from the model, the results are not in quantitative agreement with the reaction energies in *Figure 3.2*, but there are qualitative comparisons. In the case of the competing methane loss channel from $MF(M)H^+$ (*Figure 3.6*), the modeled difference in E_0 for the two reactions is 0.32 eV, compared to the calculated difference of 0.73 eV. As expected, the RRKM estimated difference in E_0 for competing MF and E loss from $MF(E)H^+$ is ~ 3 kJ mol^{-1} compared to the difference in proton affinity of MF and E of 6 kJ mol^{-1}. For the trimeric precusor ions, the RRKM estimated E_0 values for the dissociation channels are in much better agreement with the theoretical estimates in *Figure 3.2*. The results are summarized in *Table 1*.

Table 3.1: Comparison of the RRKM estimated reaction energies[1] (*Figure S3.3*) with those calculated values shown in *Figure 3.2*.

Reaction	RRKM E_0	Theoretical E_0
$MF(W)H^+ \rightarrow MFH^+ + W$	0.34	0.94
$MF(M)H^+ \rightarrow MFH^+ + M$	0.58	1.25
$\rightarrow M(CO_2)H^+ + CH_4$	0.90	1.98
$MF(E)H^+ \rightarrow MFH^+ + E$	0.53	1.21
$\rightarrow EH^+ + MF$	0.56	1.49
$MF(M)_2H^+ \rightarrow MF(M)H^+ + M$	0.77	0.84
$\rightarrow (M)_2H^+ + MF$	0.85	1.06
$MF(E)_2H^+ \rightarrow MF(E)H^+ + E$	0.87	0.89
$\rightarrow (E)_2H^+ + MF$	0.88	0.94
$MF(E)_3H^+ \rightarrow MF(E)_2H^+ + E$	0.64	0.56

[1] Values listed in eV.

3.4. Conclusions

Ion molecule reactions between methyl formate and proton-bound solvent clusters of water, methanol and ethanol demonstrate that the primary reaction product is the formation of protonated methyl formate due to its higher proton affinity than water, methanol, and ethanol. Loss of a solvent molecule from the encounter complex occurs in a barrierless reaction in all cases. In a higher energy, minor reaction, the complex between methyl formate and methanol also undergoes loss of methane which forms a proton-bound complex between methanol and CO_2. The results support the conclusion that when methyl formate interacts with atmospheric water, the encounter complexes (which were not observed in this experiment due to the low pressure in the reaction chamber) should be moderately stable at high (atmospheric) pressure as demonstrated by their calculated internal energy distributions. Protonated methyl formate will result, which can then undergo loss of CO [83].

3.5. Appendix

Table S3.1: Additional reactions observed in the ion-molecule reactions explored in this study. Energies calculated at the B3LYP/6-311+G(d,p) level of theory.

$(W)_3H^+$ (m/z 55) → $(W)_2H^+$ (m/z 37) + W	**ΔE= 0.95 eV**
$(MF)H^+$ (m/z 61) + MF (m/z 60) → $(MF)_2H^+$(m/z 121)	**ΔE=-1.34 eV**
$(MF)_2H^+$ (m/z 121) + E (m/z 46) → $(MF)_2(E)H^+$ (m/z 167)	**ΔE=-0.86 eV**
$(E)_3H^+$ (m/z 139) → $(E)_2H^+$ (m/z 93) + E	**ΔE= 0.83 eV**

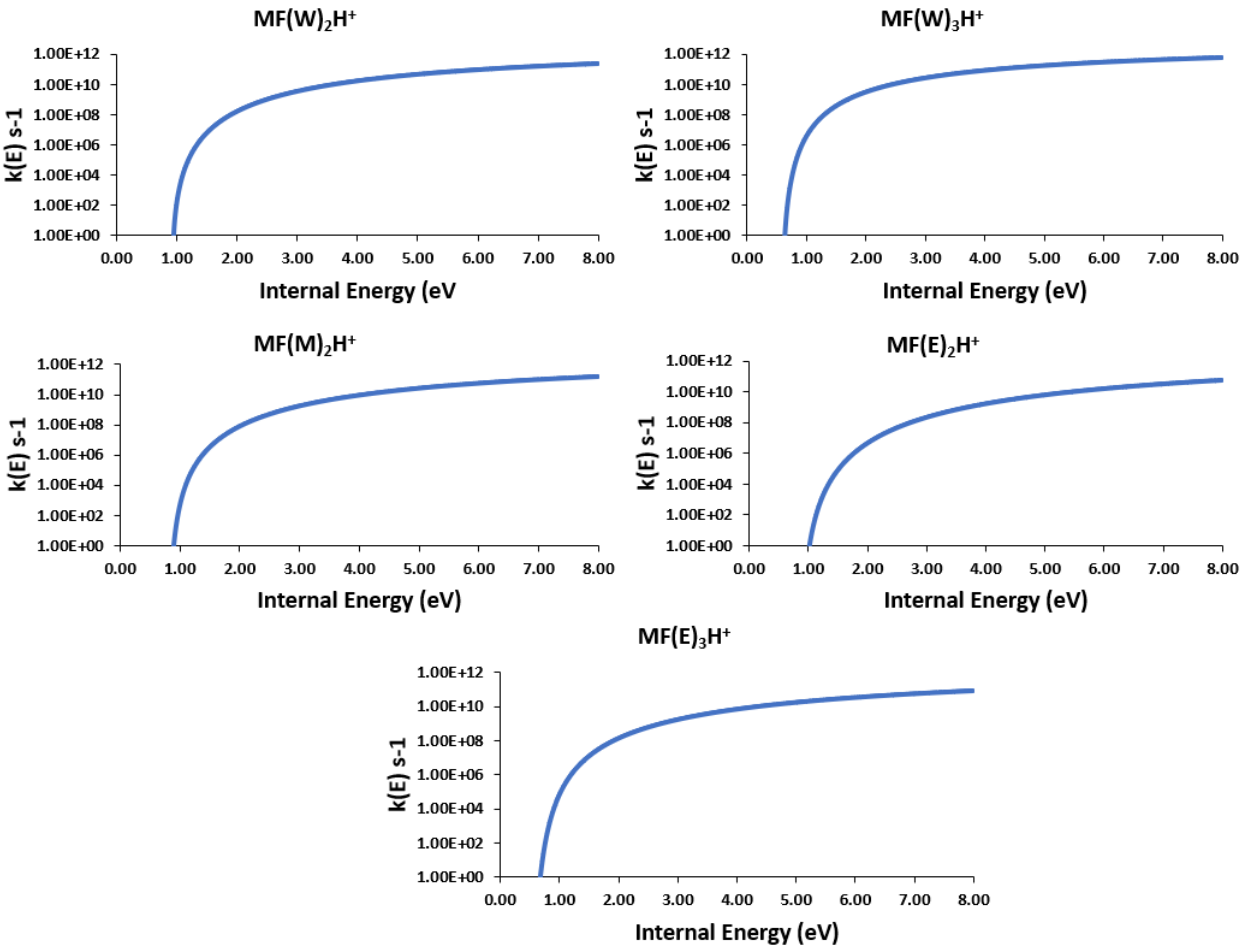

Figure S3.1: RRKM k(E) vs E curves for the dissociation of the ion-molecule encounter complexes.

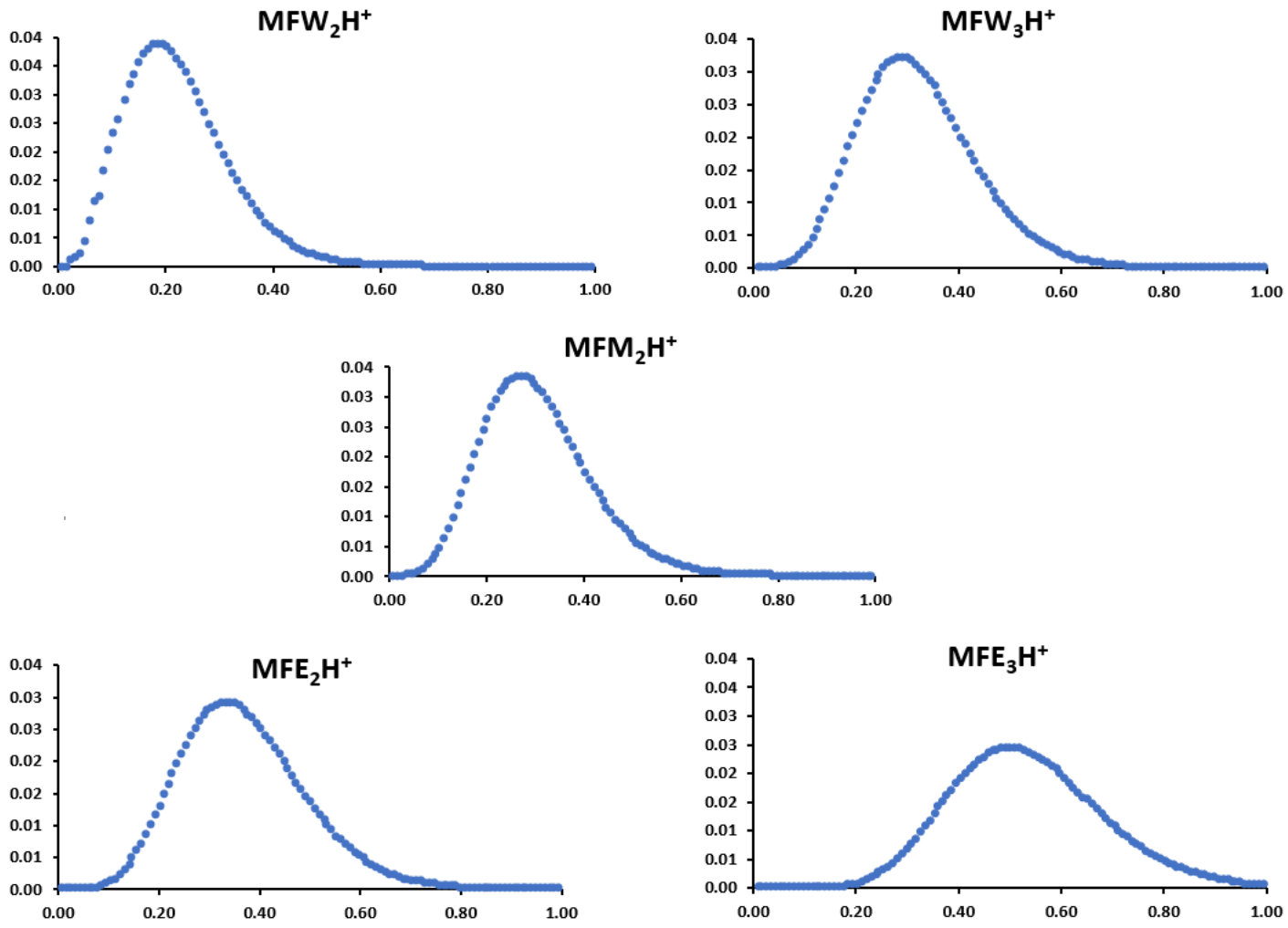

Figure S3.2: Vibrational internal energy distributions at 300 K for the encounter complexes in **R1-R5**.

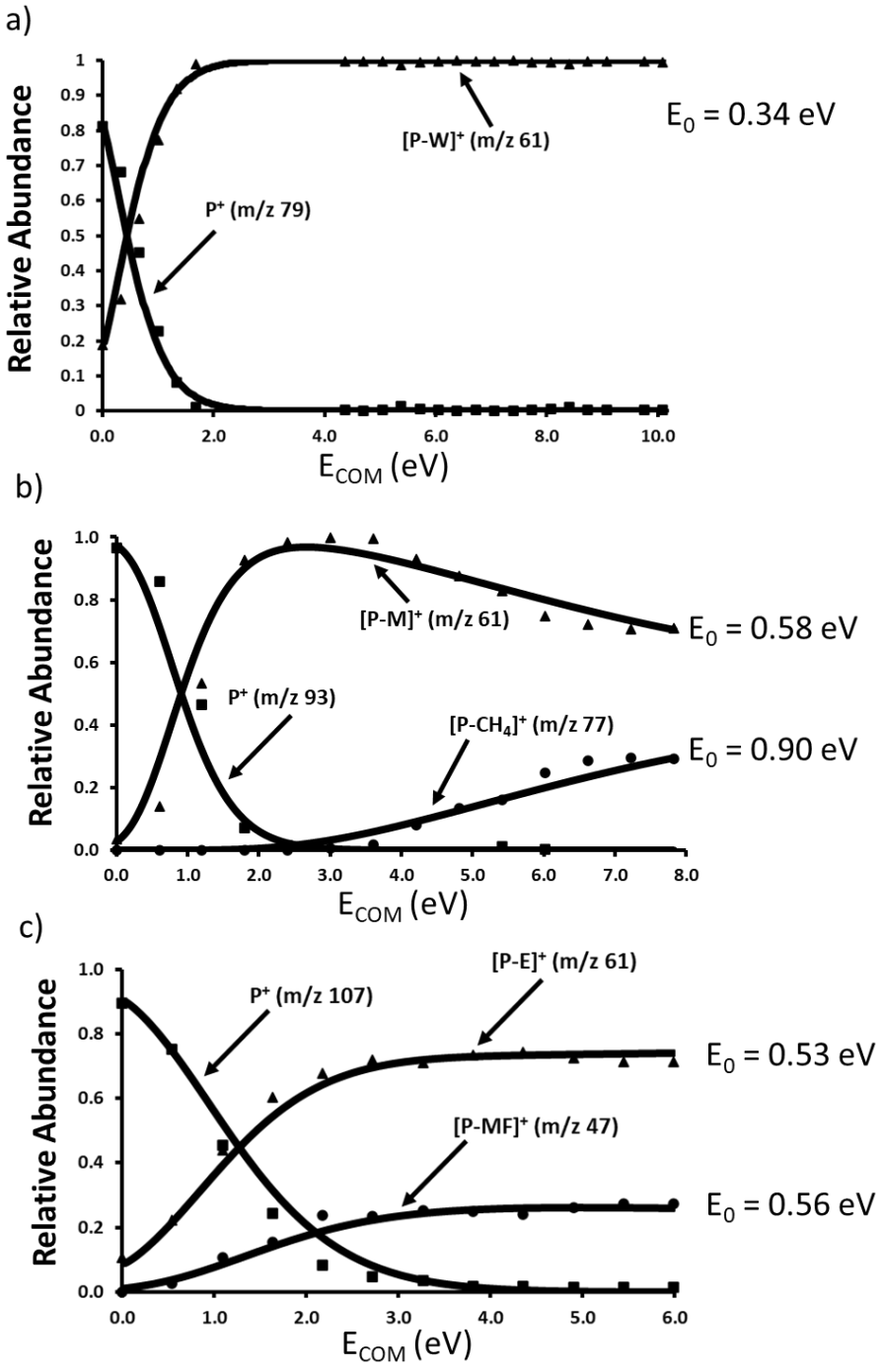
a)
Relative Abundance
[P-W]+ (m/z 61)
P+ (m/z 79)
E0 = 0.34 eV
ECOM (eV)
b)
Relative Abundance
[P-M]+ (m/z 61)
P+ (m/z 93)
[P-CH4]+ (m/z 77)
E0 = 0.58 eV
E0 = 0.90 eV
ECOM (eV)
c)
Relative Abundance
[P-E]+ (m/z 61)
P+ (m/z 107)
[P-MF]+ (m/z 47)
E0 = 0.53 eV
E0 = 0.56 eV
ECOM (eV)

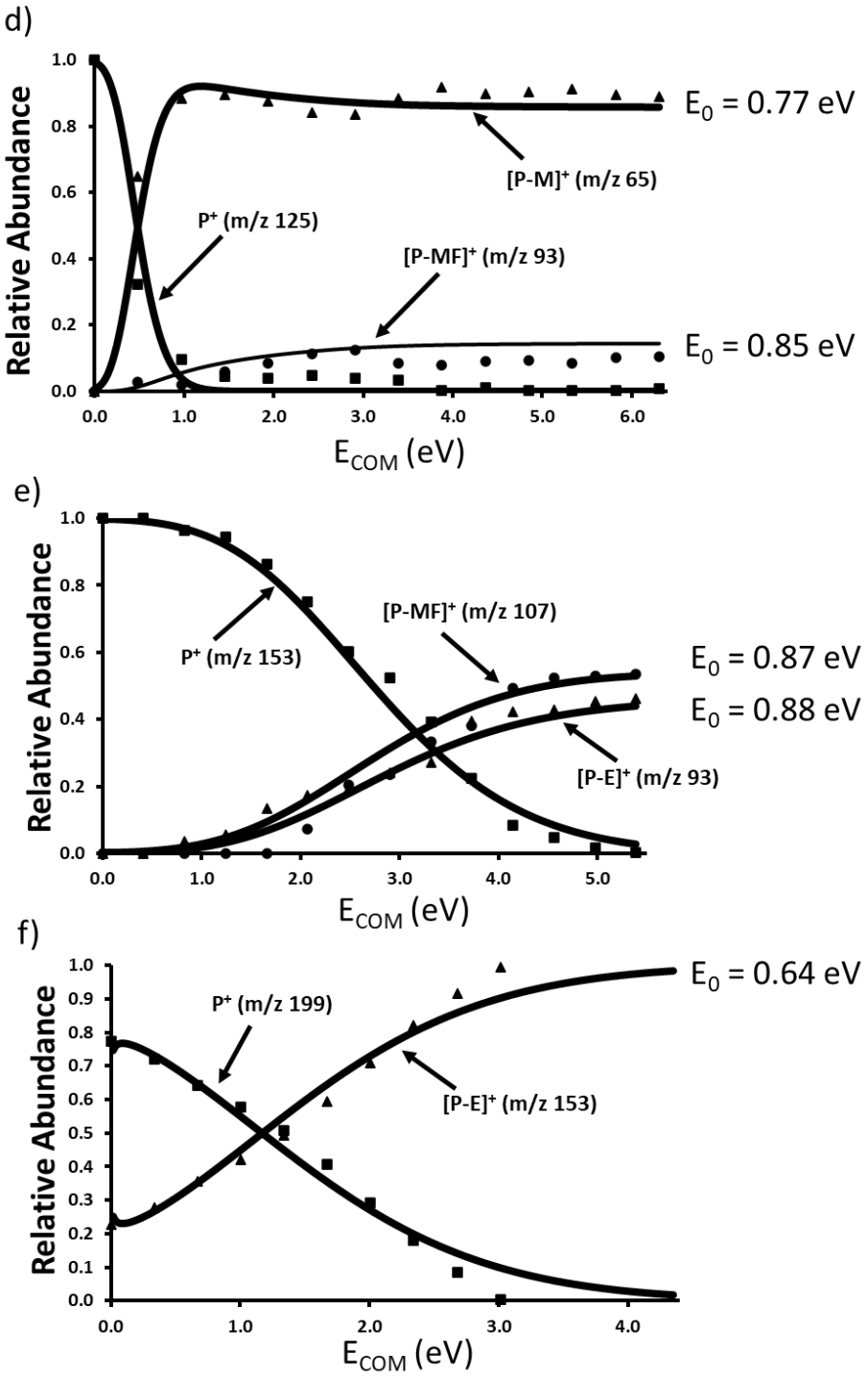

Figure S3.3: RRKM modeled breakdown curves for reactions in Figures 3.3 and 3.4. To accommodate the model, sequential reactions (such as loss of H_2O from m/z 33 in Figure 3.3a) were summed into the primary product ion abundance.

CHAPTER 4. ON THE GAS-PHASE INTERACTIONS OF ALKYL AND PHENYL FORMATES WITH WATER: ION-MOLECULE REACTIONS WITH PROTON-BOUND WATER CLUSTERS

Published as Diedhiou, Malick & Mayer, Paul M. (2023). On the Gas-Phase Interactions of Alkyl and Phenyl Formates with Water: Ion-Molecule Reactions with Proton-Bound Water Clusters. Molecules, 28, 4431 (11 pages). doi:org/10.3390/molecules28114431.

4.1. Introduction

Small water clusters are believed to play a crucial role in the catalysis of atmospheric chemical reactions [85]. Studies have shown that clusters of different sizes (W_n, where n represents the number of water molecules in the cluster) can interconvert through fast equilibration [3,10]. The ability of water molecules to act both as hydrogen bond donors and acceptors allows water clusters in the atmosphere to catalyze a plethora of chemical reactions by stabilizing intermediates and reducing transition state free energies. These reactive species are responsible for downstream atmospheric reactions such as the oxidation of reactive organic carbon (ROC) and volatile organic carbon (VOC) [86,87].

ROCs and VOCs are chemicals released from industrial processes or generated from the burning of fossil fuels and are known contributors to atmospheric pollution. However, the specific contributions of various ROC and VOC species, and the factors affecting their concentrations, are still not yet fully understood [63,88]. Generally, VOCs are known to be important carcinogens and important gaseous precursors in the photochemical generation of ozone in the troposphere. The importance of VOCs in the atmosphere and their ability to affect climate change, their health effects, and oxidation capacity has already been discussed and studied extensively [89]. Cluster ions containing water and small ROCs and VOCs have been an area of interest in atmospheric chemistry for over 30 years [18,90].

Formates compounds are known to be one of the most abundant oxygen-rich species in the atmosphere. Known sources of these species include industrial solvents, biogenic sources, secondary oxidation, biomass burning, and vehicle exhaust (incomplete combustion and fuel additives) [24,91-93]. After being emitted, formate-derived esters can undergo a range of chemical reactions in the atmosphere, including a series of oxidation reactions in the troposphere initiated by oxidants, notably the hydroxyl radical [29,64,83,94-96]. The nature of the water cluster, specifically its hydrogen-bonding, allows the prediction that the reaction between a water cluster and a ROC species should involve three main steps: the formation of the pre-reactive complex (RC), formation of the product complex (PC), and lastly dissociation to ultimately form a protonated ROC [97].

Herein, we aimed to explore the interaction of a series of atmospherically relevant formates, ethyl formate (EF), isopropyl formate (IF), tertbutyl formate (TF) and phenyl formate (PF), with proton-bound water clusters $(H_2O)_2H^+$ and $(H_2O)_3H^+$ using reactive tandem mass spectrometry. The unimolecular dissociation pathways for some of the generated reactive complexes were explored experimentally with collision-induced dissociation (CID) mass spectrometry and computationally with density functional theory.

4.2. Experimental Procedures

4.2.1. Chemicals

Water, ethyl formate, isopropyl formate, t-butyl formate and phenyl formate were purchased from Sigma Aldrich (Sigma-Aldrich, Oakville, Ontario, CA) and used without further purification.

4.2.2. Tandem Mass Spectrometry

All the studies reported herein was performed using a Micromass Quattro Ultima triple quadrupole mass spectrometer running the MassLynx software system and outfitted with an electrospray ionisation (ESI) source in a Z-spray configuration. For ion-molecule reactions, proton-bound water clusters $(H_2O)_2H^+$ and $(H_2O)_3H^+$ were generated in the electrospray source by delivering to the electrospray probe pure water (W6-1 Water, LOT 222746) with a syringe pump at a flow rate 50 μL/min. The capillary voltage was typically set to 3.5 kV but was adjusted to optimize ion yield. Nitrogen was used as the nebulizer gas with a flow rate of 100 L/hour. The source and desolvation gas temperatures were held at 120 and 150 °C, respectively. The desired proton-bound water cluster ion was mass-selected with the first quadrupole and transferred to the collision cell where it interacted with the chosen formate vapour introduced via a variable leak Granville-Phillips valve

[75]. The voltage at the entrance and exit of the collision cell was set at 50 V to give an extraction voltage for the derived reaction products, which were analyzed with the second quadrupole and continuous dynode electron multiplier detector. The resolution for both mass-selecting quadrupoles was set in the software to 17 yielding baseline resolution of neighbouring masses.

Collision-induced dissociation (CID) experiments were carried out by first creating the desired ions in the electrospray source from a 1 μL/mL solution of formate in water. The ion of interest was mass selected with the first quadrupole and transmitted to the collision cell where it underwent collisions with argon target gas as a function of lab frame collision energy, E_{LAB} (generally between 0 and 30 eV, in 1 eV increments, for all the CID experiments). The argon target gas was kept at a pressure reading of 9.26 x 10^{-6} mbar. For these experiments, the entry and exit potentials of the collision cell were set to 0 V so that the lab frame collision energy better reflected the actual translational energy of the ions. Products of the CID process were determined by scanning the last quadrupole [98]. Data was processed into breakdown curves by plotting the relative peak abundance in each mass spectrum as a function of centre-of-mass collision energy, E_{COM}. The latter was derived from the standard equation [98].

$$\boldsymbol{E_{COM} = E_{LAB}\left(\frac{m_{Ar}}{m_{Ar}+m_i}\right)} \qquad \textbf{(4.1)}$$

Where m_{Ar} is the mass of argon and m_i is the mass of the colliding ion.

4.2.3. Computational Methods

The GAUSSIAN 16 software package was used for all calculations [51]. The B3LYP hybrid density functional was employed along with the 6-311+G(d,p) basis set for all equilibrium

geometry optimisations, harmonic vibrational frequency calculations and transition state optimisations [77,78]. The intrinsic reaction coordinate approach in GAUSSIAN was used to confirm all the transition states. Kinetics calculations employed the standard Rice-Ramsperger-Kassel-Marcus (RRKM) equation for the microcanonical rate constant, k(E) [60,79].

$$\boldsymbol{k(E) = \frac{\sigma N^{\ddagger}(E-E_0)}{h\rho(E)}} \qquad \textbf{(4.2)}$$

where σ represents the reaction degeneracy, h is Planck's constant, $N^{\ddagger}(E - E_0)$ is the number of internal states for the transition state at internal energy $(E - E_0)$ and $\rho(E)$ is the density of states for the reactant ion at internal energy (E) as calculated via the Beyer and Swinehart direct count algorithm [80]. For the qualitative comparisons in this study, vibrational sums and densities of states were employed in the RRKM calculations in the harmonic approximation. Once the RRKM k(E) rate curves were obtained, branching ratios were calculated as a function of centre-of-mass collision energy. Our previous work modeling energy-resolved CID data employed a simple model in which the post-collision ions are assigned an effective temperature depending on the centre-of-mass collision energy, and thus a "thermal" internal energy distribution, according to the relationship:

$$\boldsymbol{T_{eff} = T_i + \alpha E_{com}} \qquad \textbf{(4.3)}$$

where T_i represents the initial temperature (300 K in the current study) and α describes the relationship between the centre-of-mass collision energy (E_{com}) and the increase in the effective temperature (T_{eff}). This assumption limits the model to a purely semi-quantitative one for comparisons of related systems only [81,82].

4.3. Results and Discussion

4.3.1. Water Cluster Ion / Formate Reactions

Figures 4.1 and *4.2* display representative mass spectra from ion-molecule reactions **R1**–**R8** between proton-bound water clusters (dimers and trimers) and neutral ethyl, isopropyl, t-butyl and phenyl formate. Water = W, ethyl formate = EF, isopropyl formate = IF, t-butyl formate = TF and phenyl formate = PF.

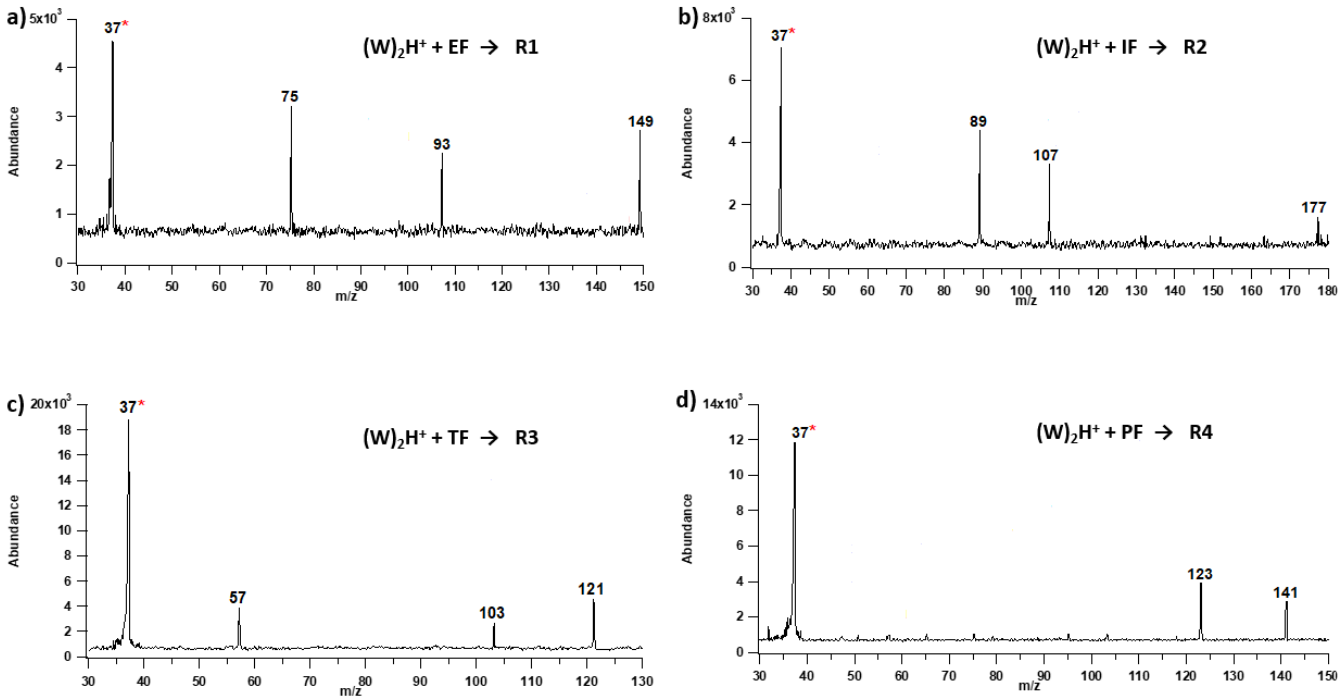

Figure 4.1: Representative mass spectra of water dimer ion (m/z 37, highlighted with the *) reacting with neutral a) EF (74 Da, **R1**), b) IF (88 Da, **R2**), c) TF (102 Da, **R3**), d) and PF (122 Da, **R4**).

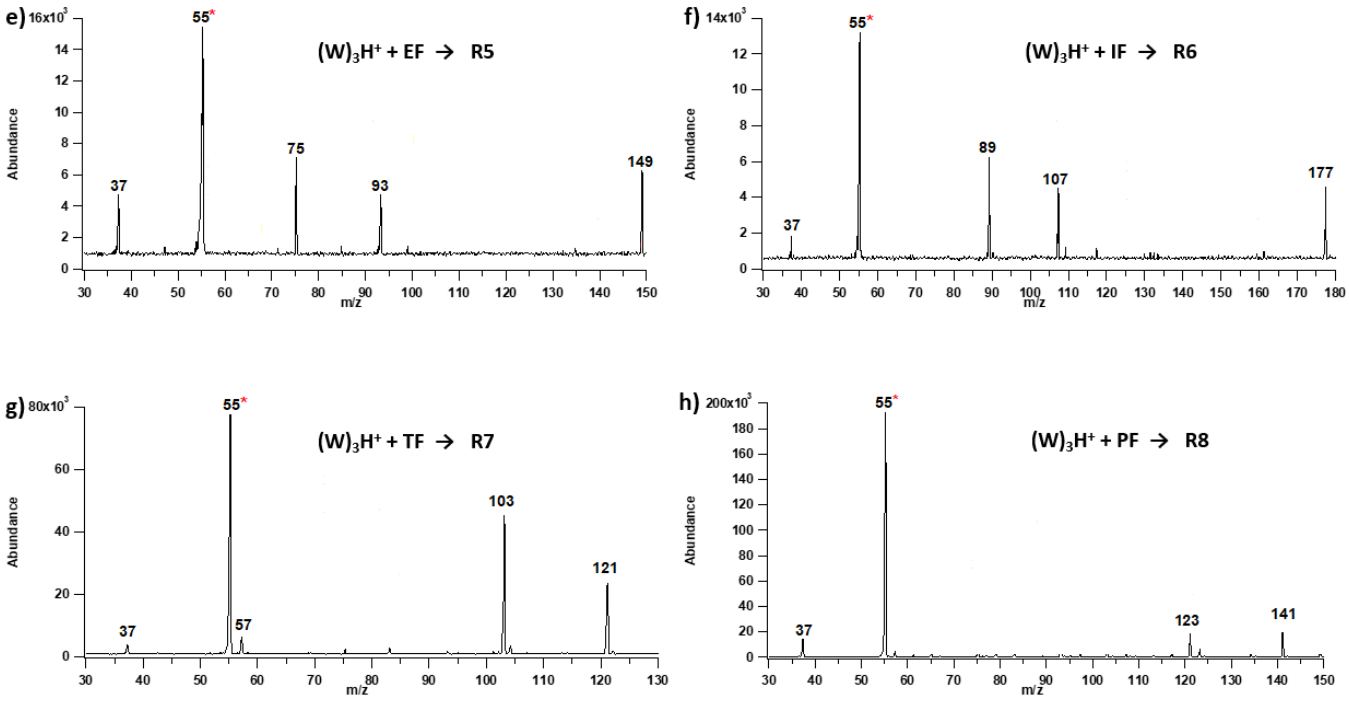

Figure 4.2: Representative mass spectra of water trimer ion (m/z 55, highlighted with the *) reacting with neutral a) EF (74 Da, **R5**), b) IF (88 Da, **R6**), c) TF (102 Da, **R7**), and d) PF (122 Da, **R8**).

The mass spectra from the reaction between water dimer ions and ethyl formate (**R1**) revealed multiple peaks, including m/z 93, which is the proton-bound water-ethyl formate complex; m/z 75, which would nominally be protonated EF; and m/z 149 representing the proton-bound EF dimer, $(EF)_2H^+$. The observation of protonated formate and the proton-bound formate-water complex was common to all reactions. For TF, also observed was m/z 57, which is likely the t-butyl cation, a known fragment of protonated TF [83]. Interestingly, another abundant fragment of TFH^+, m/z 71 (TFH^+ - CH_3OH) was not observed. The relative energy of the reaction products for the formation and dissociation of the encounter complexes were calculated at the B3LYP/6-311+G(d,p) level of theory and are shown in *Figure 4.3*.

The encounter complexes are not visible in the experiment because their formation is exothermic by 1.40 eV, 1.48 eV, 1.36 eV and 1.32 eV (for EF, IF, TF and PF, respectively) and the resulting loss of W is exothermic by 0.66 eV, 0.76 eV, 0.90 eV and 0.57 eV (compared to the reactants), respectively for EF, IF, TF and PF. According to the relative energies, it is most likely that any observed WH^+ results from the dissociation of the original $(W)_2H^+$ complex since it would not compete favourably from $EF(W)H^+$ $IF(W)H^+$, $TF(W)H^+$ or $PF(W)H^+$ due to the low energy for the loss of water as a neutral molecule.

Similarly, *Figure 4.2* shows representative mass spectra resulting from the ion-molecule reactions of each formate with the proton-bound water trimer ions (m/z 55). The same reaction products are observed from the trimer as were observed from the reactions with the dimer. In each case the dominant products are the protonated formate and the proton-bound formate-water complex. For EF and IF, the proton-bound formate dimer is also observed.

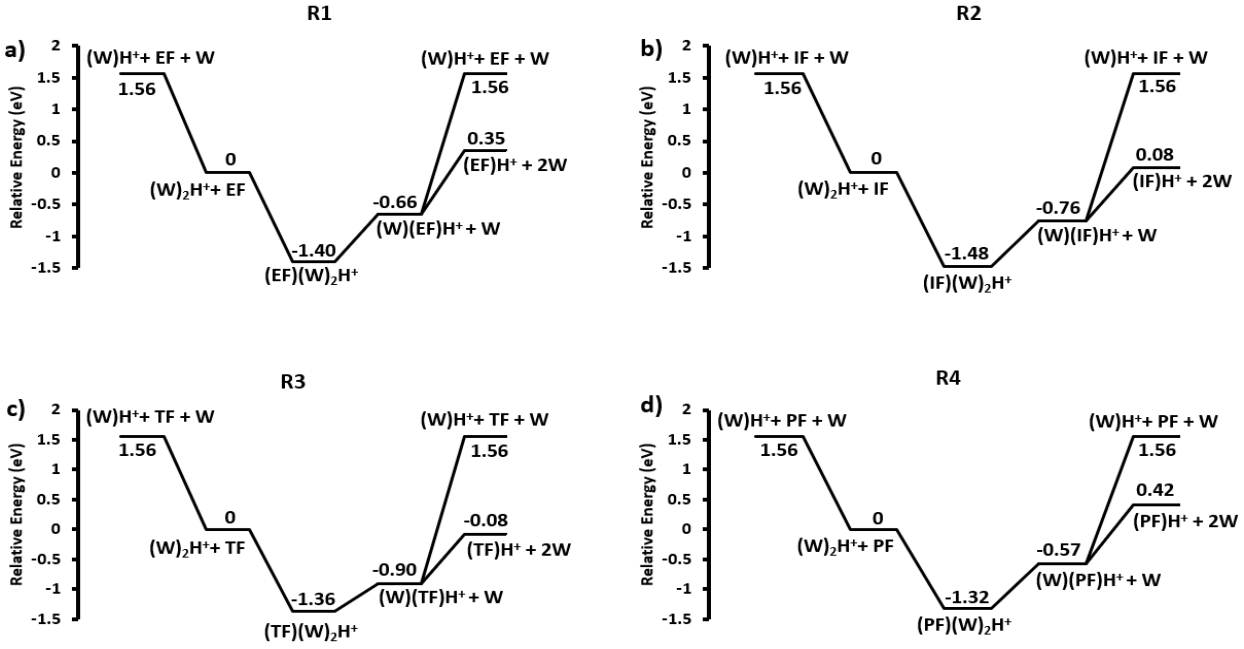

Figure 4.3: Relative energy (B3LYP/6-311+G(d,p)) of the main product ions from the interaction of the water dimer ion (m/z 37) with neutral a) EF (**R1**), b) IF (**R2**), c) TF (**R3**), d) and PF (**R4**).

The predicted dissociation energy for the $EF(W)_2H^+$ and $PF(W)_3H^+$ encounter complexes are 0.74 eV and 0.61 eV, respectively. The encounter complexes in a thermal system at 300 K exhibit an internal energy distribution that extend to 1.2 eV (*Figure 4.4a, c*), indicating that they would be stable species under atmospheric pressure. In the current experiment, however, the initial encounter complex is not seen because there is not enough time or pressure to collisionally stabilise the complex (*Figure 4.3* and *4.5*) with respect to water loss, which results in a high-rate constant for dissociation. For both ions (and indeed for all the ions studied here) the rate constant for water loss from the initially formed reactive complex at the internal energy with which they are formed are greater than 10^8 s^{-1} (*Figure 4b, d*). The greatest binding energy encounter complex, $PF(W)_2H^+$, has a 0.75 eV binding energy, as shown by the computational results reported in *Figure 4.3*, although this is still insufficient to enable their observation.

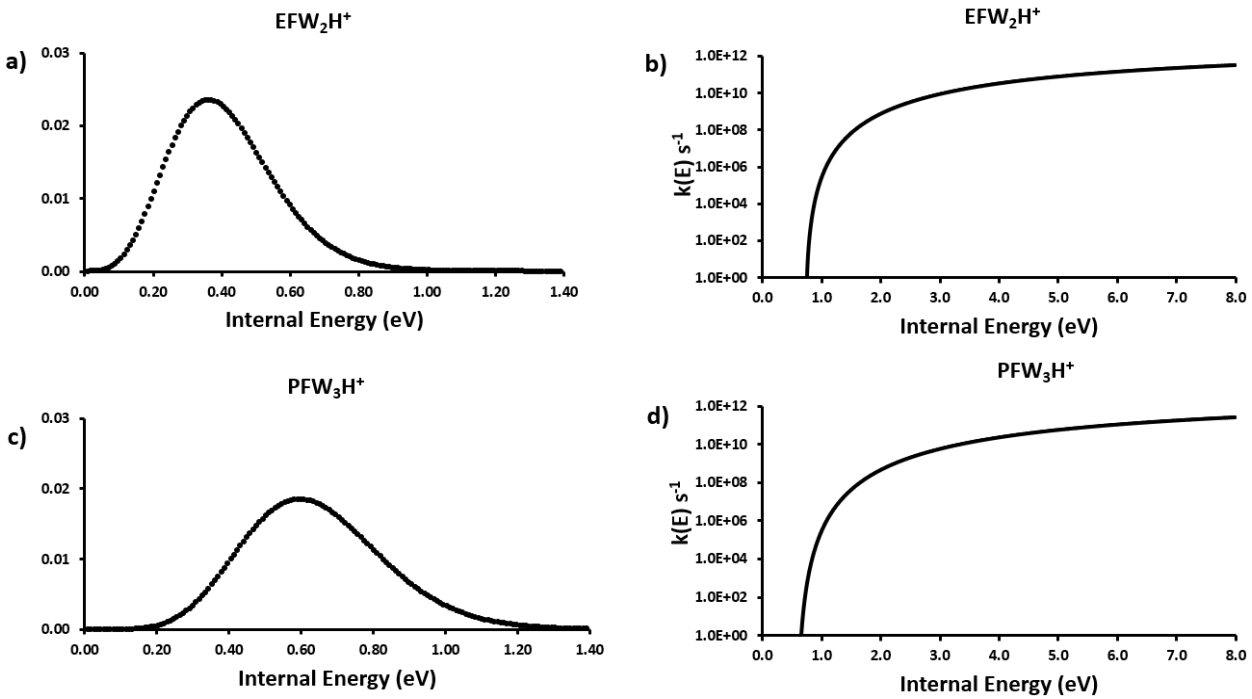

Figure 4.4: Vibrational internal energy distributions at 300 K for the encounter complexes in a) **R1** and c) **R8** and the RRKM k(E) vs E curves for the dissociation of the corresponding ion-molecule encounter complexes (b, d).

It appears that the primary reaction sequence once the encounter complex is formed is the successive loss of water, ultimately forming the protonated formate.

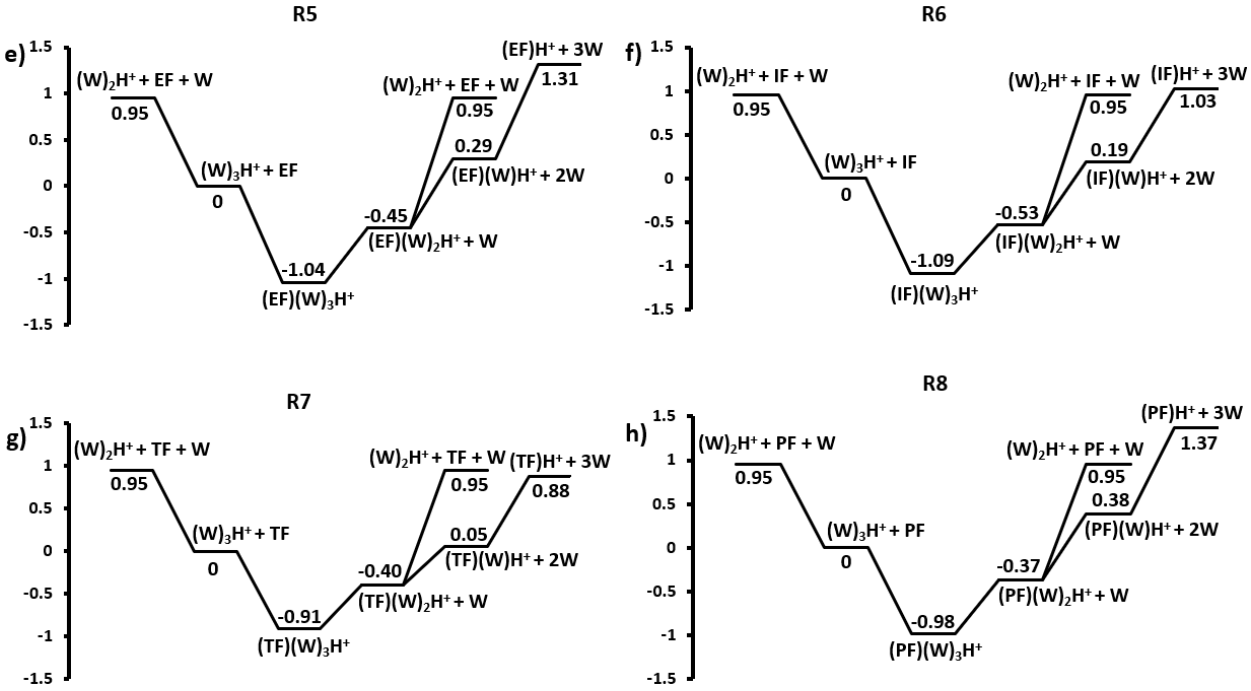

Figure 4.5: Relative energy (B3LYP/6-311+G(d,p)) of the main product ions from the interaction of water trimer ion (m/z 55) with neutral a) EF (**R5**), b) IF (**R6**), c) TF (**R7**), and d) PF (**R8**).

4.3.2. Unimolecular Reactions of Proton-Bound Water-Formate Clusters

The proton-bound complexes between EF, IF, TF and PF and a water molecule are the most prevalent principal reaction products observed in the ion-molecule reactions. The primary unimolecular reaction of these complexes is simple dissociation of a hydrogen bond as seen previously for reactions involving methyl formate.[97] In the electrospray source, we were able to independently produce $EF(W)H^+$, $IF(W)H^+$, $TF(W)H^+$, $PF(W)H^+$ and acquire CID breakdown curves for each complex (*Figure 4.6*). According to what was predicted based on the ion-molecule reaction outcomes in *Figures 4.1* and *4.2*, protonated ethyl, isopropyl, t-butyl and phenyl formate

are the common dissociation products, followed by their sequential dissociation as previously observed [83].

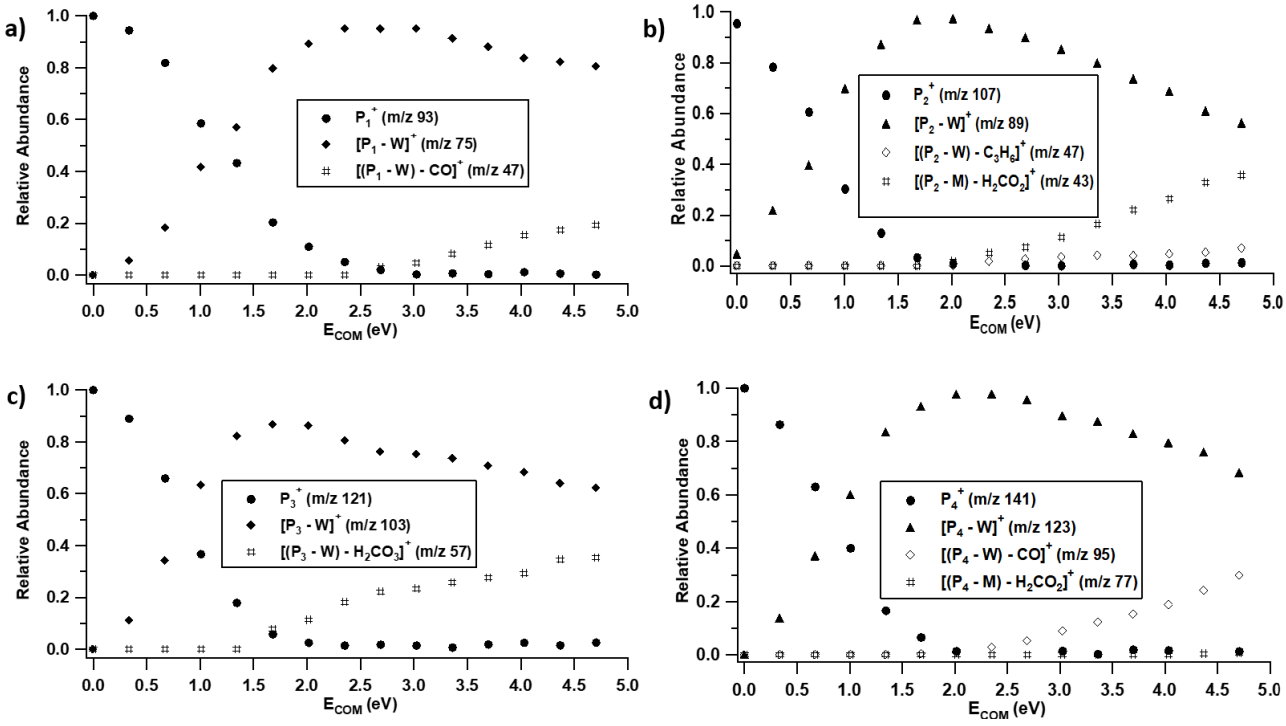

Figure 4.6: CID breakdown curves of a) P_1^+ = EF(W)H$^+$, b) P_2^+ = IF(W)H$^+$, c) P_3^+ = TF(W)H$^+$ and c) P_4^+ = PF(W)H$^+$.

EFH$^+$ is known to create the $CH_3CH_2OH_2^+$ (m/z 47) ion when CO is lost [83]. Similarly, the loss of CO from PFH$^+$, leads to the formation of $C_6H_7O^+$ (m/z 95). This fragmentation is followed by a sequential loss of H_2CO_2 to form $C_6H_5^+$ (m/z 77). In the case of IFH$^+$, parallel loss of C_3H_6 and H_2CO_2 is seen, which results in the formation of $H_3CO_2^+$ (m/z 47) and $C_3H_7^+$ (m/z 43), respectively [83]. The loss of H_2CO_2 from TFH$^+$ results in the $C_4H_9^+$(m/z 57) ion. The overall dominance of the loss of water from the formate-water complex is due to the much larger proton affinities (PA) of

EF, IF, TF and PF (799.4, 836.6, 841.1 and 793.1 kJ mol^{-1}, respectively) compared to that of water (691 kJ mol^{-1}) [84].

Simple hydrogen bond dissociation is the main initial unimolecular process of these complexes. The possibility of reverse activation barriers resulting from the potential structural rearrangement of these complexes was investigated using relaxed potential energy scans of the dissociation for $TF(W)H^+$, $IF(W)_2H^+$ and shown as examples in *Figure 4.7*. All the scans from the water monomer, dimer and trimer complexes clearly show that these encounter complexes may easily dissociate without a reverse barrier, which suggests that the relative product energies in *Figures 4.3* and *4.5* control the relative abundance of the competing reactions.

The initial dissociation pathways for the four proton-bound formate-water complexes were modeled with RRKM theory according to the semi-quantitative procedures outlined above. The results are summarized in *Figure 4.8*. The outcomes obtained using the model show that the RRKM predicted E_0 values (*Figure 4.8*) for the dissociation channels are significantly lower than those derived from the DFT calculations (*Figure 4.3*). This would suggest that the internal energy content of the formate-water complex is much higher than we have employed with this model in the past [82,84,99], leading to greater dissociation. One reason for this could be the inefficient vibrational energy transfer between these complexes and background gas in the source region of the instrument.

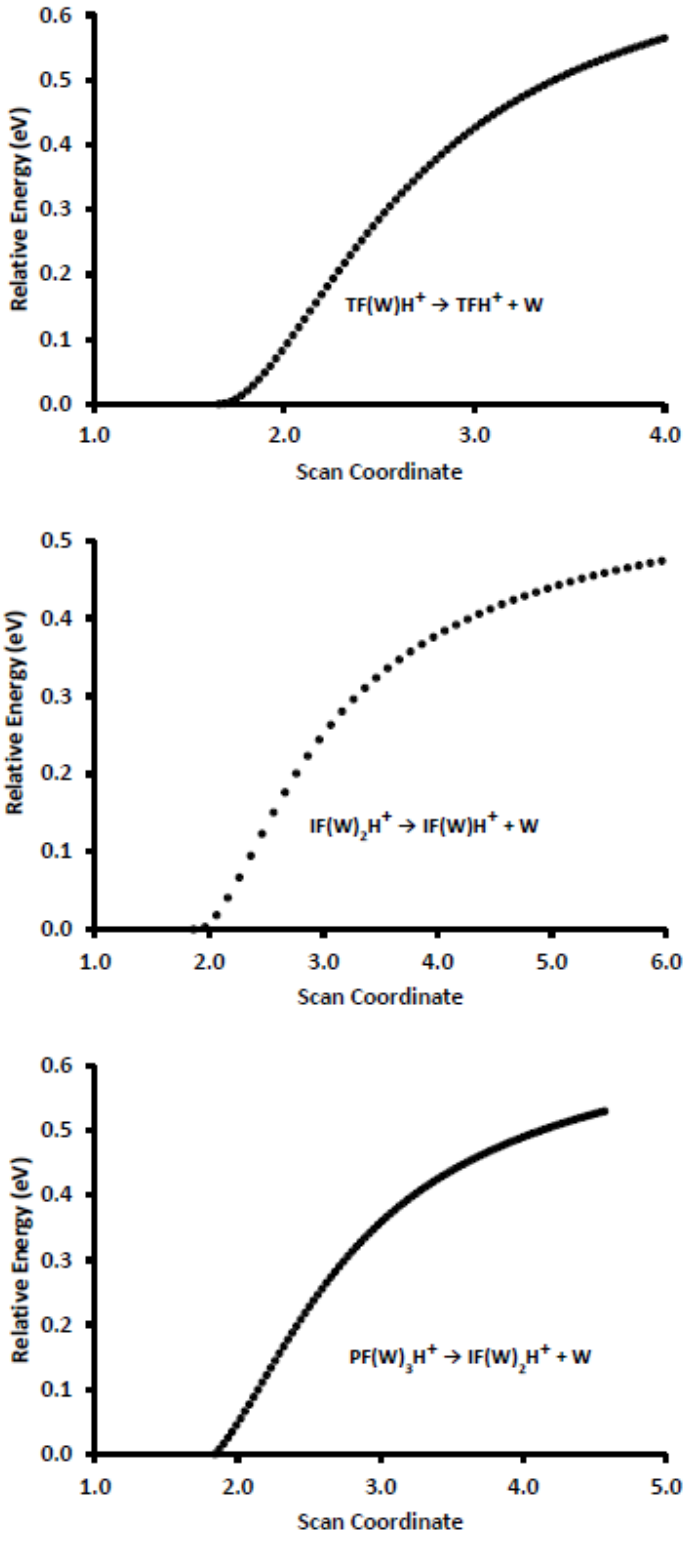

Figure 4.7: Relaxed potential energy scan of the dissociation of $TF(W)H^+$, $IF(W)_2H^+$ and $PF(W)_3H^+$ at the B3LYP/6-311+G(d,p) level of theory.

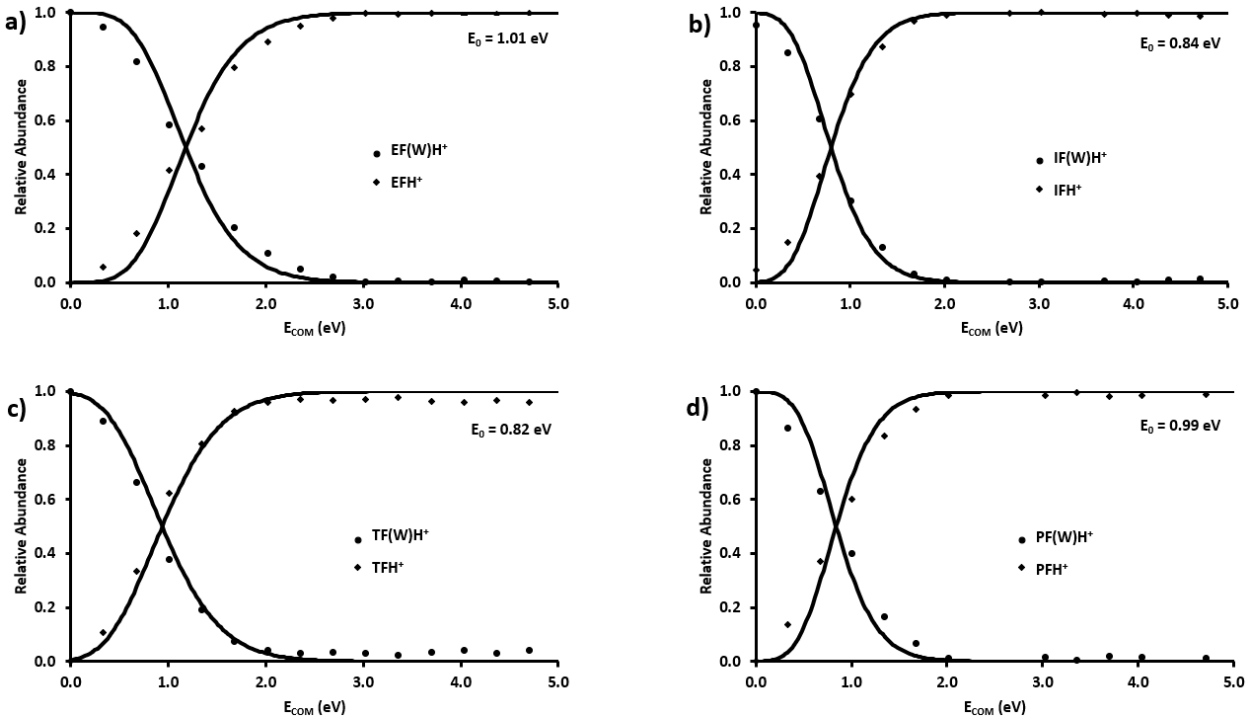

Figure 4.8: RRKM modeled breakdown curves for $EF(W)_2H^+$ $IF(W)_2H^+$, $TF(W)_2H^+$ or $PF(W)_2H^+$ complexes. Sequential fragmentation channels were summed into the primary channel to aid the modeling of those primary pathways. The solid line represents the RRKM fit.

4.4. Conclusions

Ion-molecule reactions between formates and proton-bound clusters of water demonstrate that the primary reaction product is the formation of the protonated formate due to its higher proton affinity. Loss of a water molecule from the encounter complex occurs without a reverse energy barrier in all cases. The results support the conclusion that when formates interact with atmospheric water, the encounter complexes, which were not observed in this experiment due to the low pressure in the reaction chamber, are stable to dissociation under equilibrium conditions. These encounter complexes can then go on to lose multiple water molecules leaving the protonated formate.

4.5. Appendix

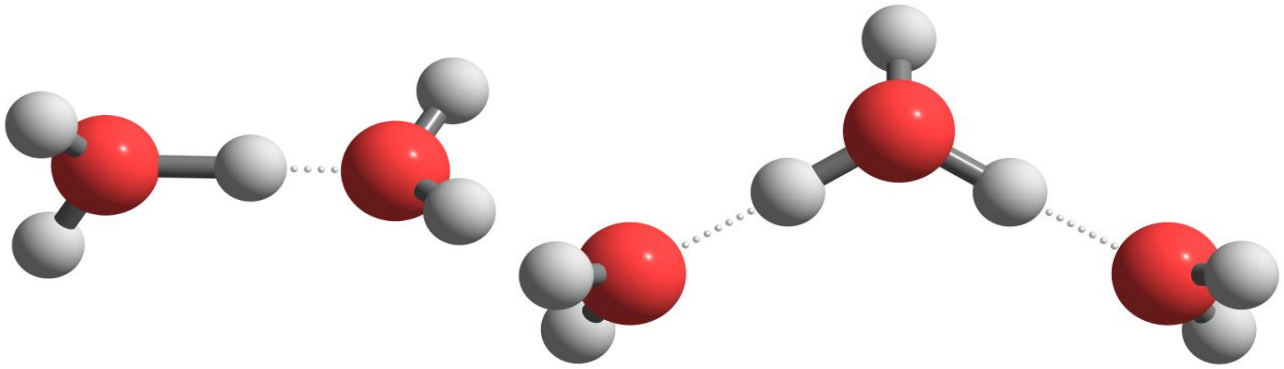

Figure S4.1: Calculated minimum energy structures for (W)2H+ and (W)3H+ at the B3LYP/6-311+G(d,p) level of theory.

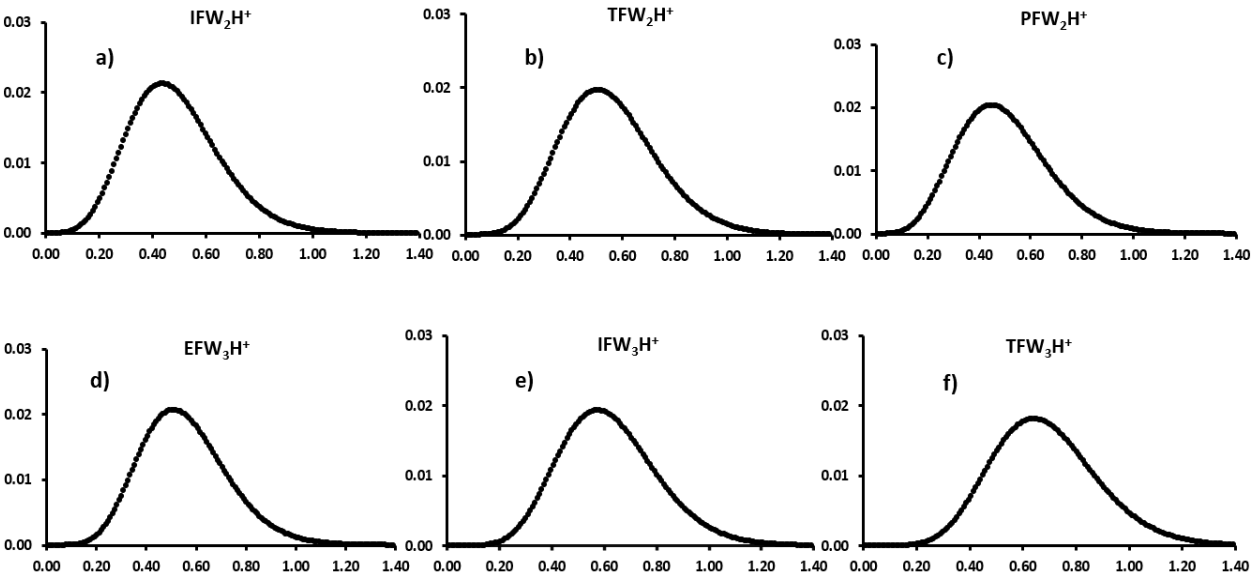

Figure S4.2: Vibrational internal energy distributions at 300 K for the encounter complexes.

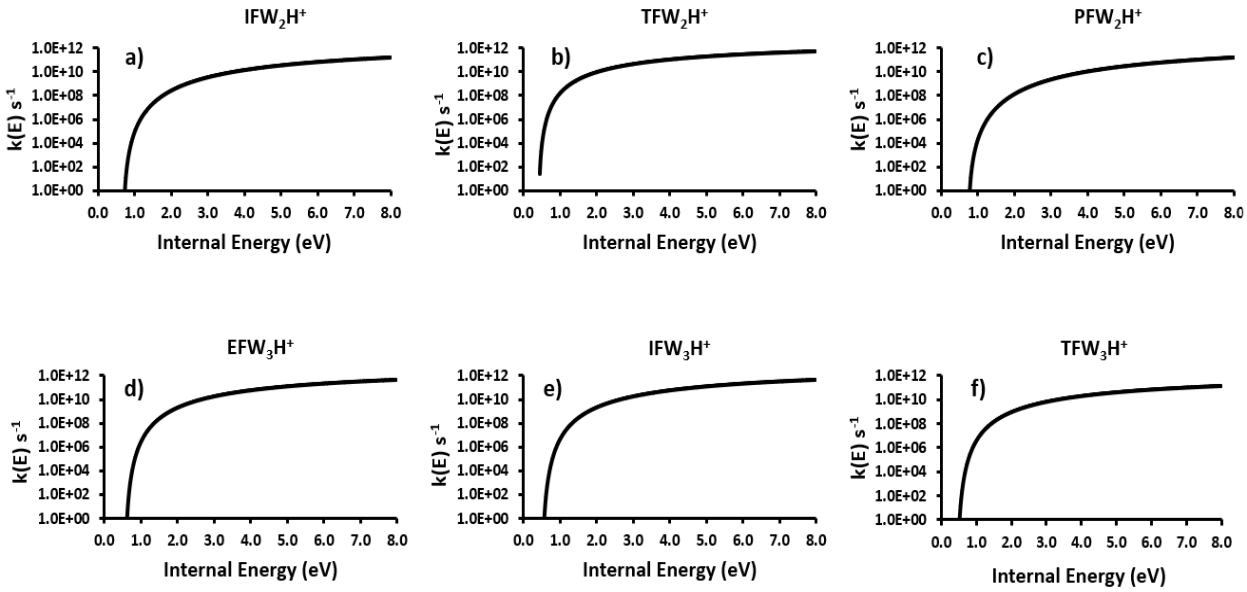

Figure S4.3: RRKM k(E) vs E curves for the dissociation of the ion-molecule encounter complexes.

Table 4.1: Theoretical Energies calculated from *Figure 4.3*.

Reaction	Theoretical E_0 (eV)
$EF(W)_2H^+ \rightarrow EF(W)H^+ + W$	0.74
$\rightarrow EFH^+ + 2W$	1.01
$\rightarrow WH^+ + W + EF$	2.22
$EF(W)_3H^+ \rightarrow EF(W)_2H^+ + W$	0.59
$\rightarrow EF(W)H^+ + 2W$	0.74
$\rightarrow (W)_2H^+ + W + EF$	1.40
$\rightarrow EFH^+ + 3W$	1.02
$IF(W)_2H^+ \rightarrow IF(W)H^+ + W$	0.72
$\rightarrow IFH^+ + 2W$	0.84
$\rightarrow WH^+ + W + IF$	2.32
$IF(W)_3H^+ \rightarrow IF(W)_2H^+ + W$	0.56
$\rightarrow IF(W)H^+ + 2W$	0.75
$\rightarrow (W)_2H^+ + W + IF$	1.48
$\rightarrow IFH^+ + 3W$	0.84
$TF(W)_2H^+ \rightarrow TF(W)H^+ + W$	0.46
$\rightarrow TFH^+ + 2W$	0.82
$\rightarrow WH^+ + W + TF$	2.46
$TF(W)_3H^+ \rightarrow TF(W)_2H^+ + W$	0.51
$\rightarrow TF(W)H^+ + 2W$	0.45
$\rightarrow (W)_2H^+ + W + TF$	1.35
$\rightarrow TFH^+ + 3W$	0.83
$PF(W)_2H^+ \rightarrow PF(W)H^+ + W$	0.75
$\rightarrow PFH^+ + 2W$	0.99
$\rightarrow WH^+ + W + PF$	2.13
$PF(W)_3H^+ \rightarrow PF(W)_2H^+ + W$	0.61
$\rightarrow PF(W)H^+ + 2W$	0.75
$\rightarrow (W)_2H^+ + W + PF$	1.32
$\rightarrow PFH^+ + 3W$	0.99

CHAPTER 5. THE FATE OF PROTONATED FORMATES IN THE GAS PHASE

Published as Diedhiou, Malick and Mayer, Paul M. (2021). The Fate of Protonated Formates in the Gas Phase. J. Phys. Chem. A, 125, 5096-5102. doi:10.1021/acs.jpca.1c03814.

5.1. Introduction

The atmospheric fate of organic acids has not been as extensively studied as that of their inorganic cousins [100-103]. Organic acids have both anthropogenic and biogenic sources and are linked to global climate change [104]. A 1989 study aimed to measure the atmospheric levels of organic acids and determine the sources and sinks of formates, formic acid, and acetic acid [100,105]. The major contributor to their atmospheric levels was determined to be emissions from mobile sources (vehicular fuel combustion). Carboxylic acids are known to play important roles in atmospheric chemistry including reactions with hydroxyl radicals [106]. Proton transfer reactions between hydroxyl radicals and formic acid, the most abundant carboxylic acid in the troposphere, can lead to the production of formates [107]. The importance of acid-derived formates and esters in atmospheric chemistry cannot be understated. After being emitted from fuel additives and industrial solvents, these species can undergo a vast range of chemical reactions in the atmosphere, most of which are initiated by oxidation by hydroxyl radicals [108,109]. Formate concentrations in non-urban precipitation were reported to be 10 to 30 μM [100,110,111]. Khare et al. demonstrated that wet and dry deposition are both considered to be the main atmospheric sinks for formates/formic acid (95%) [24]. Formates are also present in cloud water, fog, and dew (3.2 to 627 μM) [24]. The proposed secondary sources of formates/formic acid (atmospheric

chemical production) include isoprene photooxidation, aldehyde oxidation by HO_2 radicals, ozone-olefin reactions, and gas/aqueous phase oxidation of formaldehyde by hydroxy radicals [112,113]. Anthropogenic emissions contributing to formic acid and formate levels include biomass burning and automobile exhaust (incomplete combustion and fuel additives) [114-116]. Biogenic and other natural sources include direct emission from vegetation, release from soil, and formicine ants [117,118].

Understanding the atmospheric fate of formates, including their interactions with water clusters have become recent interests in atmospheric chemistry research [119]. The complexity of the oxidation reaction pathways of formates shows how starting with a few simple species in the atmosphere can lead to the propagation and production of a plethora of radicals and products [96]. In 2018, Wu et al. aimed to use computational methods, including statistical rate theory to study the temperature and pressure dependence of the methyl formate + OH reaction across a broad range of conditions [94]. The reaction between a formate and a proton source such as water can lead to proton transfer, which results in the formation of the protonated formate [120]. The reaction can take place in presence of any proton source such as HCO^+ or $C_2H_5OH^+$. A question that arises is thus of the chemistry of these now very reactive protonated formates. Herein, we use a combination of tandem mass spectrometry and computational chemistry to study the unimolecular reactions of protonated methyl-, ethyl-, isopropyl-, t-butyl-, and phenyl- formate.

5.2. Experimental Procedures

Methyl, ethyl, isopropyl, t-butyl, and phenyl formates were purchased from Sigma Aldrich (Sigma-Aldrich, Oakville, Ontario, CA) and used without further purification.

5.2.1. Tandem Mass Spectrometry

Solutions (100μg/ml) in methanol were introduced to the electrospray source (having z-spray optics) of a Micromass Ultima triple-quadrupole mass spectrometer by syringe pump with a flow rate of 50ml min^{-1}. Protonated formate ions are selected according to their m/z ratio by the first quadrupole and passed into the collision cell of the instrument where they undergo collisions with argon target gas. The product ions are analyzed by the second quadrupole analyzer. A breakdown diagram is obtained by acquiring collision-induced dissociation (CID) mass spectra as a function of collision energy and plotting the relative abundance of the precursor and product ions as a function of the same. To compare the breakdown of different ions, the laboratory-frame collision energy (E_{LAB}) is first converted to centre-of-mass frame (E_{COM}) to account for the different efficiencies of collisional-energy transfer, according to equation (5.1):

$$E_{COM} = E_{LAB}\left(\frac{m_{Ar}}{m_{Ar}+m_I}\right) \qquad \textbf{(5.1)}$$

where m_{Ar} is the mass of an argon atom and m_I is the mass of the ion.

5.2.2. Computational Methods

All calculations (optimizations and vibrational frequency calculations) were performed with the GAUSSIAN 16 suite of programs [51] at the B3LYP level using the 6-311+G(d,p) basis set [77,78]. Single-point calculations with the CBS-QB3 composite method [121,122] were used to refine the energy obtained from the B3LYP level of theory. Intrinsic reaction coordinate calculations were employed to confirm transition states. *Figure 5.1* contains the lowest-energy optimized structures for the protonated formates.

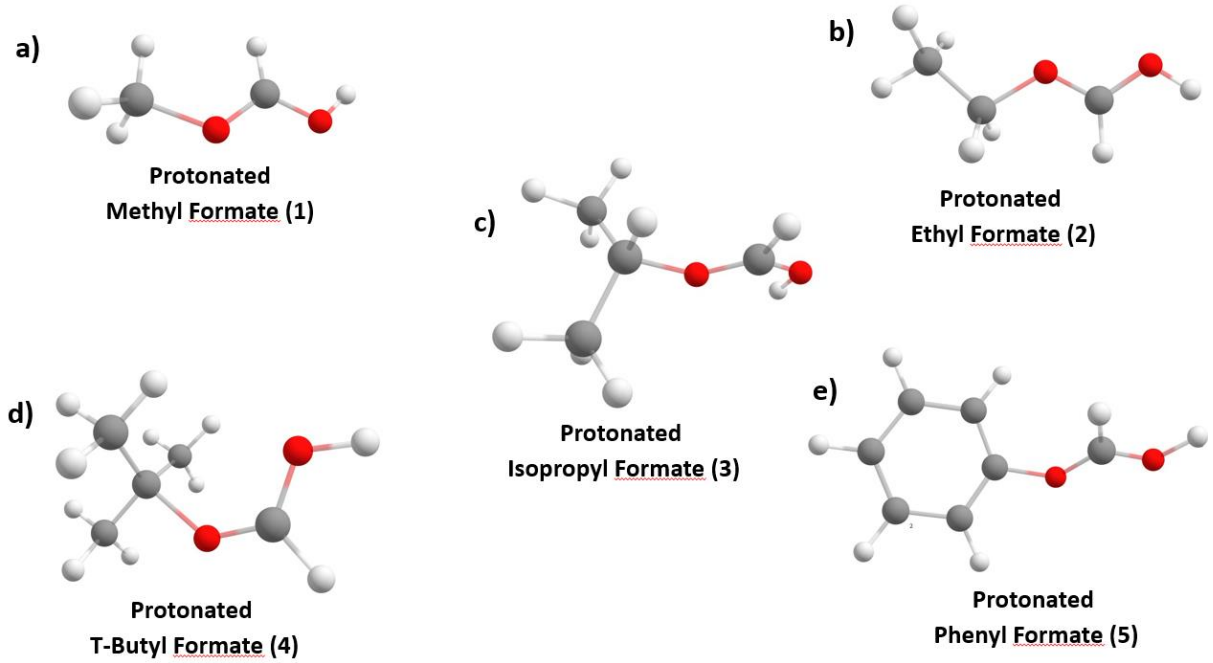

Figure 5.1: Global minimum calculated protonated formates at the B3LYP/6-311+G(d,p) level of theory.

5.3. Results and Discussion

5.3.1. Tandem Mass Spectrometry

Representative CID mass spectra for each protonated formate are shown in *Figure 5.2* and the resulting breakdown curves in *Figure 5.3*.

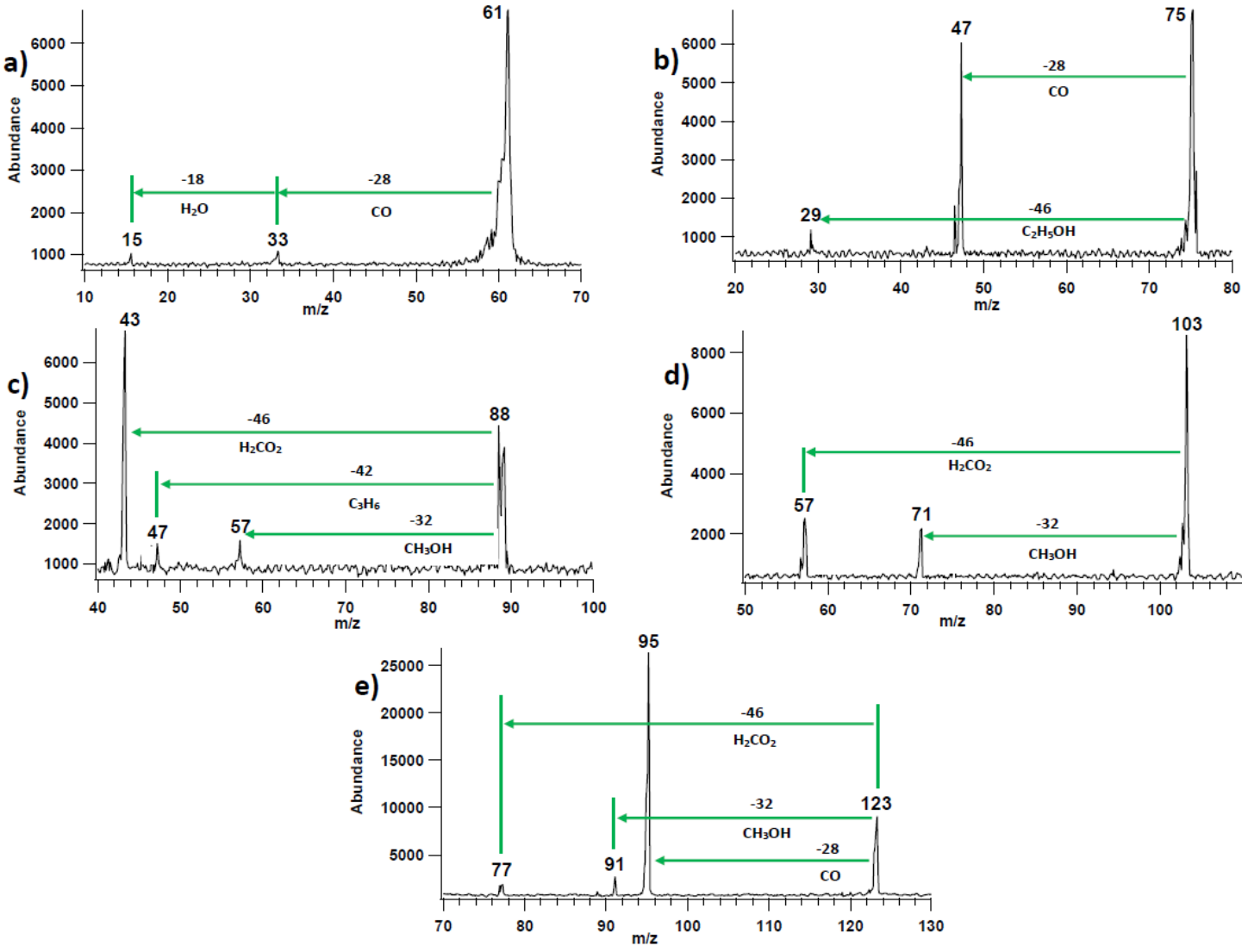

Figure 5.2: Representative CID mass spectra (each at the given E_{LAB}) of protonated **a)** methyl formate (**1**, m/z 61, 25 eV), **b)** ethyl formate (**2,** m/z 75, 10 eV), **c)** isopropyl formate (**3**, m/z 88, 13 eV), **d)** t-butyl formate (**4**, m/z 103, 10 eV) and **e)** phenyl formate (**5**, m/z 123, 10 eV).

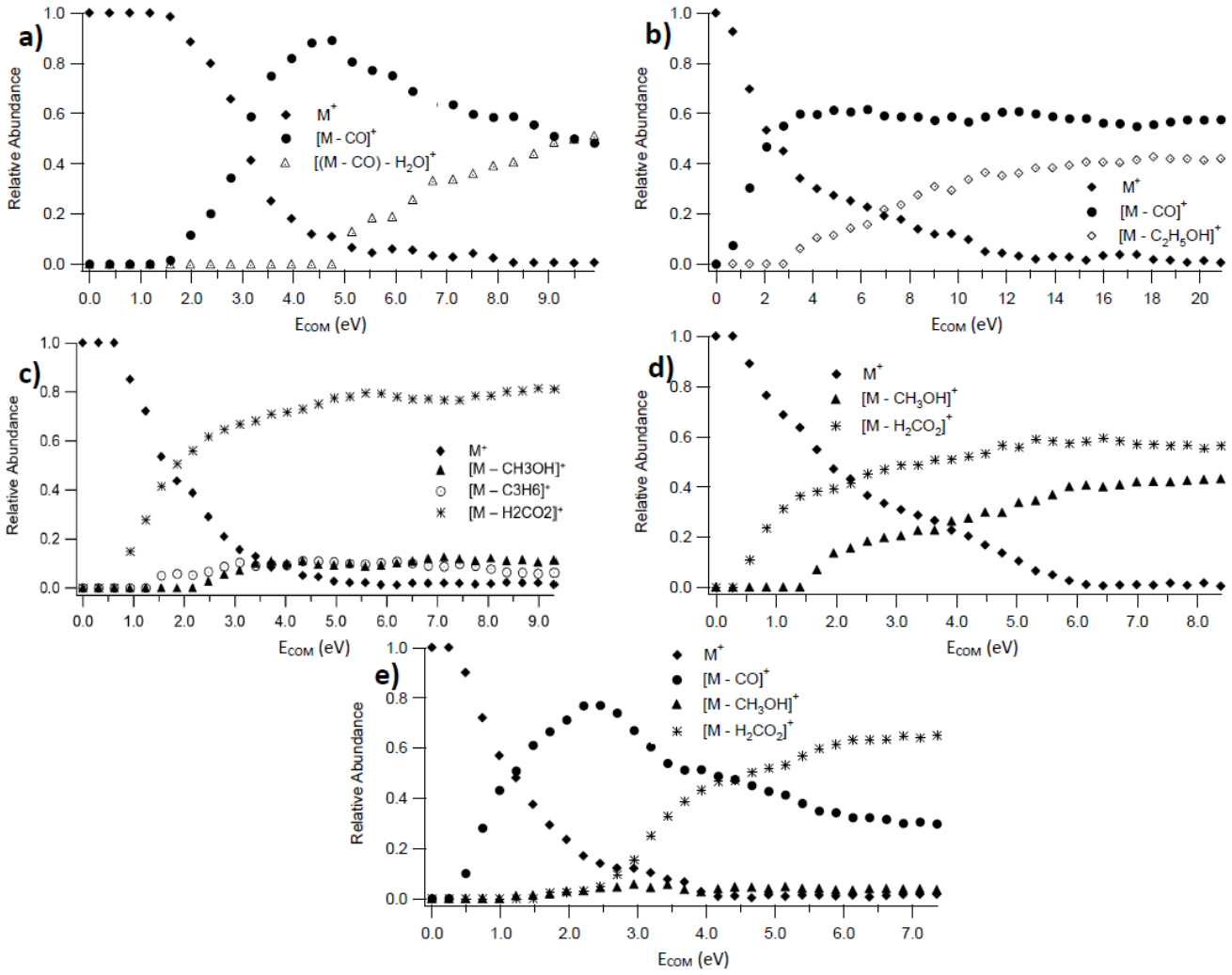

Figure 5.3: CID breakdown curves of protonated **a)** methyl formate (**1**), **b)** ethyl formate (**2**), **c)** isopropyl formate (**3**), **d)** tert-butyl formate (**4**), and **e)** phenyl formate (**5**).

There are two reactions (R1 and R2) for the unimolecular dissociation of the protonated methyl formate (**1**), sequential loss of CO (R1) and H_2O to form CH_3^+ (R2) as shown in *Figure 5.2a*.

$C_2H_5O_2^+ \rightarrow CH_5O^+$ (m/z 33) + CO (R1)

$CH_5O^+ \rightarrow CH_3^+$ (m/z 15) + H_2O (R2)

Fragmentation of protonated ethyl formate (**2**) leads to competing losses of CO (R3) and C_2H_5OH (R4), with the former occurring at very low collision energy. The two reactions are complimentary suggesting a common intermediate (such as a proton-bound complex of CO and ethanol) that can dissociate to either set of products, with loss of CO being energetically more favorable since ethanol has the greater proton affinity (PA, 776.4 vs 594 kJ mol^{-1}) [123].

$C_3H_7O_2^+ \rightarrow C_2H_7O^+(m/z\ 47) + CO$ (R3)

$C_3H_7O_2^+ \rightarrow CHO^+(m/z\ 29) + C_2H_5OH$ (R4)

Protonated isopropyl formate (**3**) dissociates three ways: loss of CH_3OH (R5), C_3H_6 (R6), and formic acid, H_2CO_2 (R7). Absent is CO loss. Reactions R6 and R7 are complimentary, again suggesting the participation of a common reaction intermediate of a proton-bound complex between formic acid and propene. The PA of formic acid is 742 kJ mol^{-1} compared to 752 kJ mol^{-1} for propene, [123] and so there is a favoring of losing the neutral formic acid as evident in the breakdown diagram in *Figure 3*.

$C_4H_9O_2^+ \rightarrow C_3H_5O^+(m/z\ 57) + CH_3OH$ (R5)

$C_4H_9O_2^+ \rightarrow H_3CO_2^+(m/z\ 47) + C_3H_6$ (R6)

$C_4H_9O_2^+ \rightarrow C_3H_7^+(m/z\ 43) + H_2CO_2$ (R7)

Protonated t-butyl formate (**4**) displays the same behavior as protonated isopropyl formate in the loss of CH_3OH (R8) and H_2CO_2 (R9), suggesting analogous reaction pathways. The stability of the $C_4H_9^+$ ion likely prevents the competing loss of C_4H_8 forming protonated formic acid. Indeed, the PA of isobutene is 802 kJ mol^{-1}, some 60 kJ mol^{-1} higher than that of formic acid, precluding the formation of the protonated acid.

$C_5H_{11}O_2^+ \rightarrow C_4H_7O^+(m/z\ 71) + CH_3OH$ (R8)

$C_5H_{11}O_2^+ \rightarrow C_4H_9^+(m/z\ 57) + H_2CO_2$ (R9)

Protonated phenyl formate (**5**) exhibits reactions from both sets of ions above. It loses CO (R10), CH_3OH (R11), and H_2CO_2 (R12).

$C_7H_7O_2^+ \rightarrow C_6H_7O^+(m/z\ 95) + CO$ (R10)

$C_7H_7O_2^+ \rightarrow C_6H_3O^+(m/z\ 91) + CH_3OH$ (R11)

$C_7H_7O_2^+ \rightarrow C_6H_5^+(m/z\ 77) + H_2CO_2$ (R12)

5.3.2. Calculated Reaction Mechanisms

There are two sequential channels in the dissociation of **1**, leading to the loss of CO followed by the loss of H_2O. The loss of CO occurs by a series of hydrogen migrations, initiated by the transfer of the proton from the carbonyl group to the ester oxygen, having an energy requirement of 1.82 eV. This is followed by the formation of a proton-bound complex between methanol and CO (0.09 eV) which then loses CO (0.53 eV) due to the higher proton affinity of methanol (754.3 kJ mol^{-1}) compared to CO (594 kJ mol^{-1}) [124]. The loss of H_2O is a sequential channel from the dissociation of protonated methanol (*Figure 5.4*).

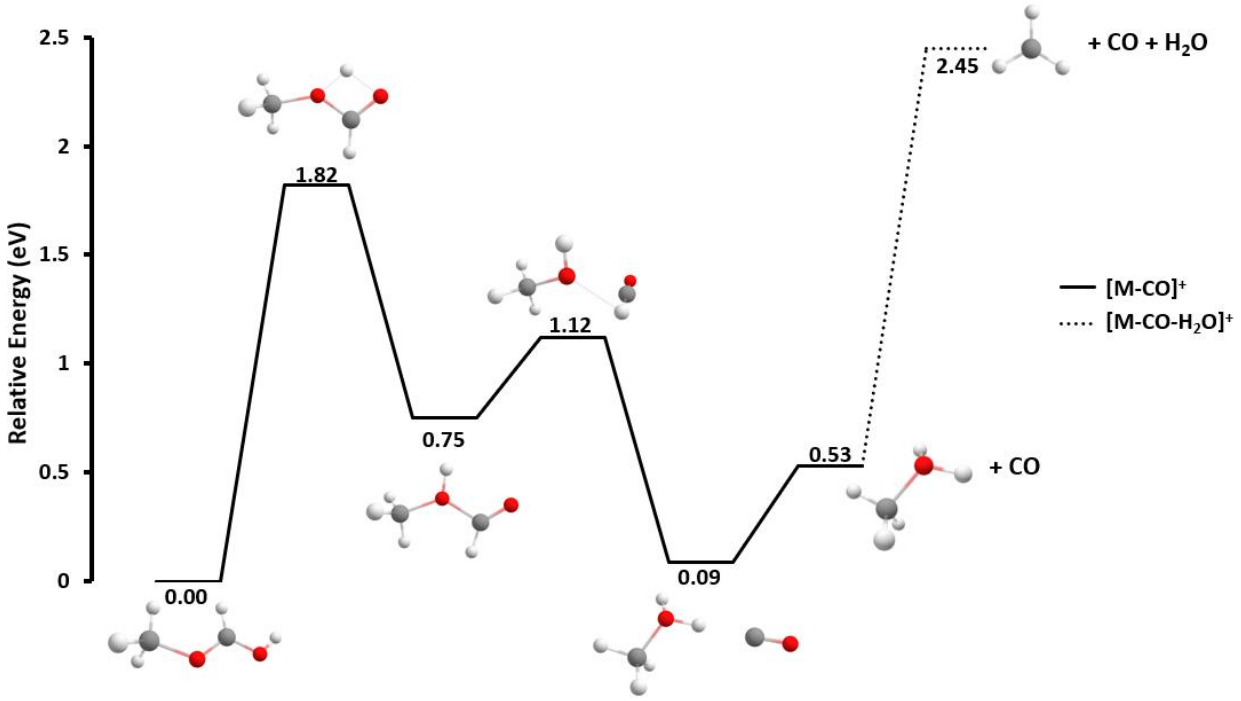

Figure 5.4: CBS-QB3//B3LYP/6-311+G(d,p) minimum energy reaction pathways for CO loss (—) and CO,H_2O loss (····) and from **1**.

The two competing channels for **2** (*Figure 5.5*) are initiated by an analogous 1,3-H shift (1.76 eV) to form the protonated ester oxygen atom (0.69 eV), as seen for **1**. This ion can either lose ethanol via a high energy bond cleavage reaction (2.29 eV) or isomerize into a proton-bound complex of ethanol and CO, which preferentially goes on to lose the CO molecule (0.45 eV).

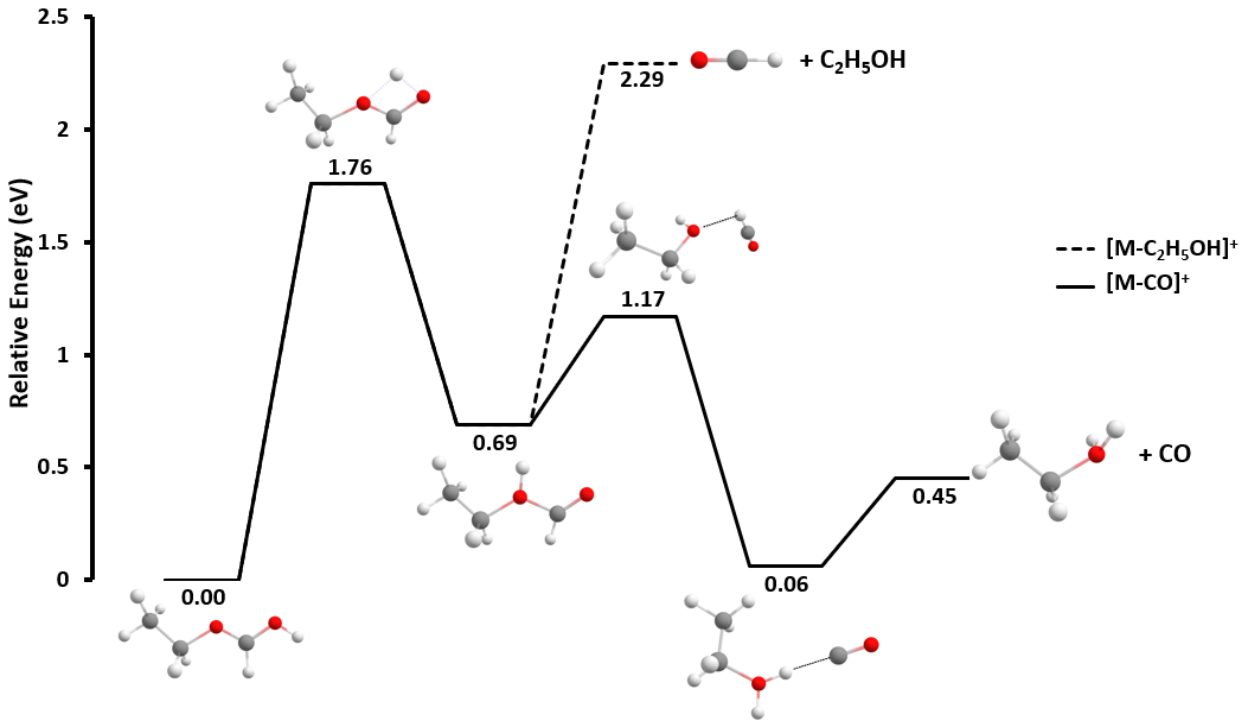

Figure 5.5: CBS-QB3//B3LYP/6-311+G(d,p) minimum energy reaction pathway for C_2H_5OH loss (---) and CO loss (—) from **2**.

The dissociation of **3** leads to the loss of H_2CO_2, C_3H_6, and CH_3OH (*Figure 5.6*). H_2CO_2 loss can occur directly from the protonated isopropyl formate with an energy requirement of 1.20 eV. As for the loss of C_3H_6, **3** undergoes rearrangement (transition state not found) to make a proton-bound complex between propene and H_2CO_2 (0.67 eV). The similarity of the PA of propene and formic acid means there are two forms of this ion (0.67 and 0.62 eV) that can interconvert over a barrier of 0.1 – 0.15 eV. This complex can also lose H_2CO_2 to form the propyl cation (1.20 eV) or C_3H_6 (1.35 eV). Similarly, loss of CH_3OH starts by a rearrangement of **3** to a complex between propene and the OH oxygen atom of formic acid (1.06 eV) and then to a complex between the ethyl acylium ion and methanol via a transition state at 1.41 eV, which then loses

CH_3OH (1.17 eV). For this latter pathway we may not have found every intermediate, but believe the key steps are those in the *Figure5.6*.

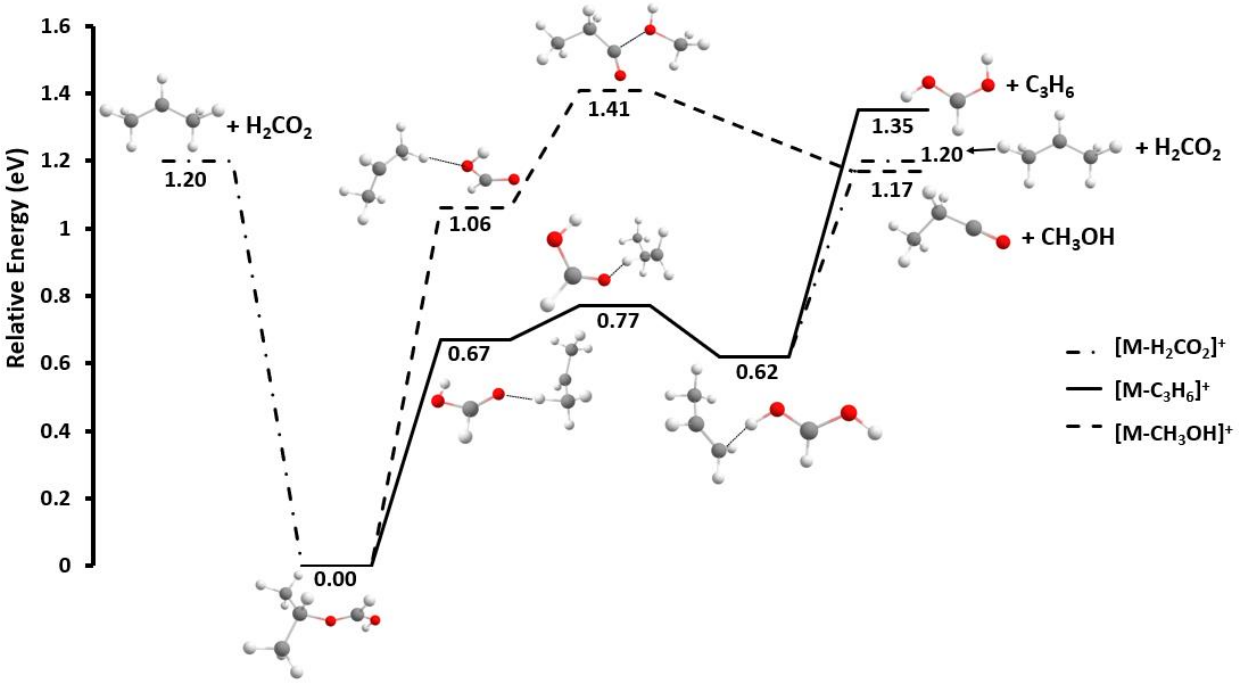

Figure 5.6: CBS-QB3//B3LYP/6-311+G(d,p) minimum energy reaction pathways for H_2CO_2 loss (- · -), C_3H_6 loss (---) and CH_3OH loss (—) from **3**.

The minimum energy reaction pathways of **4** are shown in *Figure 5.7*. The loss of H_2CO_2 is a direct cleavage of the ion requiring only 0.67 eV, consistent with the appearance of this product ion at low collision energy (*Figure 5.3d*). **4** can also isomerize to form a complex between the isopropyl acylium ion and methanol (0.55 eV) prior to the loss of the latter neutral molecule (1.17 eV). Again, we likely did not find all of the structures in this pathway, but believe the key intermediates are as shown in the *Figure 5.7*.

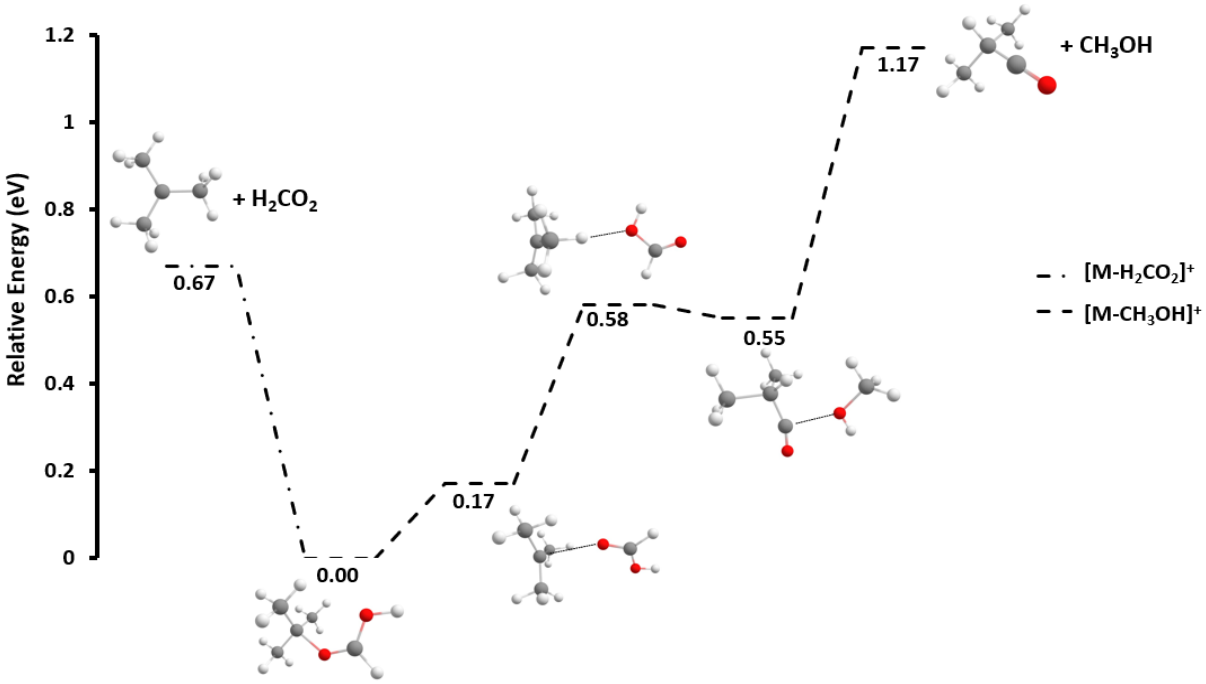

Figure 5.7: CBS-QB3//B3LYP/6-311+G(d,p) minimum energy reaction pathways for H_2CO_2 loss (-・-) and CH_3OH loss (---) from **4**.

In the case of **5**, **t**he loss of methanol (R11) is a very minor reaction (*Figure 5.3e*) likely involving a similar set of ion-molecule complexes as seen for **3** and **4**, and so was not calculated herein. As noticed in the behavior of the alkyl formates, the loss of H_2CO_2 occurs directly from the protonated phenyl formate (2.26 eV), *Figure 5.8*. The loss of CO can follow two distinct pathways depending on whether the final product ion, protonated phenol, is protonated on O or C. Both paths are initiated by proton-transfer to the ester oxygen atom (1.82 eV) to form a common reaction intermediate (0.63 eV). This ion can either hydrogen transfer to a carbon atom on the ring or to the oxygen, forming in both cases complexes between a protonated phenol and CO, which then lose CO. Protonating the phenol on the benzene ring is 0.51 eV (49 kJ mol^{-1}) more favorable than on oxygen and involves a slightly lower barrier (0.80 vs 1.02 eV). The similarity of these two

barriers suggests that a mixture of product ions will be made, especially since the system has enough internal energy to overcome the initial 1.82 eV barrier.

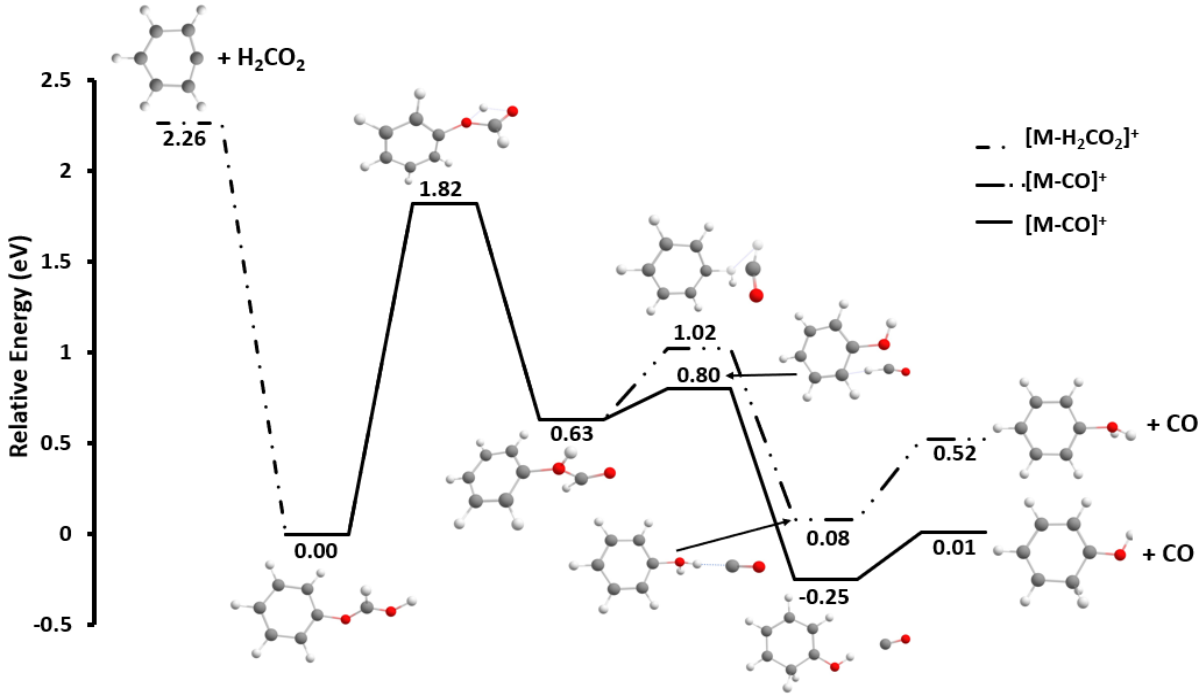

Figure 5.8: CBS-QB3//B3LYP/6-311+G(d,p) minimum energy reaction pathways for H_2CO_2 loss (- · -), and two possible paths to CO loss (— · · —) and (—) from **5**.

5.4. Conclusions

The unimolecular reactions of protonated formates were explored with tandem mass spectrometry and computational chemistry. For protonated methyl-, ethyl-, and phenyl formate, a common reaction involves the isomerization of the global minimum structure to one with a protonated ester oxygen. This isomer then leads to ion-molecule complexes between protonated alcohols and CO and ultimately CO loss. As the stability of the R group in ROC(O)H increases, direct loss of formic acid becomes the dominant pathway, in competition with methanol loss, which appears to be mediated in each case by a series of ion-molecule complexes.

CHAPTER 6. ON THE FATE OF PROTONATED CHLOROFORMATES IN THE GAS PHASE: A COMPETITION BETWEEN FORMING HCl AND CHLOROFORMIC ACID

Published as Diedhiou, Malick & Mayer, Paul M. (2024). On The Fate of Protonated Chloroformates in the Gas Phase: A Competition Betthen Forming HCl and Chloroformic Acid. J. Mass Spectrom. 2024 Jun; 59(6): e5044. doi: 10.1002/jms.5044.

6.1. Introduction

The atmospheric chemistry of organic acids, both in their pure form and as part of complex chemical reactions, has garnered significant attention due to its implications for global climate change and air quality [125-127]. While many studies have explored the fate of organic acids and their interactions with various atmospheric components, the focus has often been on common carboxylic acids like formic acid and acetic acid [68,107,114,128-130]. However, there is a growing interest in understanding the behavior, reactivity, and dissociation of less-studied compounds, such as chloroformates in the Earth's atmosphere.

Chloroformates are a class of atmospheric species [131] formed by reactions of chloroformic acid and can be protonated through interactions with HCO^+ (hydrocarbonyl cation), $C_2H_5OH_2^+$ (protonated ethanol) or protonated water clusters [132]. The primary sources of chloroformates are associated with industrial processes and vehicle emissions. For instance, methyl chloroformate

and phenyl chloroformate are used in the chemical industry as pharmacological agents, in pesticide manufacturing and can be released directly into the atmosphere [133-135]. There are also natural processes that contribute to their presence in the atmosphere [136,137]. The resulting protonated chloroformates are potentially highly reactive. The specific reactions can include but are not limited to, atmospheric degradation pathways, formation of secondary organic aerosols, and interactions with other atmospheric constituents [138-140].

In this study, we use a combination of tandem mass spectrometry and computational chemistry to elucidate the chemistry of protonated methyl, ethyl, neopentyl, and phenyl chloroformate. In our previous work on alkyl formates, we explored their interaction with protonated water and alcohol clusters and the unimolecular dissociation of protonated formates formed by electrospray ionization [141]. Chloroformates have proven to be more difficult to study. When we employed electrospray ionization, we did not observe a mass spectral signal for the protonated chloroformates. In addition, a look at the NIST mass spectral database shows that only methyl and phenyl chloroformate have a significant molecular ion signal in their electron ionization (EI) mass spectra. Our attempts to study these molecules using imaging photoelectron photoion coincidence spectroscopy at the Swiss Light Source resulted only in the photoionization of degradation products of the chloroformates, other than methyl chloroformate and phenyl chloroformate [137,142]. In the present contribution, we successfully generated the protonated chloroformates by chemical ionization of the corresponding neutrals in the EI source of a double focussing magnetic sector mass spectrometer. The short time scale for introducing the neutral vapour into the source permits some of the intact neutral to be protonated by ion-molecule reaction

with the chemical ionization reagent, methanol. Of note is that isopropyl chloroformate remained elusive and could not be studied.

6.2. Experimental Procedures

Methyl-, ethyl-, neopentyl-, and phenyl-chloroformate were purchased from Sigma Aldrich (Sigma-Aldrich, Oakville, Ontario, CA) and used without further purification.

6.2.1. Tandem Mass Spectrometry

The mass spectrometer employed was a modified VG ZAB-R double focusing mass spectrometer of BEE geometry (a magnetic sector followed by two electrostatic analyzers, of which only the first was used in these experiments) [143]. Approximately 10 mL of liquid sample is introduced using a gas chromatography syringe through a septum inlet into a steel reservoir heated to 100^{o}C. The resulting vapour is transferred to the ion source via a glass capillary inlet heated to 110^{o}C. The source pressure, read with an ionization gauge at the top of the turbo pump under the ion source, was typically 5 x 10^{-6} mbar, with the pressure in the source itself being at least 100 times larger. Methanol was then introduced in the same manner to increase the pressure reading to 10^{-4} mbar. Within the ion source, the methanol preferentially undergoes electron ionization (due to its much higher abundance) and subsequent ion-molecule reactions resulted in mass spectral signals for the two isotopes of each protonated chloroformate. The generated ions are then accelerated to 8 keV and directed to the magnetic sector, where the ions are selected based on their mass-to-charge ratio [41]. The selected ions proceed to the second field-free region (FFR) where metastable ions dissociate (those ions leaving the source with sufficient internal energy to dissociate with rate constants between 10^{3} and 10^{6} s^{-1}) [44]. The product ions from dissociation

events in the FFR have translational energies that are related to that of the precursor ion by their relative mass. These are separated by the electrostatic analyzer (ESA) to yield a mass-analyzed ion kinetic energy, or MIKE, spectrum [42,41].

6.2.2. Computational Methods

The GAUSSIAN 16 suite of programs [51] was used to perform all calculations (optimizations and vibrational frequency calculations) at the B3LYP level of theory using the 6-311+G(d,p) basis set [77,78]. Intrinsic reaction coordinate calculations were employed to confirm transition states. CBS-QB3 [121] single point energy calculations were employed to obtain accurate energetics. *Figure 6.1* shows the lowest-energy optimized structures for the protonated chloroformates.

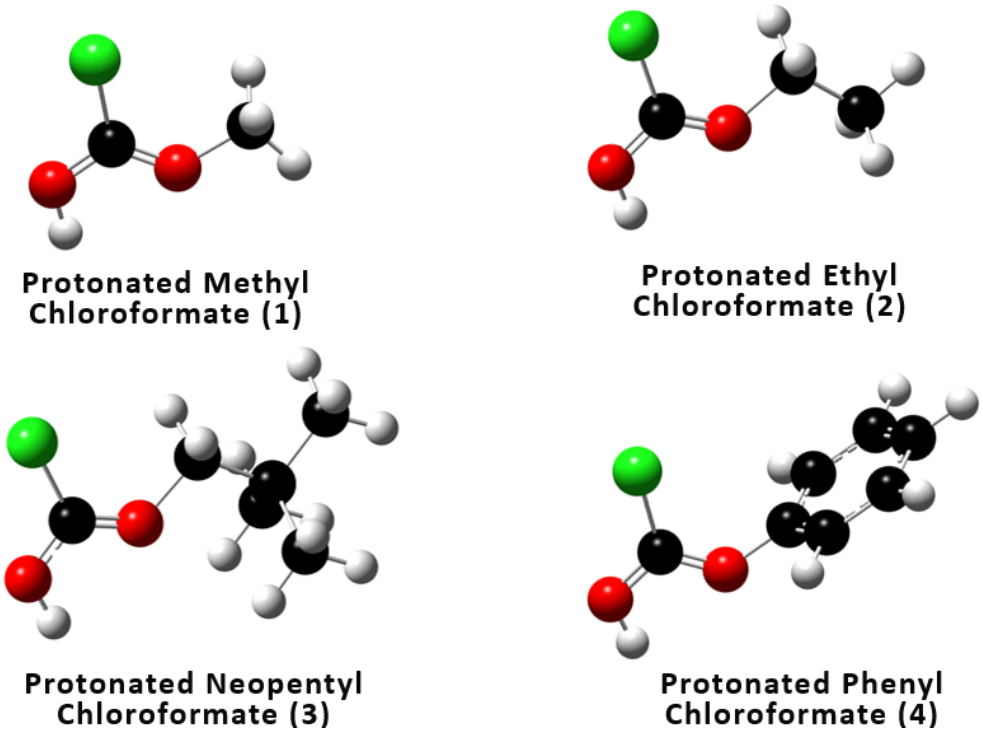

Figure 6.1: Global minimum structure for all calculated protonated chloroformates at the B3LYP/6-311+G(d,p) level of theory.

Unimolecular dissociation rate constants were calculated with Rice-Ramsperger-Kassel-Marcus (RRKM theory) employing the B3LYP/6-311+G(d,p) calculated harmonic vibrational frequencies [60,79].

6.3. Results and Discussion

The MIKE spectra for each protonated chloroformate are shown in *Figure 6.2*. In all cases the ^{35}Cl isotope was selected, but the data was confirmed by also selecting the ^{37}Cl isotope.

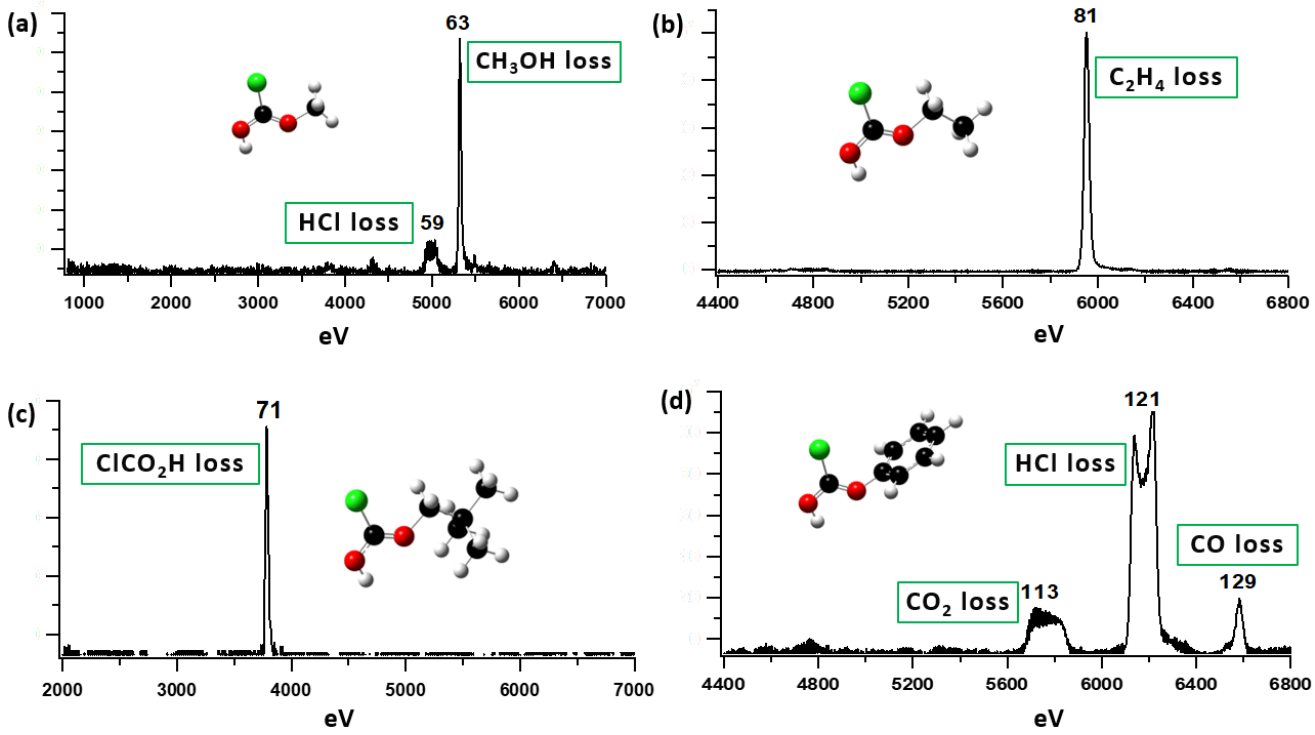

Figure 6.2: MIKE mass spectra of the ^{35}Cl isotope of protonated a) methyl chloroformate (**1**, m/z 95), b) ethyl chloroformate (**2**, m/z 109), c) neopentyl chloroformate (**3**, m/z 151), and d) phenyl chloroformate (**4**, m/z 157). In each case the selected precursor ion (at 8000 eV) is several orders of magnitude greater in abundance than the displayed fragment ions and is omitted for clarity.

As can be seen from *Figure 6.2*, each of the protonated chloroformates has unique fragmentation behaviour. The unimolecular dissociation of the protonated methyl chloroformate **(1)** shows two reactions corresponding to the formation of $CH_3O_2^+$ (m/z 59) + HCl and $ClCO^+$ (m/z 63) + CH_3OH. The primary dissociation pathway for the methyl chloroformate radical cation is loss of Cl, [137] so the current result highlights the differences in the unimolecular chemistry of these two types of ions. Fragmentation of protonated ethyl chloroformate **(2)** leads to the loss of C_2H_4 forming protonated chloroformic acid, $ClCO_2H_2^+$ (m/z 81), while protonated neopentyl chloroformate **(3)** dissociates to make $C_5H_{11}^+$ (m/z 71) + $ClCO_2H$, neutral chloroformic acid. The unimolecular chemistry of protonated phenyl chloroformate **(4)** is more complex with three observed dissociation products, m/z 113, 121 and 129. Loss of CO_2 can form the protonated chlorobenzene ion ($C_6H_6Cl^+$) at m/z 113. HCl loss can form m/z 121 while CO loss forms m/z 129. The broad dish-shaped MIKE peaks for m/z 113 and 121 indicate a large translational energy release for these reactions, which is an indication that the reaction proceeds with a large reverse energy barrier or at least a preferential partitioning of product excess energy into translations.

6.4. Calculated Reaction Mechanisms

The calculated minimum energy reaction pathways (MERPs) for the two dissociation reactions of **1** are shown in *Figure 6.3*. The loss of methanol is initiated by the transfer of the proton from the carbonyl group to the ester oxygen, having an energy requirement of 1.85 eV. This is followed by the loss of CH_3OH, leading to the formation of $ClCO^+$ ion (1.89 eV). The loss of HCl starts by proton transfer from the carbonyl group to the chlorine which generates an ion-molecule complex between HCl and CH_3OCO^+. The calculations are consistent with methanol loss being the observed primary product (the transition state is lower by 0.12 eV) even though the products lie

significantly higher in energy than the loss of HCl to make CH_3OCO^+. A plot of the two RRKM rate constants (*Figure S6.1*) demonstrates the higher rate for methanol loss in the metastable internal energy window.

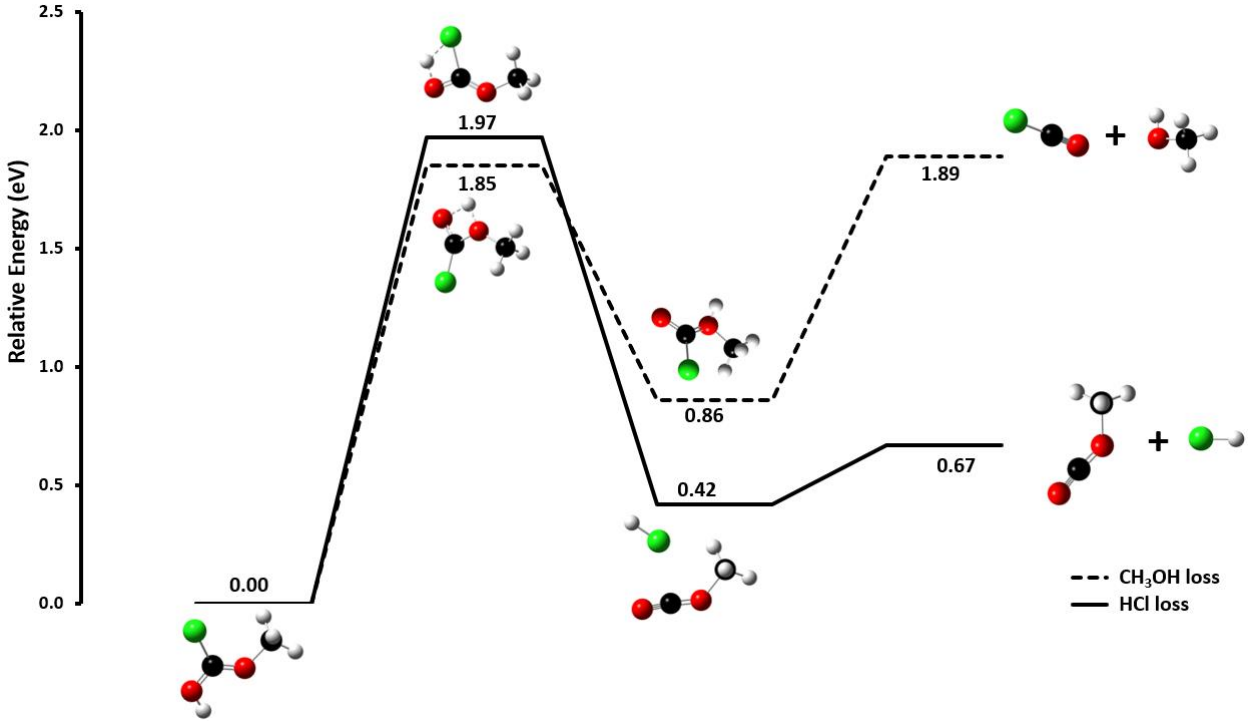

Figure 6.3: CBS-QB3(sp)//B3LYP/6-311+G(d,p) minimum energy reaction pathways for the unimolecular decomposition of **1**.

The dissociation of **2** (*Figure 6.4*) is initiated by a 1,3-H shift (1.92 eV) from the methyl group to form a proton-bound complex between chloroformic acid and C_2H_4 (0.74 eV). This ion then easily loses the neutral C_2H_4 to form protonated chloroformic acid (1.12 eV). Loss of ethanol in a manner analogous to that for methanol loss from **1** lead to products that lie too high in energy to be competitive (2.31 eV). We also calculated loss of CO (also 28 Da) but the resulting products ($CH_3CH_2OClH^+$ + CO) were found to be much too high in energy to be competitive.

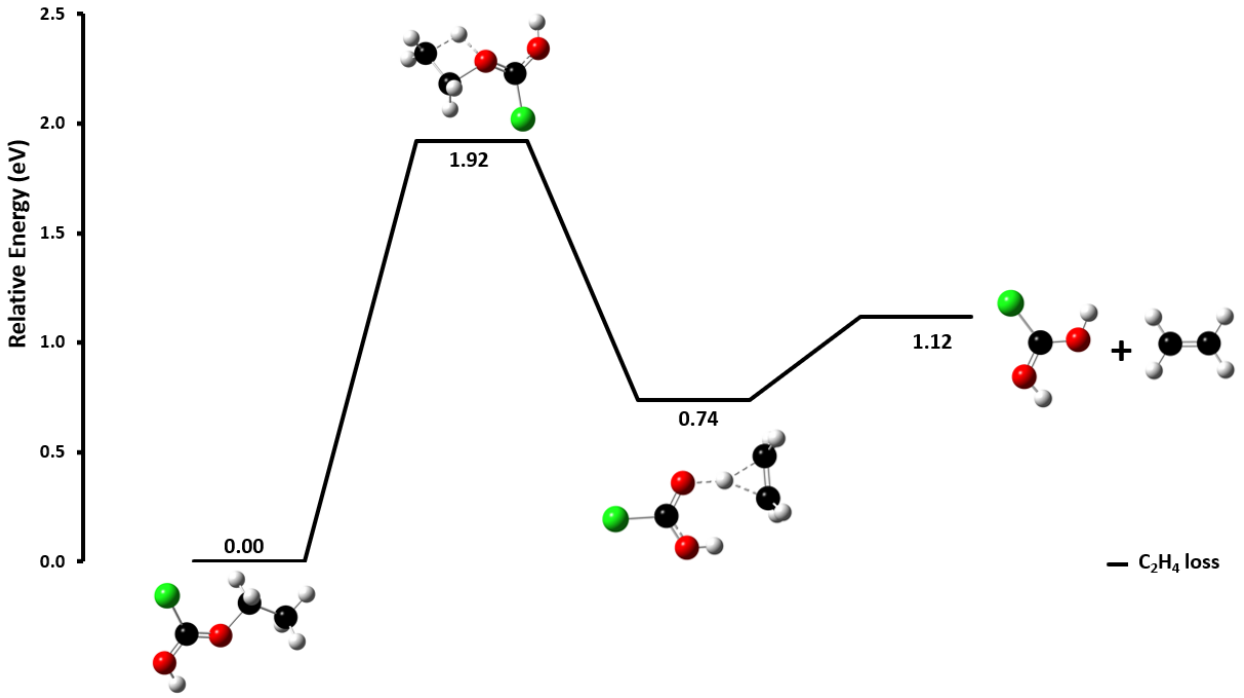

Figure 6.4: CBS-QB3(sp)//B3LYP/6-311+G(d,p) minimum energy reaction pathway for C_2H_4 loss **2**.

The minimum energy reaction pathway of **3** is shown in *Figure 6.5*. The loss of $ClCO_2H$ is initiated by the H-shift from the carbonyl group to the ester oxygen with an energy requirement 1.88 eV. This is followed by C−O bond cleavage (0.95 eV) to form an ion-molecule complex (-0.62 eV). Rather than generating an alcohol (as was observed for **1**; the products for which lie at 2.42 eV relative to **3**), in this complex a CH_3 group has migrated over to the vacant CH_2 group, forming a tertiary carbocation. This complex can directly loose $ClCO_2H$, having an energy requirement of -0.41 eV (*Figure 6.5*).

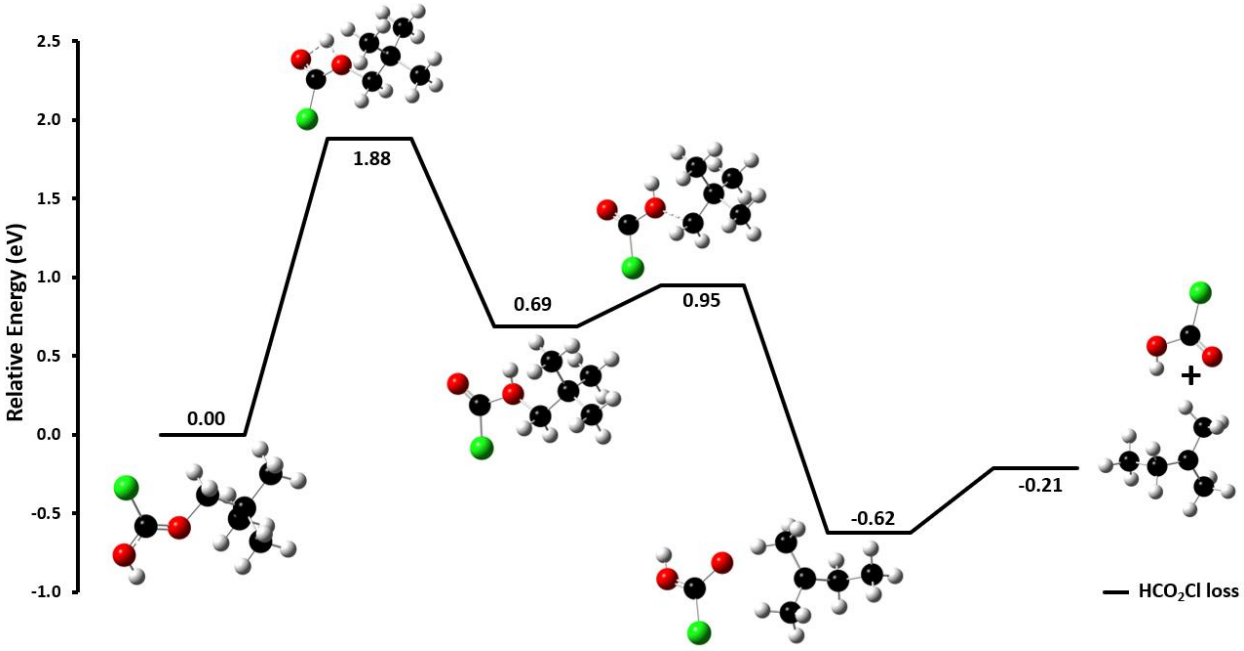

Figure 6.5: CBS-QB3(sp)//B3LYP/6-311+G(d,p) minimum energy reaction pathways for $ClCO_2H$ loss from **3**.

The dissociation of **4** leads to the loss of CO_2, HCl, and CO (*Figure 6.6*). CO_2 loss occurs by a series of hydrogen migrations, initiated by the transfer of the proton from the carbonyl group to the ester oxygen and then to the benzene ring (ortho position), having an energy requirement of 2.03 eV and 1.94 eV respectively. This is followed by either the formation of a proton-bound complex between $C_6H_6OCl^+$ and CO (1.07 eV) which then loses CO (1.96 eV), or an isomerization into a proton-bound complex of $C_6H_6Cl^+$ and CO_2 (-1.11 eV), which can easily loose the neutral carbon dioxide (-1.00 eV). The large reverse barrier to CO_2 loss at the last step is consistent with the observed large translational energy release in the MIKE spectrum. Loss of neutral phenol after the initial 1,3-H shift reaction requires 2.06 eV, making the subsequent H transfer to the ring kinetically competitive. As for the loss of HCl, **4** undergoes proton transfer from the carbonyl group to the chlorine (1.79 eV) to make a complex between HCl and $C_7H_5O_2^+$ (-0.33 eV). This

complex can then lose HCl to form the $C_7H_5O_2^+$ (1.39 eV). Again, a large reverse barrier to form the complex, which is essentially product-like, must partition the excess internal energy into translations resulting in the dish-toped peak in the MIKE spectrum.

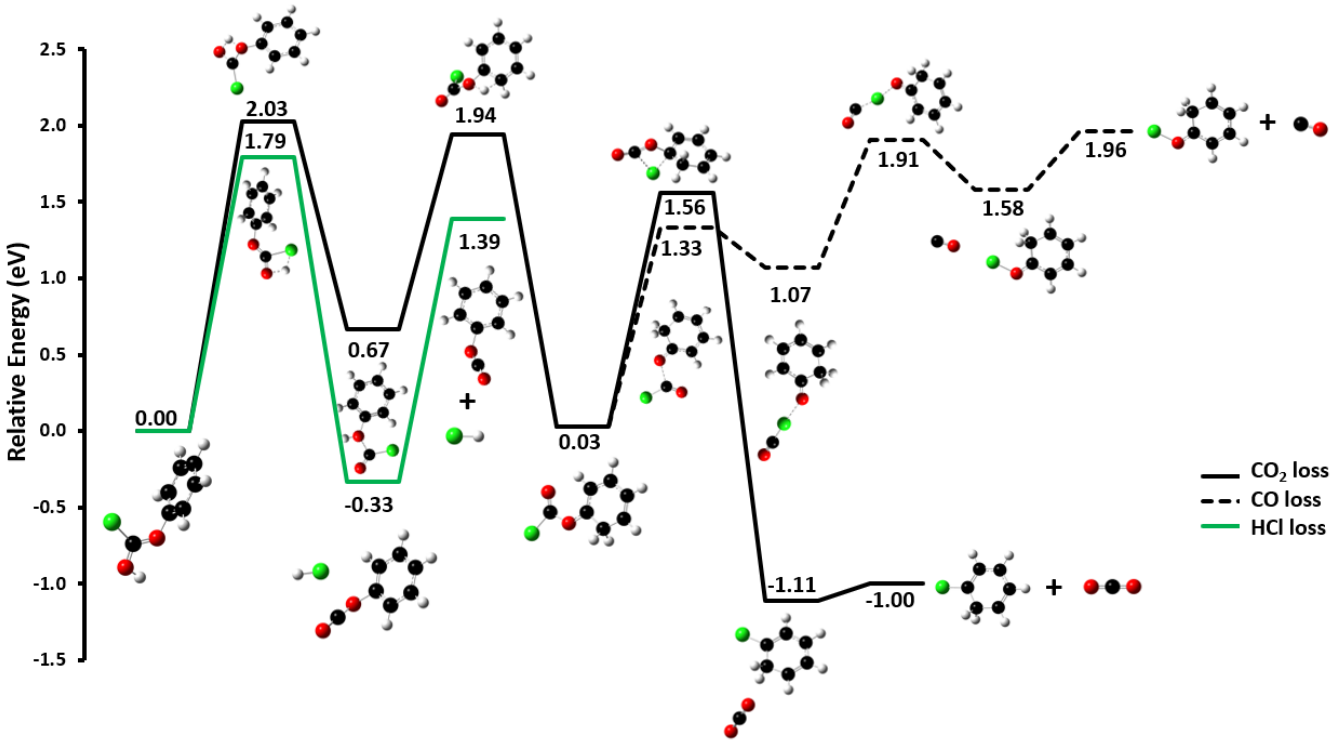

Figure 6.6: CBS-QB3(sp)//B3LYP/6-311+G(d,p) minimum energy reaction pathways for CO_2 loss (—), CO loss (---) and HCl loss (—) from **4**.

6.5. Conclusions

The unimolecular reactions of protonated chloroformates were explored with tandem mass spectrometry and computational chemistry. For protonated methyl **(1)**, neopentyl **(3)**, and phenyl **(4)** chloroformates, a common reaction involves the isomerization of the global minimum structure to one with a protonated ester oxygen. This isomer then leads to ion-molecule complexes which lose CH_3OH **(1)**, $ClCO_2H$ **(2)** and CO_2 and CO **(4)**. The calculated reaction mechanisms highlighted the energetically favorable pathways for these dissociations. Similarly, ethyl

chloroformate dissociated through a 1,3-H shift to lose C_2H_4. These results suggest that the unimolecular dissociation of these protonated chloroformates species can lead to the formation of HCl and chloroformic acid in the atmosphere.

6.6. Appendix

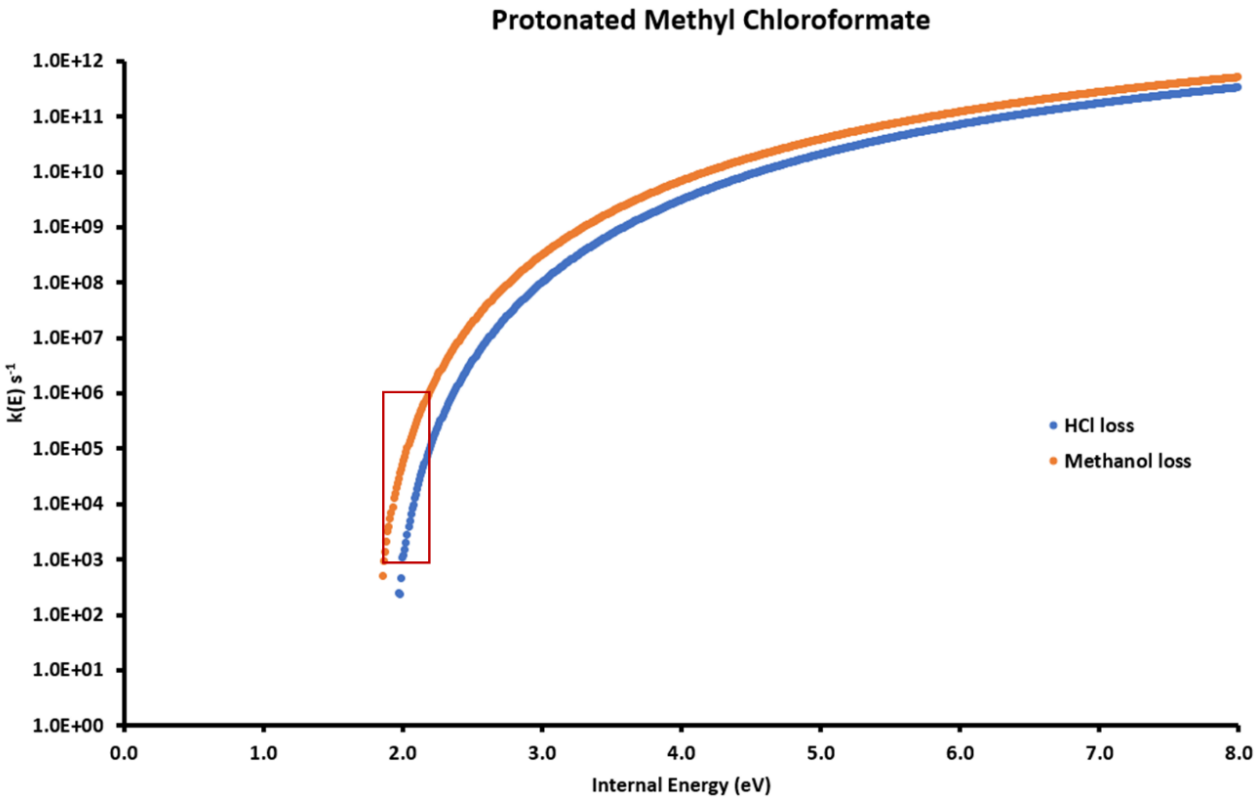

Figure S6.1: RRKM k(E) vs E curves for the dissociation of protonated methyl chloroformate. The region responsible for observations in the MIKE experiment is shown in the box.

CHAPTER 7. CONCLUSIONS

The investigation into ion-molecule reactions involving methyl formate and proton-bound solvent clusters (water, methanol, and ethanol) has provided valuable insights. The primary outcome of these reactions is the formation of protonated methyl formate, underscoring its higher proton affinity compared to water, methanol, and ethanol. Interestingly, a barrierless reaction, common across all solvents, results in the loss of a solvent molecule from the encounter complex. In a secondary, higher-energy reaction, the complex formed between methyl formate and methanol experiences the loss of methane, leading to a proton-bound complex between methanol and CO_2.

These findings suggest that, under higher pressure conditions mimicking atmospheric interactions, encounter complexes between methyl formate and water would be moderately stable, favoring the production of protonated methyl formate, which can subsequently undergo CO loss. Examining ion-molecule reactions between formates and proton-bound water clusters demonstrated that the primary product is protonated formate due to its higher proton affinity. Loss of a water molecule from the encounter complex, occurring without a reverse energy barrier, is observed in all cases. These encounter complexes, stable to dissociation under equilibrium conditions, can lose multiple water molecules, leading to the formation of protonated formate.

The exploration of unimolecular reactions of protonated formates, including methyl, ethyl, and phenyl derivatives, revealed a common pathway involving isomerization to a protonated ester oxygen structure. This isomerization initiates ion-molecule complexes with protonated alcohols and CO, ultimately resulting in CO loss. Notably, as the stability of the R group in ROC(O)H

increases, direct loss of formic acid becomes the dominant pathway, competing with methanol loss. This competitive process is mediated by a series of ion-molecule complexes.

The investigation into protonated chloroformates, encompassing methyl, neopentyl, phenyl, and ethyl derivatives, revealed a common reaction pathway involving isomerization to a structure with a protonated ester oxygen. Subsequent ion-molecule complexes lose CH_3OH, HCO_2Cl, CO_2, CO, and C_2H_4, highlighting energetically favorable dissociation pathways. This comprehensive study, employing tandem mass spectrometry and computational chemistry, provides crucial insights into the atmospheric behavior and dissociation pathways of protonated chloroformates.

Future Outlook

The findings presented in this study pave the way for future research avenues. Further exploration into the gas-phase chemistry of formates and chloroformates, particularly under conditions mimicking atmospheric interactions, is warranted. High-pressure experiments would unveil the dynamics of encounter complexes, which, though not observed in the current low-pressure setting, are predicted to be moderately stable under atmospheric conditions.

Moreover, extending the investigation to other solvents and environmental factors could broaden our understanding of the complex interplay between formates and chloroformates in different atmospheric scenarios. The development of more sophisticated computational models and experimental techniques will be instrumental in refining our comprehension of these processes.

References

1. Nicolet, M. The composition and structure of the terrestrial atmosphere; **1963**. Available online: https://api.semanticscholar.org/CorpusID:222425984 (Accessed on January **2024**).

2. The University corporation for atmospheric research. Layers of earth's atmosphere. Available online: https://scied.ucar.edu/atmosphere-layers (Accessed on April **2023**).

3. Samala, N.R.; Agmon, N. Thermally induced hydrogen-bond rearrangements in small water clusters and the persistent water tetramer. *ACS Omega* **2019**, *4*, 22581-22590, doi:10.1021/acsomega.9b03326.

4. Kildgaard, J.V.; Mikkelsen, K.V.; Bilde, M.; Elm, J. Hydration of atmospheric molecular clusters II: organic acid-water clusters. *J. Phys. Chem. A* **2018**, *122*, 8549-8556, doi:10.1021/acs.jpca.8b07713.

5. Zhang, T.; Wen, M.; Zhang, Y.; Lan, X.; Long, B.; Wang, R.; Yu, X.; Zhao, C.; Wang, W. Atmospheric chemistry of the self-reaction of HO_2 radicals: Stepwise mechanism versus one-step process in the presence of $(H_2O)n$ (n = 1-3) clusters. *Phys. Chem. Chem. Phys.* **2019**, *21*, 24042-24053, doi:10.1039/c9cp03530c.

6. Anglada, J.M.; Hoffman, G.J.; Slipchenko, L.V.; M.costa, M.; Ruiz-López, M.F.; Francisco, J.S. Atmospheric significance of water clusters and ozone-water complexes. *J. Phys. Chem. A* **2013**, *117*, 10381-10396, doi:10.1021/jp407282c.

7. Goken, E.G.; Castleman, A.W. Reactions of formic acid with protonated water clusters: Implications of cluster growth in the atmosphere. *J. Geophys. Res. Atmos.* **2010**, *115*, 1-8, doi:10.1029/2009JD013249.

8. Vaida, V. Perspective: Water cluster mediated atmospheric chemistry. *J. Chem. Phys.* **2011**, *135*, doi:10.1063/1.3608919.

9. Zhang, T.; Yang, C.; Feng, X.; Kang, J.; Song, L.; Lu, Y.; Wang, Z.; Xu, Q.; Wang, W.; Wang, Z. The catalytic effect of water, water dimers and water trimers on $H_2S + 3O_2$ formation by the HO_2 + HS reaction under tropospheric conditions. *Phys. Chem. Chem. Phys.* **2016**, *18*, 17414-17427, doi:10.1039/c6cp00654j.

10. Gerber, R.B.; Varner, M.E.; Hammerich, A.D.; Riikonen, S.; Murdachaew, G.; Shemesh, D.; Finlayson-Pitts, B.J. Computational studies of atmospherically-relevant chemical reactions in water clusters and on liquid water and ice surfaces. *Acc. Chem. Res.* **2015**, *48*, 399-406, doi:10.1021/ar500431g.

11. Heald, C.L.; Kroll, J.H. The fuel of atmospheric chemistry: Toward a complete description of reactive organic carbon. *Sci. Adv.* **2020**, *6*, 1-9, doi:10.1126/sciadv.aay8967.

12. Xiong, Y.; Aynul Bari, M.; Xing, Z.; Du, K. Ambient volatile organic compounds (VOCs) in two coastal cities in western Canada: Spatiotemporal variation, source apportionment, and health risk assessment. *Sci. Total Environ.* **2020**, *706*, 135970-135970, doi:10.1016/j.scitotenv.2019.135970.

13. Huang, J.; Hartmann, H.; Hellén, H.; Wisthaler, A.; Perreca, E.; Weinhold, A.; Rücker, A.; Van Dam, N.M.; Gershenzon, J.; Trumbore, S.; et al. New perspectives on CO_2 , temperature, and light effects on BVOC emissions using online measurements by PTR-MS and cavity ring-down spectroscopy. *Environ. Sci. Technol.* **2018**, *52*, 13811-13823, doi:10.1021/acs.est.8b01435.

14. Kroll, J.H.; Lim, C.Y.; Kessler, S.H.; Wilson, K.R. Heterogeneous oxidation of atmospheric organic aerosol: Kinetics of changes to the amount and oxidation state of particle-phase organic carbon. *J. Phys. Chem. A* **2015**, *119*, 10767-10783, doi:10.1021/acs.jpca.5b06946.

15. Ryzhkov, A.B.; Ariya, P.A. The importance of water clusters $(H_2O)n$ (n = 2, ... , 4) in the reaction of Criegee intermediate with water in the atmosphere. *Chem. Phys. Lett.* **2006**, *419*, 479-485, doi:10.1016/j.cplett.2005.12.016.

16. Poštulka, J.; Slavíček, P.; Domaracka, A.; Pysanenko, A.; Fárník, M.; Kočišek, J. Proton transfer from pinene stabilizes water clusters. *Phys. Chem. Chem. Phys.* **2019**, *21*, 13925-13933, doi:10.1039/c8cp05959d.

17. Inaba, S. Theoretical study of water cluster catalyzed decomposition of formic acid. *J. Phys. Chem. A* **2014**, *118*, 3026-3038, doi:10.1021/jp5021406.

18. Iraqi, M.; Lifshitz, C. Studies of ion clusters of atmospheric importance by tandem mass spectrometry. Neat and mixed clusters involving methanol and water. *Int. J. Mass Spectrom. Ion Processes* **1989**, *88*, 45-58, doi:10.1016/0168-1176(89)80041-2.

19. Lv, S.S.; Miao, S.K.; Ma, Y.; Zhang, M.M.; Wen, Y.; Wang, C.Y.; Zhu, Y.P.; Huang, W. Properties and atmospheric implication of methylamine-sulfuric acid-water clusters. *J. Phys. Chem. A* **2015**, *119*, 8657-8666, doi:10.1021/acs.jpca.5b03325.

20. Breitenlechner, M.; Fischer, L.; Hainer, M.; Heinritzi, M.; Curtius, J.; Hansel, A. PTR3: An instrument for studying the lifecycle of reactive organic carbon in the atmosphere. *Anal. Chem.* **2017**, *89*, 5824-5831, doi:10.1021/acs.analchem.6b05110.

21. Guo, J.; Pugliesi, I.; Müller-Dethlefs, K.; Dessent, C.E.H. Multidimensional Franck-Condon simulations of photodetachment spectra for the formate-water cluster anion: Investigating H atom transfer along the HCOOH+OH reaction coordinate. *J. Chem. Phys.* **2007**, *127*, doi:10.1063/1.2805188.

22. Legrand, M.; Preunkert, S.; Jourdain, B.; Aumont, B. Year-round records of gas and particulate formic and acetic acids in the boundary layer at Dumont d'Urville, coastal Antarctica. *J. Geophys. Res. D: Atmos.* **2004**, *109*, 1-11, doi:10.1029/2003jd003786.

23. Boring, C.B.; Al-Horr, R.; Genfa, Z.; Dasgupta, P.K.; Martin, M.W.; Smith, W.F. Field measurement of acid gases and soluble anions in atmospheric particulate matter using a parallel plate wet denuder and an alternating filter-based automated analysis system. *Anal. Chem.* **2002**, *74*, 1256-1268, doi:10.1021/ac015643r.

24. Khare, P.; Kumar, N.; Kumari, K.M.; Srivastava, S.S. Atmospheric formic and acetic acids: An overview. *Rev. of Geophys.* **1999**, *37*, 227-248, doi:10.1029/1998RG900005.

25. Grosjean, D. Organic acids in southern California air: Ambient concentrations, mobile source emissions, in situ formation and removal processes. *Environ. Sci. Technol.* **1989**, *23*, 1506-1514, doi:10.1021/es00070a009.

26. Sabbioni, C.; Ghedini, N.; Bonazza, A. Organic anions in damage layers on monuments and buildings. *Atmos. Environ.* **2003**, *37*, 1261-1269, doi:10.1016/S1352-2310(02)01025-7.

27. Wallington, T.J.; Hurley, M.D.; Maurer, T.; Barnes, I.; Becker, K.H.; Tyndall, G.S.; Orlando, J.J.; Pimentel, A.S.; Bilde, M. Atmospheric oxidation mechanism of methyl formate. *J. Phys. Chem. A* **2001**, *105*, 5146-5154, doi:10.1021/jp0041398.

28. Wu, J.; Ning, H.; Ma, L.; Ren, W. Pressure-dependent kinetics of methyl formate reactions with OH at combustion, atmospheric and interstellar temperatures. *Phys. Chem. Chem. Phys.* **2018**, *20*, 26190-26199, doi:10.1039/c8cp04114h.

29. Hendriyana; Susanto, H.; Subagjo. Atmospheric hydrogenolysis of methyl formate to bio-methanol using Cu/MgO catalyst. *AIP Conf. Proc.* **2017**, vol. 1904, no. 1, https://doi.org/10.1063/1.5011862.

30. Bell, M.J.; Lau, K.C.; Krisch, M.J.; Bennett, D.I.G.; Butler, L.J.; Weinhold, F. Characterization of the methoxy carbonyl radical formed via photolysis of methyl chloroformate at 193.3 nm. *J. Phys. Chem. A* **2007**, *111*, 1762-1770, doi:10.1021/jp066056i.

31. Reitmeier, S.J.; Balaj, O.P.; Bondybey, V.E.; Beyer, M.K. Reactions of hydrated electrons $(H_2O)n^-$ with formic acid. *Int. J. Mass Spectrom.* **2006**, *249-250*, 106-111, doi:10.1016/j.ijms.2006.01.006.

32. Bruins, A.P. Mass spectrometry with ion sources operating at atmospheric pressure. *Mass Spectrom. Rev.* **1991**, *10*, 53-77, doi:https://doi.org/10.1002/mas.1280100104.

33. Xu, S.; Zhang, Y.; Errabelli, R.; Attygalle, A.B. Ambulation of incipient proton during gas-phase dissociation of protonated alkyl dihydrocinnamates. *J. Org. Chem.* **2015**, *80*, 9468-9479, doi:10.1021/acs.joc.5b01390.

34. Ding, L.; Kumashiro, S. Ion motion in the rectangular wave quadrupole field and digital operation mode of a quadrupole ion trap mass spectrometer. *Rapid Commun. Mass Spectrom.* **2006**, *20*, 3-8, doi:10.1002/rcm.2253.

35. March, R.E.; Todd, J.F.J. Quadrupole ion trap mass spectrometry, 2nd ed.; Wiley-Interscience: Hoboken, *N.J*, **2005**.

36. Mathieu, É. Mémoire sur le mouvement vibratoire d'une membrane de forme elliptique. *J. Math. Pures Appl.* **1868**, *13*.

37. Mikhail, S.; Maria, A. Perturbation theory for ion motion in quadrupole radio frequency field. *Int. J. Mass Spectrom.* **2012**, *325-327*, 58-66, doi:10.1016/j.ijms.2012.07.019.

38. Michaud, A.L.; Frank, A.J.; Ding, C.; Zhao, X.; Douglas, D.J. Ion excitation in a linear quadrupole ion trap with an added octopole field. *J. Am. Soc. Mass Spectrom.* **2005**, *16*, 835-849, doi:10.1016/j.jasms.2005.02.006.

39. March, R.E. An introduction to quadrupole ion trap mass spectrometry. *J. Mass Spectrom.* **1997**, *32*, 351-369, doi:10.1002/(SICI)1096-9888(199704)32:4<351::AID-JMS512>3.0.CO;2-Y.

40. Ho, C.S.; Lam, C.W.K.; Chan, M.H.M.; Cheung, R.C.K.; Law, L.K.; Lit, L.C.W.; Ng, K.F.; Suen, M.W.M.; Tai, H.L. Electrospray ionisation mass spectrometry: Principles and clinical applications. *Clin. Biochem. Rev.* **2003**, *24*, 3-12.

41. Cooks, R.G. Metastable ions. *Elsevier Scientific Pub. Co.: Amsterdam* **1973**.

42. West, B.; Joblin, C.; Blanchet, V.; Bodi, A.; Sztáray, B.; Mayer, P.M. On the dissociation of the naphthalene radical cation: New ipepico and tandem mass spectrometry results. *J. Phys. Chem A* **2012**, *116*, 10999-11007, doi:10.1021/jp3091705.

43. William, K. Encyclopedia of chemical physics and physical chemistry encyclopedia of chemical physics and physical chemistry , John H. Moore and Nicholas D. Spencer , eds. volume 1: Fundamentals volume 2: Methods volume 3: Applications IOP. *Phy. today* **2003**, *56*, 66-67, doi:10.1063/1.1564357.

44. Holmes, J.L.; Mayer, P.M. Proton affinities of primary alkanols: An appraisal of the kinetic method. *J. Phys. Chem. A* **1999**, *103*, 6492-6492, doi:10.1021/jp9919617.

45. Cances, E. A mathematical introduction to Density Functional Theory and Kohn-Sham models (REVIEW) **2019**, UBC cIRcle BIRS workshop lecture videos (Accessed on June **2023**).

46. Lewars, Errol G. Computational chemistry : Introduction to the theory and applications of molecular and quantum mechanics, Third edition *ed. Springer: Switzerland* **2016**.

47. Kohanoff, J.; Gidopoulos, N. Density Functional Theory: Basics, new trends and applications. *Handbook of Molecular Physics and Quantum Chemistry* **2003**, *2*.

48. Cramer, Christopher J. Essentials of computational chemistry : Theories and models. *Wiley* **2004**, 2nd Edition.

49. Krishnakumar, V.; Keresztury, G.; Sundius, T.; Ramasamy, R. Simulation of IR and Raman spectra based on scaled DFT force fields: a case study of 2-(methylthio) benzonitrile, with emphasis on band assignment. *J. Mol. Struct.* **2004**, *702*, 9-21, doi:10.1016/j.molstruc.2004.06.004.

50. Barone, V.; Bloino, J.; Biczysko, M.; Santoro, F. Fully integrated approach to compute vibrationally resolved optical spectra: From small molecules to macrosystems. *J. Chem. Theory Comput.* **2009**, *5*, 540-554, doi:10.1021/ct8004744.

51. Frisch, M.J.; Trucks, G.W.; Schlegel, H.B.; Scuseria, G.E.; Robb, M.A.; Cheeseman, J.R.; Scalmani, G.; Barone, V.; Petersson, G.A.; Nakatsuji, H.; et al. *Gaussian 16 Rev. B.01*, Wallingford, CT, **2016**.

52. Di Giacomo, F. A Short Account of RRKM theory of unimolecular reactions and of Marcus theory of electron transfer in a historical perspective. *J. Chem. Educ.* **2015**, *92*, 476-481, doi:10.1021/ed5001312.

53. Lindemann, F.A.; Arrhenius, S.; Langmuir, I.; Dhar, N.R.; Perrin, J.; McC. Lewis, W.C. Discussion on "the radiation theory of chemical action". *Trans. Faraday Soc.* **1922**, *17*, 598-606, doi:10.1039/TF9221700598.

54. Rice, O.K.; Ramsperger, H.C. Theories of unimolecular gas reactions at low pressures. *J. Am. Chem. Soc.* **1927**, *49*, 1617-1629.

55. Kassel, L.S. Studies in homogeneous gas reactions I. *J. Phys. Chem.* **1928**, *32*, 225-242.

56. Marcus, R.A. Unimolecular dissociations and free radical recombination reactions. *J.Chem. Phys.* **1952**, *20*, 359-364.

57. Kim, G.-S.; Nguyen, T.L.; Mebel, A.M.; Lin, S.H.; Nguyen, M.T. Ab initio/RRKM study of the potential energy surface of triplet ethylene and product branching ratios of the $C(^3P) + CH_4$ reaction. *J. Phys. Chem. A* **2003**, *107*, 1788-1796, doi:10.1021/jp0261410.

58. Sivy, G.T. Discoloration of elastomeric joint sealants. *Adhesives & Sealants Industry* **2013**, *20*, 30-42.

59. Green, W.H.; Moore, C.B.; Polik, W.F. Transition states and rate constants for unimolecular reactions. *Annu. Rev. Phys. Chem.* **1992**, *43*, 591-626, doi:10.1146/annurev.pc.43.100192.003111.

60. Baer, T.; Hase, W.L. *Unimolecular Reaction Dynamics, Theory And Experiments*; Oxford University Press: New York, **1996**.

61. Baer, T.; Mayer, P.M. Statistical Rice-Ramsperger-Kassel-Marcus quasiequilibrium theory calculations in mass spectrometry. *J. Am. Soc. Mass Spectrom.* **1997**, *8*, 103-115.

62. Rivett, A.C.; Martin, D.; Gray, D.J.; Price, C.S.; Nickless, G.; Simmonds, P.G.; O'Doherty, S.J.; Greally, B.R.; Knights, A.; Shallcross, D.E. The role of volatile organic compounds in the polluted urban atmosphere of Bristol, UK. *Atmos. Chem. Phys.* **2003**, *3*, 769-796.

63. Xiong, Y.; Bari, M.A.; Xing, Z.; Du, K. Ambient volatile organic compounds (VOCs) in two coastal cities in western Canada: Spatiotemporal variation, source apportionment, and health risk assessment. *Sci. Total Environ.* **2020**, *706*, 135970, doi:https://doi.org/10.1016/j.scitotenv.2019.135970.

64. Wallington, T.J.; Hurley, M.D.; Maurer, T.; Barnes, I.; Becker, K.H.; Tyndall, G.S.; Orlando, J.J.; Pimentel, A.S.; Bilde, M. Atmospheric oxidation mechanism of methyl formate. *J. Phys. Chem. A*, **2001**, *105*, 5146-5154, doi:10.1021/jp0041398.

65. Sinha, A.; Thomson, M.J. The chemical structures of opposed flow diffusion flames of C3 oxygenated hydrocarbons (isopropanol, dimethoxy methane, and dimethyl carbonate) and their mixtures. *Combust. flame* **2004**, *136*, 548-556, doi:10.1016/j.combustflame.2003.12.011.

66. Daly, C.A.; Simmie, J.M.; Dagaut, P.; Cathonnet, M. Oxidation of dimethoxymethane in a jet-stirred reactor. *Combust. flame* **2001**, *125*, 1106-1117, doi:10.1016/S0010-2180(01)00227-9.

67. Liu, I.; Cant, N.W.; Bromly, J.H.; Barnes, F.J.; Nelson, P.F.; Haynes, B.S. Formate species in the low-temperature oxidation of dimethyl ether. *Chemosphere* **2001**, *42*, 583-589.

68. Bertin, M.; Romanzin, C.; Michaut, X.; Jeseck, P.; Fillion, J.H. Adsorption of organic isomers on water ice surfaces: A study of acetic acid and methyl formate. *J. Phys. Chem. C* **2011**, *115*, 12920-12928, doi:10.1021/jp201487u.

69. Goken, E.G.; Castleman Jr, A.W. Reactions of formic acid with protonated water clusters: Implications of cluster growth in the atmosphere. *J. Geophys. Res.* **2010**, *115*, n/a, doi:10.1029/2009JD013249.

70. Zheng, Z.; Pavlov, J.; Attygalle, A.B. Fortuitous ion–molecule reaction enables enumeration of metal–hydrogen bonds present in gaseous ions. *ACS Omega* **2019**, *4*, 3965-3972, doi:10.1021/acsomega.8b03341.

71. Osburn, S.; Ryzhov, V. Ion–molecule reactions: Analytical and structural tool. *Anal. chem.* **2013**, *85*, 769-778, doi:10.1021/ac302920a.

72. Španěl, P.; Pavlik, M.; Smith, D. Reactions of H_3O^+ and OH^- ions with some organic molecules; applications to trace gas analysis in air. *Int. J. Mass Spectrom. Ion Processes* **1995**, *145*, 177-186, doi:10.1016/0168-1176(95)04164-G.

73. Adams, N.G.; Smith, D. The selected ion flow tube (SIFT); A technique for studying ion-neutral reactions. *Int. J. Mass Spectrom. Ion Phys.* **1976**, *21*, 349-359, doi:10.1016/0020-7381(76)80133-7.

74. Smith, D.; Španěl, P. Selected ion flow tube mass spectrometry (SIFT-MS) for on-line trace gas analysis. *Mass Spectrom. Rev.* **2005**, *24*, 661-700, doi:10.1002/mas.20033.

75. Curtis, S.; DiMuzio, J.; Mungham, A.; Roy, J.; Hassan, D.; Renaud, J.; Mayer, P.M. Reactions of atomic metal anions in the gas phase: Competition between electron transfer, proton abstraction and bond activation. *J. Phys. Chem.* A **2011**, *115*, 14006-14012, doi:10.1021/jp2086736.

76. Cooks, R.G. Collision spectroscopy; *Plenum Press: West Lafayette, Ind.* **1977**.

77. Becke, A.D. Density-functional thermochemistry. III. The role of exact exchange. *J. Chem. Phys.* **1993**, *98*, 5648-5652, doi:10.1063/1.464913.

78. Lee, C.; Yang, W.; Parr, R.G. Development of the Colle-Salvetti correlation-energy formula into a functional of the electron density. *Phys. Rev. B* **1988**, *37*, 785-789, doi:10.1103/PhysRevB.37.785.

79. Green, N., Comprehensive chemical kinetics: Unimolecular kinetics, part 1. the reaction step. *Elsevier Science* **2003**, vol. 3.

80. Beyer, T.; Swinehart, D.R. Number of multiply-restricted Partitions [A1] (Algorithm 448). *ACM Commun.* **1973**, *16*, 379.

81. Mayer, P.M.; Martineau, E. Gas-phase binding energies for non-covalent Aβ-40 peptide/small molecule complexes from CID mass spectrometry and RRKM theory. *Phys. Chem. Chem. Phys.* **2011**, *13*, 5178-5186, doi:10.1039/c0cp02149k.

82. Renaud, J.B.; Martineau, E.; Mironov, G.G.; Berezovski, M.V.; Mayer, P.M. The collaborative role of molecular conformation and energetics in the binding of gas-phase non-covalent polymer/amine complexes. *Phys. Chem. Chem. Phys.* **2012**, *14*, 165-172.

83. Diedhiou, M.; Mayer, P.M. Fate of protonated formates in the gas phase. *J. Phys. Chem. A* **2021**, *125*, 5096-5102, doi:10.1021/acs.jpca.1c03814.

84. Hunter, E.P.L.; Lias, S.G. Evaluated gas phase basicities and proton affinities of molecules: An update. *J. Phys. Chem. Ref. Data.* **1998**, *27*, 413-656, doi:10.1063/1.556018.

85. Vaida, V. Perspective: Water cluster mediated atmospheric chemistry. *J. chem. phys.* **2011**, *135*, 020901-020901-020908, doi:10.1063/1.3608919.

86. Alecia M. English, Jaron C. Hansen*, Joseph J. Szente, and M. Matti Maricq. The effects of water vapor on the CH_3O_2 self-reaction and reaction with HO_2. *J. Phys. Chem. A* **2008**, 112, 39, 9220–9228, https://doi.org/10.1021/jp800727a

87. Zhang, T.; Yang, C.; Feng, X.; Kang, J.; Song, L.; Lu, Y.; Wang, Z.; Xu, Q.; Wang, W.; Wang, Z. The catalytic effect of water, water dimers and water trimers on $H_2S + 3O_2$ formation by the HO_2 + HS reaction under tropospheric conditions. *Chem. Chem. Phys.* **2016**, *18*, 17414-17427, doi:10.1039/c6cp00654j.

88. Heald, C.L.; Kroll, J.H. The fuel of atmospheric chemistry: Toward a complete description of reactive organic carbon. *Sci. Adv.* **2020**, *6*, doi:10.1126/sciadv.aay8967.

89. Huang, J.; Hartmann, H.; Hellén, H.; Wisthaler, A.; Perreca, E.; Weinhold, A.; Rücker, A.; van Dam, N.M.; Gershenzon, J.; Trumbore, S. New perspectives on CO_2 , temperature, and

light effects on BVOC emissions using online measurements by PTR-MS and cavity ring-down spectroscopy. *Environ. Sci. Technol.* **2018**, *52*, 13811.

90. Inaba, S. Theoretical study of water cluster catalyzed decomposition of formic acid. *J. Phys. Chem. A* **2014**, *118*, 3026-3038, doi:10.1021/jp5021406.

91. Sabbioni, C.; Ghedini, N.; Bonazza, A. Organic anions in damage layers on monuments and buildings. *Atmos. Environ.* **2003**, *37*, 1261-1269, doi:10.1016/S1352-2310(02)01025-7.

92. Legrand, M.; Preunkert, S.; Jourdain, B.; Aumont, B. Year-round records of gas and particulate formic and acetic acids in the boundary layer at Dumont d'Urville, coastal Antarctica. *J. Geophys. Res. Atmos.* **2004**, *109*, D06313-n/a, doi:10.1029/2003JD003786.

93. Boring, C.B.; Genfa, Z.; Dasgupta, P.K.; Martin, M.W.; Smith, W.F. Field measurement of acid gases and soluble anions in atmospheric particulate matter using a parallel plate wet denuder and an alternating filter-based automated analysis system. *Anal. chem.* **2002**, *74*, 1256-1268, doi:10.1021/ac015643r.

94. Wu, J.; Ning, H.; Ma, L.; Ren, W. Pressure-dependent kinetics of methyl formate reactions with OH at combustion, atmospheric and interstellar temperatures. *Chem. Chem. Phys. PCCP* **2018**, *20*, 26190-26199, doi:10.1039/C8CP04114H.

95. Bell, M.J.; Lau, K.C.; Krisch, M.J.; Bennett, D.I.G.; Butler, L.J.; Weinhold, F. Characterization of the methoxy carbonyl radical formed via photolysis of methyl chloroformate at 193.3 nm. *J. Phys. Chem. A* **2007**, *111*, 1762-1770, doi:10.1021/jp066056i.

96. Pimentel, A.S.; Tyndall, G.S.; Orlando, J.J.; Hurley, M.D.; Wallington, T.J.; Sulbaek Andersen, M.P.; Marshall, P.; Dibble, T.S. Atmospheric chemistry of isopropyl formate and tert-butyl formate. *Int. J. Chem. Kinet.* **2010**, *42*, 479-498, doi:https://doi.org/10.1002/kin.20498.

97. Diedhiou, M.; Mayer, P.M. The Interaction of methyl formate with proton-bound solvent clusters in the gas phase and the unimolecular chemistry of the reaction products. *Appl. Sci.* **2023**, *13*, 1339, doi:10.3390/app13031339.

98. Johnson, Andrew R., and Erin E. Carlson. Collision-Induced Dissociation mass spectrometry: A powerful tool for natural product structure elucidation. *Anal. Chem.* **2015**, 87, 21, 10668–10678, https://doi.org/10.1021/acs.analchem.5b01543.

99. West, B.; Sit, A.; Mohamed, S.; Joblin, C.; Blanchet, V.; Bodi, A.; Mayer, P.M. Dissociation of the anthracene radical cation: A comparative look at iPEPICO and collision-induced dissociation mass spectrometry results. *J. Phys. Chem. A* **2014**, *118*, 9870-9878, doi:10.1021/jp505438f.

100. Grosjean, D. Organic acids in Southern California air: Ambient concentrations, mobile source emissions, in situ formation and removal processes. *Environ. Sci. Technol.* **1989**, *23*, 1506-1514, doi:10.1021/es00070a009.

101. Cruz, L.; Mota, E.; Campos, V.; Santana, F.; Luz, S.; Santos, D. Inorganic and organic acids in the atmosphere of the urban area of the city of Salvador, Brazil. *J. Braz. Chem. Soc.* **2018**, *30*, 904-914, doi:10.21577/0103-5053.20180227.

102. Xu, Y.; Nadykto, A.B.; Yu, F.; Herb, J.; Wang, W. Interaction between common organic acids and trace nucleation species in the earth's atmosphere. *J. Phys. Chem. A* **2010**, *114*, 387-396, doi:10.1021/jp9068575.

103. Ludwig, J.; Klemm, O. Organic acids in different size classes of atmospheric particulate material. *Tellus B: Chem. Phys. Meteorol.* **1988**, *40*, 340-347, doi:10.3402/tellusb.v40i5.15997.

104. Deshmukh, D.K.; Haque, M.M.; Kim, Y.; Kawamura, K. Organic tracers of fine aerosol particles in central Alaska: Summertime composition and sources. *Atmos. Chem. Phys.* **2019**, *19*, 14009-14029, doi:10.5194/acp-19-14009-2019.

105. Franco, B.; Clarisse, L.; Stavrakou, T.; Müller, J.F.; Taraborrelli, D.; Hadji-Lazaro, J.; Hannigan, J.W.; Hase, F.; Hurtmans, D.; Jones, N. Spaceborne measurements of formic and acetic acids: a global view of the regional sources. *Geophys. Res. Lett.* **2020**, *47*, n/a, doi:10.1029/2019GL086239.

106. Talbot, R.W.; Mosher, B.W.; Heikes, B.G.; Jacob, D.J.; Munger, J.W.; Daube, B.C.; Keene, W.C.; Maben, J.R.; Artz, R.S. Carboxylic acids in the rural continental atmosphere over the eastern United States during the Shenandoah cloud and photochemistry experiment. *J. Geophys. Res. Atmos* **1995**, *100*, 9335-9343, doi:10.1029/95JD00507.

107. Anglada, J.M.; Gonzalez, J. Different catalytic effects of a single water molecule: The gas-phase reaction of formic acid with hydroxyl radical in water vapor. *Chem. Phys. Chem.* **2009**, *10*, 3034-3045, doi:10.1002/cphc.200900387.

108. Cordova-Gomez, M.; Iuga, C.; Alvarez-Idaboy, J.R. Mechanisms and rate constants in the atmospheric oxidation of saturated esters by hydroxyl radicals: A theoretical study. *Int. J. Quantum Chem.* **2012**, *112*, 3508-3515, doi:10.1002/qua.24149.

109. Du, B.; Zhang, W. Atmospheric oxidation chemistry of 1-methoxy 2-propyl acetate initiated by OH radicals: Kinetics and mechanisms. *Mol. Phys.* **2020**, *118*, e1601786, doi:10.1080/00268976.2019.1601786.

110. Atkinson, R.; Lloyd, A. C. Evaluation of kinetic and mechanistic data for modeling of photochemical smog. *J. Phys. Chem. Ref. Data.* **1984**, *13*, 315-444, doi:10.1063/1.555710.

111. Min, K.E.; Washenfelder, R.A.; Dubé, W.P.; Langford, A.O.; Edwards, P.M.; Zarzana, K.J.; Stutz, J.; Lu, K.; Rohrer, F.; Zhang, Y.; et al. A broadband cavity enhanced absorption spectrometer for aircraft measurements of glyoxal, methylglyoxal, nitrous acid, nitrogen dioxide, and water vapor. *Atmos. Meas. Tech.* **2016**, *9*, 423-440, doi:10.5194/amt-9-423-2016.

112. Baasandorj, M.; Millet, D.B.; Hu, L.; Mitroo, D.; Williams, B.J. Measuring acetic and formic acid by proton-transfer reaction mass spectrometry: Sensitivity, humidity

dependence, and quantifying interferences. *Atmos. Meas. Tech.* **2015**, *8*, 1303-1321, doi:10.5194/amt-8-1303-2015.

113. Bruns, E.A.; Slowik, J.G.; El Haddad, I.; Kilic, D.; Klein, F.; Dommen, J.; Temime-Roussel, B.; Marchand, N.; Baltensperger, U.; PrévÃ´t, A.S.H. Characterization of gas-phase organics using proton transfer reaction time-of-flight mass spectrometry: Fresh and aged residential wood combustion emissions. *Atmos. Chem. Phys.* **2017**, *17*, 705-720, doi:10.5194/acp-17-705-2017.

114. Gao, Y.-Y.; Tan, C.-H.; Ye-Ping, L.I.; Guo, J.; Zhang, S.-Y. Formic acid formate blended solution: A new fuel system with high oxidation activity. *Int. J. Hydrogen Energy* **2012**, *37*, 3433-3437, doi:10.1016/j.ijhydene.2011.11.077.

115. Busó-Rogero, C.; Ferre-Vilaplana, A.; Herrero, E.; Feliu, J.M. The role of formic acid/formate equilibria in the oxidation of formic acid on Pt (111). *Electrochem. commun.* **2019**, *98*, 10-14, doi:10.1016/j.elecom.2018.11.011.

116. Alwe, H.D.; Millet, D.B.; Chen, X.; Raff, J.D.; Payne, Z.C.; Fledderman, K. Oxidation of volatile organic compounds as the major source of formic acid in a mixed forest canopy. *Geophys. Res. Lett.* **2019**, *46*, 2940-2948, doi:10.1029/2018GL081526.

117. Chen, C.L.; Chen, S.; Russell, L.M.; Liu, J.; Price, D.J.; Betha, R.; Sanchez, K.J.; Lee, A.K.Y.; Williams, L.; Collier, S.C.; et al. Organic aerosol particle chemical properties associated with residential burning and fog in Wintertime San Joaquin Valley (Fresno) and with vehicle and firework emissions in summertime south coast Air Basin (Fontana). *J. Geophys. Res. Atmos.* **2018**, *123*, 10,707-710,731, doi:10.1029/2018JD028374.

118. Satish, V.; Robert, J.G.; Donald, D. Simulation and analysis of secondary organic aerosol dynamics in the south coast Air Basin of California. *J. Geophys. Res. Atmos.* **2006**, *111*, D10S12-n/a, doi:10.1029/2005JD006139.

119. Guo J, Pugliesi I, Müller-Dethlefs K, Dessent CE. Multidimensional Franck-Condon simulations of photodetachment spectra for the formate-water cluster anion: Investigating

H atom transfer along the HCOOH+OH reaction coordinate. *J. Chem. Phys.* **2007**, *127*, 234308, doi:10.1063/1.2805188.

120. Tanner, S.D.; Mackay, G.I.; Hopkinson, A.C.; Bohme, D.K. Proton transfer reactions of HCO^+ at 298 K. *Int. J. Mass Spectrom. Ion Phys.* **1979**, *29*, 153-169, doi:10.1016/0020-7381(79)80027-3.

121. J. A. Montgomery, M. J. Frisch, J. W. Ochterski, G. A. Petersson. A complete basis set model chemistry. VI. Use of density functional geometries and frequencies. *J. Chem. Phys.* **1999**, *110*, 2822-2827, doi:10.1063/1.477924.

122. Ochterski, J.W.; Petersson, G.A.; Montgomery, J.A. CBS-Q, CBS-q and CBS-4. *J. Chem. Phys.* **1996**, *104*, 2598.

123. Hunter, E.P.; Lias, S.G. Proton affinity evaluation. *J. Phys. Chem. Ref. Data* **1998**, *27*, 413-656.

124. Linstrom, Peter J.; Mallard, William G. NIST Chemistry WebBook, *Reference Database Number 69*, National Institute of Standards and Technology (Accessed on April **2023**).

125. Guzman, M.I.; Eugene, A.J. Aqueous photochemistry of 2-oxocarboxylic acids: Evidence, mechanisms, and atmospheric impact. *Molecules* **2021**, *26*, 5278, doi:10.3390/molecules26175278.

126. Glasius, M.; Goldstein, A.H. Recent discoveries and future challenges in atmospheric organic chemistry. *Environ. Sci. Tech.* **2016**, *50*, 2754-2764, doi:10.1021/acs.est.5b05105.

127. David, E.; Niculescu, V.-C. Volatile organic compounds (VOCs) as environmental pollutants: Occurrence and mitigation using nanomaterials. *Int. J. Environ. Res. Public Health* **2021**, *18*, 13147, doi:10.3390/ijerph182413147.

128. Wallington, T.J.; Hurley, M.D.; Maurer, T.; Barnes, I.; Becker, K.H.; Tyndall, G.S.; Orlando, J.J.; Pimentel, A.S.; Bilde, M. Atmospheric oxidation mechanism of methyl formate. *J. Phys. Chem. A*, **2001**, *105*, 5146-5154, doi:10.1021/jp0041398.

129. Bready, C.J.; Fowler, V.R.; Juechter, L.A.; Kurfman, L.A.; Mazaleski, G.E.; Shields, G.C. The driving effects of common atmospheric molecules for formation of prenucleation clusters: the case of sulfuric acid, formic acid, nitric acid, ammonia, and dimethyl amine. *Environ. Sci. Atmos.* **2022**, *2*, 1469-1486, doi:10.1039/d2ea00087c.

130. Legrand, M.; Preunkert, S.; Jourdain, B.; Aumont, B. Year-round records of gas and particulate formic and acetic acids in the boundary layer at Dumont d'Urville, coastal Antarctica. *J. Geophys. Res. Atmos.*, **2004**, *109*, D06313-n/a, doi:10.1029/2003JD003786.

131. Matzner, M.; Kurkjy, R.P.; Cotter, R.J. The Chemistry of chloroformates. *Chem. Rev.* **1964**, *64*, 645-687, doi:10.1021/cr60232a004.

132. Mizuno, T.; Takahashi, J.; Ogawa, A. Benzyl chloroformate (CbzCl) synthesis using carbon monoxide as a carbonyl source. *Tetrahedron* **2002**, *58*, 10011-10015, doi:10.1016/S0040-4020(02)01331-5.

133. Herbert, H.R. Patty's Industrial hygiene and toxicology, volume 2A (Toxicology), 3rd revised edition. **1981**, *23*, 592-592.

134. Wieting, J.M.; Fisher, T.J.; Schafer, A.G.; Visco, M.D.; Gallucci, J.C.; Mattson, A.E. Preparation and catalytic activity of binol-derived silanediols. *Eur. J. Org. Chem.* **2015**, *2015*, 525-533, doi:10.1002/ejoc.201403441.

135. Kwak, S.H.; Gong, Y.-D. Unexpected route for the synthesis of N,N-dialkyl formamidines using phenyl chloroformate and N,N-dialkyl formamides. *Tetrahedron* **2013**, *69*, 7107-7111, doi:https://doi.org/10.1016/j.tet.2013.06.026.

136. A. Mellouki. Environmental simulation chambers: Application to atmospheric chemical processes. *Springer* **2006**, 163-169.

137. Lowe, B.; Cardona, A.L.; Bodi, A.; Mayer, P.M.; Burgos Paci, M.A. The unimolecular chemistry of methyl chloroformate ions and neutrals: A story of near-threshold decomposition. *J. Am. Soc. Mass Spectrom.* **2023**, *34*, 2831-2839, doi:10.1021/jasms.3c00334.

138. Su, W.; Zhong, W.; Bian, G.; Shi, X.; Zhang, J. Recent advances in the chemistry of trichloromethyl chloroformate and bis-(trichloromethyl) carbonate. *Org. Prep. Proced. Int.* **2004**, *36*, 499-547, doi:10.1080/00304940409355972.

139. Akyuz, M. Simultaneous determination of aliphatic and aromatic amines in ambient air and airborne particulate matters by gas chromatography-mass spectrometry. *Atmos. Environ. (1994)* **2008**, *42*, 3809-3819, doi:10.1016/j.atmosenv.2007.12.057.

140. Karlsson, D. Sampling chamber with minimal wall surface for simultaneous emission testing of diisocyanates and diamines from polyurethane products. *Toxicol. Ind. Health.* **2023**, *39*, 313-324, doi:10.1177/07482337231172811.

141. Diedhiou, M.; Mayer, P.M. On the gas-phase interactions of alkyl and phenyl formates with water: Ion-molecule reactions with proton-bound water clusters. *Molecules* **2023**, *28*, 4431, doi:10.3390/molecules28114431.

142. Lowe, B.; Cardona, A.L.; Salas, J.; Bodi, A.; Mayer, P.M.; Burgos Paci, M.A. What a difference a chlorine makes: The remarkable unimolecular ion chemistry of phenyl formate and phenyl chloroformate. *J. Mass Spectrom.* **2024**, *59*, e5004, doi:https://doi.org/10.1002/jms.5004.

143. Gondarry, S.; Mayer, P.M. Does the dissociation of guaiacol family radical cations mimic their thermal decomposition? *Comput. Theor. Chem.* **2023**, *1229*, 114323, doi:https://doi.org/10.1016/j.comptc.2023.114323.